Technische Universität München
Fakultät für Elektrotechnik und Informationstechnik

# Label-free, Non-Invasive Cell Based Monitoring Based on Organic Bioelectronics

**Shokoufeh Teymouri**

Vollständiger Abdruck der von der Fakultät für Elektrotechnik und Informationstechnik der Technischen Universität München zur Erlangung des akademischen Grades eines
Doktors der Ingenieurwissenschaften (Dr.-Ing.)
genehmigten Dissertation.

Vorsitzender: Prof. Dr.-Ing. habil. Erwin Biebl

Prüfer der Dissertation:
1. Prof. Dr. Paolo Lugli
2. Prof. Dr. Bernhard Wolfrum

Die Dissertation wurde am 21.09.2021 bei der Technischen Universität München eingereicht und durch die Fakultät für Elektrotechnik und Informationstechnik am 22.11.2021 angenommen.

Dedicated to

my lovely husband,

my beloved parents and brother

# Abstract


## Deutsch

Die Messung der elektrischen Impedanz von adhärierten Zellschichten wird häufig für die Charakterisierung von Zellproliferation und Zellmigration bzw. zur Untersuchung der *in vitro* Toxizität von Materialien eingesetzt. Eine gleichzeitige optische Analyse der Zellen kann noch detailliertere Informationen liefern und zu einem besseren Verständnis der spektroskopischen Impedanzdaten führen. Durch die Verwendung von transparenten Elektroden soll eine deutlich bessere optische Charakterisierung möglich werden. Um dies zu ermöglichen und um die spezifischen Eigenschaften von Kohlenstoffnanoröhren (CNTs) zu berücksichtigen, wurden Elektrodenarrays mit ungerichtet aufgesprühten CNTs auf flexiblen Polymersubstraten hergestellt. Durch Zellkulturstudien und Fluoreszenzspektroskopie wurde ein biokompatibler Photolack ausgewählt, der sich durch geringe Autofluoreszenz auszeichnet. Anschließend wurde eine geeignete Kombination von CNTs und Dispergatoren unter Berücksichtigung der Transparenz und des Flächenwiderstands von sprühbeschichteten CNT-Filmen ermittelt. Die Oberflächentopographie der CNT-Filme, die mit unterschiedlichen Parametern erzeugt wurde, konnte durch Oberflächen-Profilometrie, Rasterelektronenmikroskopie und Rasterkraftmikroskopie

betrachtet werden. Dabei konnte gezeigt werden, dass die Art des Dispergators für die Sprühlösung die optischen Eigenschaften der aufgetragenen CNT-Schichten direkt beeinflusst. Insbesondere da die Gleichmäßigkeit und Transparenz der CNT-Schichten eine wichtige Rolle für die Qualität der zellmikroskopischen Bilder spielt. Bei Messungen, bei denen parallel zur Zellmikroskopie impedimetrische Messungen erfolgten, wurde die Proliferation und Migration von MCF7-Zellen untersucht. Es konnten erfolgreich Wundheilungs-Assays durchgeführt werden, bei denen die elektrischen Impedanz Eigenschaften von Zellschichten auf CNT-Elektroden mit den Daten aus der optischen Mikroskopie korreliert wurden.

# Abstract


## English

Electric cell–substrate impedance sensing is widely used for studies such as cell proliferation, cell migration, and toxicity of materials *in vitro*. Besides, a simultaneous optical analysis of the cells provides more detailed information for a better understanding of the electrical recordings. This reveals the importance of transparent electrodes for a better optical properties. To achieve this goal and considering the exceptional properties of carbon nanotubes (CNTs), we fabricated electrode array with randomly spray-coated CNTs on flexible polymeric substrate. A biocompatible photoresist with low auto-fluorescence through cell culturing studies and fluorescence spectroscopy was selected. Afterwards, an optimized combination of CNTs and dispersants considering the transparency and sheet resistance of spray-coated CNT films were identified. The surface topography of CNT films obtained by surface profilometry, scanning electron microscopy and atomic force microscopy was demonstrated. Furthermore, we compared the optical microscopic results of the cells grown on CNT and standard gold electrodes. The type of dispersant affected directly the properties of CNT films. The uniformity and transparency of CNT multilayers play an important role in the quality of the cell mi-

croscopic images. Finally, we performed impedimetric measurements during MCF7 cell proliferation, in parallel with cell microscopy. We successfully conducted a wound healing assay on CNT electrodes and correlated the impedance graphs with optical images.

# Contents

# Chapter 1

# Introduction

Cells are the functional micro-structure units of living organisms. Every research in life science such as disease diagnosis, discovery and development of drugs closely associate with cell studies. There are two general methods to observe and study cells in the lab. One way is to capture cell activity by microscopy in which we could take images of cells and there are various microscopes for this purpose. The other method relates to the electrical property of cells. This method is specifically called as electric cell–substrate impedance sensing (ECIS) which is a non-invasive method to investigate living cells spectroscopically in real-time, pioneered for the first time by Giaever and Keese [1984]. In this method the electrical property of the cells are measured which can provide various information about cells *in vitro*. The electrical properties of cells can change with cell type, cell morphology and function. ECIS has a wide applications including monitoring cells proliferation, migration, and wound healing (Keese et al. [2004]). In addition, ECIS replaces the traditional methods such as scratch assays and records reproducible and quantitative data.

There are many interests to perform the optical microscopy of cells in parallel

with impedance measurements, to obtain deeper understanding of the spectroscopic impedance data. This enables researchers to perform cell-based assays such as immune-fluorescence in parallel with electrical measurements. Therefore, the mentioned two methods of microscopy and impedance measurement can be combined and provide more information about cells. The common electrode arrays for ECIS assays are made of thin structured gold. Cells are cultured on these electrodes and a weak alternating current (AC) is applied to the electrodes and the impedance of the cell layer is recorded. However, low transparency of gold (Demchenko [2015]) have restricted the optical microscopy of cells, specially by inverted microscopes. Fabrication of electrode arrays made of transparent conducting films is a great progress on the significance of the ECIS method.

In this study, we describe the application of organic carbon nanotubes (CNTs) for the fabrication of ECIS electrode arrays. Beside high electrical conductivity, CNTs have high mechanical strength and flexibility suitable for the deposition of electrodes on polymeric substrates. We used spray coating for direct deposition of random CNT networks onto polymeric substrates, which is a simple, low cost, and low temperature solution-based deposition technique. At the end, we performed the impedimetric measurements in parallel with optical imaging of cells. The CNT electrodes allowed us to correlate the impedance data with high quality microscopy images. This book presents the overview of this procedure including the theoretical information, methods, results, discussions and conclusions in different chapters.

The second and third chapters dedicate to the theoretical part of the thesis. The second chapter introduces the carbon nanotubes with their properties for fabrication of transparent electrodes. The charge transfer mechanism in CNT films, the parameters that influence the conductivity of CNT films, and the var-

ious applications of CNT films are overviewed. The deposition techniques of carbon nanotubes on flexible substrates are explained. The fabrication of homogeneous CNT suspensions, the role of dispersants in dispersion of CNTs, and hybrid structure of CNTs are discussed. This chapter shows the examples of transparent electrodes specially for cell impedance measurement applications.

The third chapter has two main sections. The first section deals with the biology of cultured cells. The common cell types such as epithelial, endothelial and fibroblasts as well as cell organelles are described. The behavior of cells after seeding on a substrate and the cell growth phases are explained. The terms such as cell motility and cell-cell junctions that have been used later in this study are defined. In addition, ibidi GmbH as a leading supplier of products for cellular microscopy and cell-based assays is introduced. The second section provides an overview of ECIS theory, the ECIS device, mechanism of measurements, and interpretation of impedance data. The ECIS® cultureware and their applications are introduced. The wound healing assay is one of the main applications of ECIS which will be described in details here. Beside the several advantages of ECIS cultureware, the limitation of gold electrodes concerning microscopy are discussed.

The chapter four reports the materials and methods that have been used for fabrication of the electrode arrays. It reports the process of various characterization assessments that have been applied to choose the best materials with optimum conditions for electrode arrays. In this study the single-walled CNTs (SWCNTs) and multi-walled CNTs (MWCNTs) are selected as candidate electrode materials. The CNTs are mixed with different dispersants and they are spray coated in multilayers over flexible polymeric substrates. The transparency, sheet resistance (Rs), and surface topography of CNT multilayers are character-

ized. As the electrodes are in direct contact with the living cells, the biocompatibility is the other important parameter in selection of electrode materials. Therefore, the live-dead assay and immunofluorescence assay are performed to reveal the biocompatibility of CNT films as well as the effect of CNTs on the quality of microscopic images. This chapter also shows the process of characterization studies related to the auto-fluorescence properties, biocompatibility, and thickness of the candidate photoresists. Finally the processes of ECIS experiments conducted in combination with the optical imaging of cells are outlined.

The chapter five summarizes the results of the characterization studies and the impedimetric measurements that were shown in the previous chapter. In this chapter the auto-fluorescence properties of several photoresists are compared and the effects of this properties on fluorescence microscopy images are investigated. The cell culture studies demonstrate that the photoresist can affect the cell morphologies and the pre-coating of the photoresist with extracellular matrix proteins can prevent these morphological changes. It is shown that the type of CNTs, dispersant, and the number of spray coated layers influence the properties of CNT films such as transparency, sheet resistance and uniformity of CNT layers spray-coated on polymeric substrate. CNT transparent electrodes noticeably improve the quality of phase contrast and fluorescence images of cells compared to the gold electrodes. However, the uniformity of CNT layers can comparatively affect this quality. The electrical measurements in cell proliferation and wound healing assays done by CNT electrode arrays are presented in this chapter. To consider the main aim of this study, the electrical monitoring of the cells is combined with the optical microscopy, and the electrical measurements are interpreted with the optical images. In each experiment the main findings are discussed and the relevant literature references are given.

In the last chapter, the main conclusions of the thesis are summarized. The topics deal with the photoresists, electrode materials and the impedimetric measurements. An outlook is presented in each section for future studies.

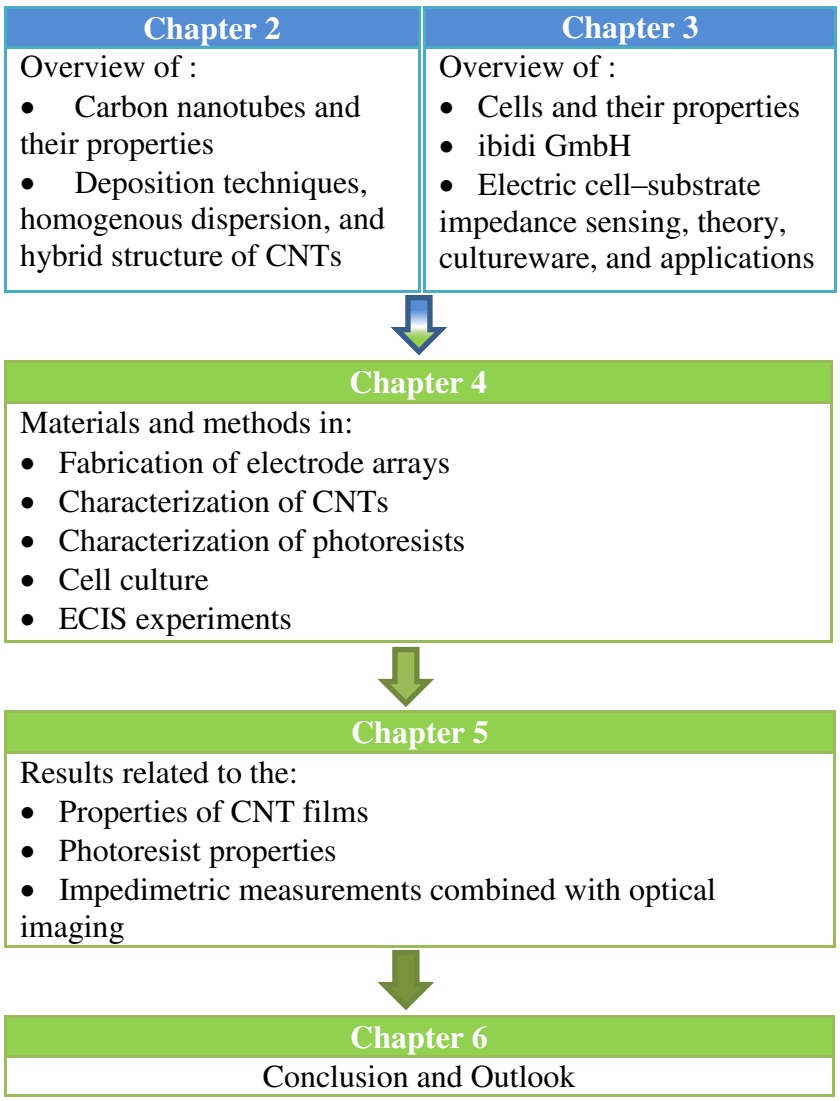


Figure 1.1: Chart summarizing the general structure of the thesis

# Chapter 2

# Carbon Nanotubes: New Generation of Organic Transparent Electronics

Transparent electrodes play an important role when optical monitoring is required in parallel with electrical measurements. Several parameters such as optical properties, biocompatibility, surface topography and stability of electrodes are important to be considered when the electrodes are used for biological applications. The main focus of this chapter is on organic carbon nanotubes (CNTs) and their properties as common materials used in transparent electrodes. Different methods for the fabrication of CNT transparent films are compared. The studies related to the homogeneous dispersion of CNTs for solution-based deposition techniques are discussed. In addition, the hybrid structure of CNTs are introduced. Finally, the application of CNTs for impedimetric monitoring of cell-based assays are mentioned.

## 2.1 Carbon Nanotubes

Carbon nanotubes, discovered in 1991 by Iijima (Iijima [1991]), are organic materials composed of carbon atoms with a hexagonal ring structure in the walls and pentagonal rings in the ends (Georgakilas et al. [2015]). Theoretically, a carbon nanotube is a single 2-dimensional (2D) graphene sheet rolled up in a small tube about a particular axis. This axis is represented as a chiral vector of $C_h$ equal to the $n\vec{a}_1+m\vec{a}_2$ shown in Figure 2.1 a. The values of n and m determine the diameter and chirality of CNTs which are named as armchair, zigzag, and chiral shapes (Figure 2.1 a) (Geim and Novoselov [2007]; Page et al. [2015]). CNTs are categorized as SWCNTs, double-walled CNTs (DWCNTs) and MWCNTs based on the number of graphene cylinders that are concentrically arranged (Figure 2.1 b) (Geim and Novoselov [2007]). Typically the diameter of MWCNTs is in the range of 6 nm to 170 nm which is higher than the average diameter of SWCNTs in the range of 0.4 nm to 2.3 nm (Bandaru [2007]; Moisala et al. [2006]; Sigma-Aldrich [2019a]; Wang et al. [2013b]). Several parameters such as diameter and lenght of tubes, chirality, type of CNT, functionalization, degree of graphitization and crystallinity, and synthesis method affect the properties of CNTs (Vaisman et al. [2006]).

The cabon atom has an electron configuration of $1s^2\ 2s^2\ 2p^2$ at the ground state (Figure 2.2 a), which change to a $1s^2\ 2s^1\ 2p^3$ in excited state. In $sp^2$ hybridization, $2s$ orbital and two $2p$ orbitals form three hybrid orbitals of $sp^2$ and the remaining $2p$ orbital is considered as unhybridized $p$ orbital (Figure 2.2 b). (Armano and Agnello [2019]) In ethylene, the double bond between two carbon atoms consists of one $\sigma$ bond made by two $sp^2$ orbitals between adjacent atoms, and one $\pi$ bond which is formed by overlapping of parallel unhybridized

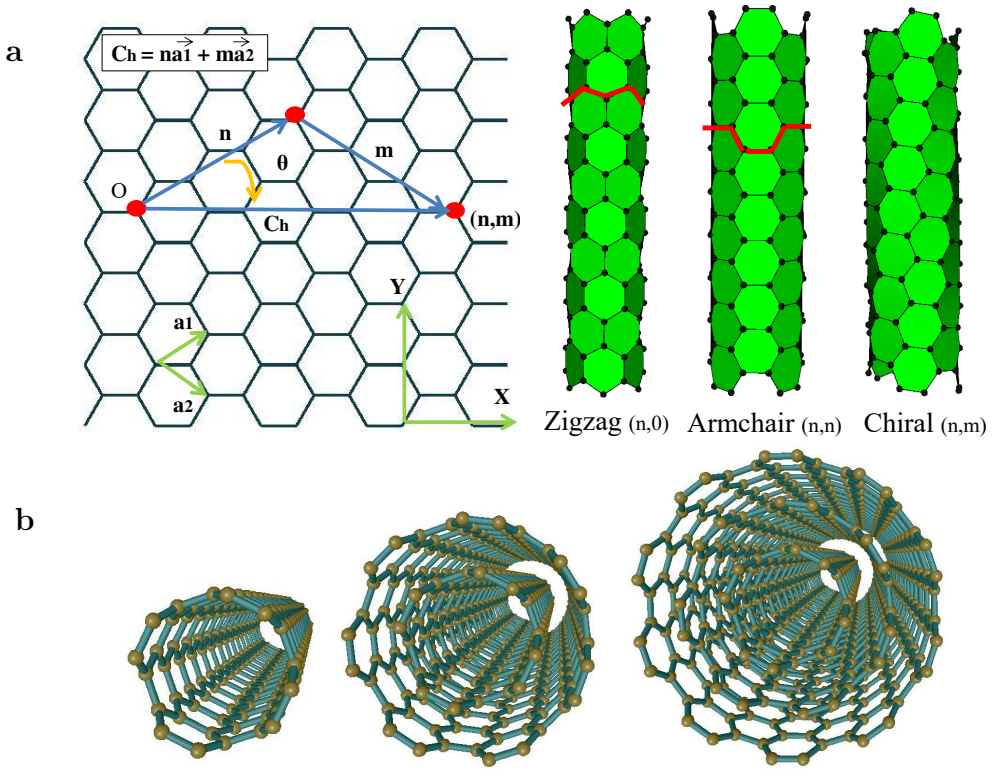


Figure 2.1: (a) Left: graphene sheet and the chiral vector, Right: different types of SWCNTs on the basis of symmetry, zigzag (6,0), armchair (4,4), and chiral shape (5,3). Figures are made in NanoCap software (NanoCap [2019]). (b) Different types of CNTs based on the number of tubes concentrically arranged, from left to right: SWCNTs, DWCNTs, and MWCNTs. Figures are made in Ninithi 1.0 modelling Software for Nanotechnology (Ninithi [2019]). Figure adapted with changes from (Yu et al. [2016]) with permission, ©2016 American Chemical Society.

$p$ orbital lobes on adjacent atoms (Figure 2.2 c) (Liang [2014]). In benzene ring the six electrons unhybridized $p$ orbitals are free to move around the entire benzene ring and form delocalized electron clouds (Figure 2.2 d). Getting back to CNTs, they have abundant conjugated double bonds (alternating double and single bonds of carbon) in the structure which form a $sp^2$ hybridized network. The delocalized $\pi$-electrons of CNTs are responsible for charge carrier mobility in CNTs and different moieties adsorb to the surface of CNTs through these

electrons (Vaisman et al. [2006]).

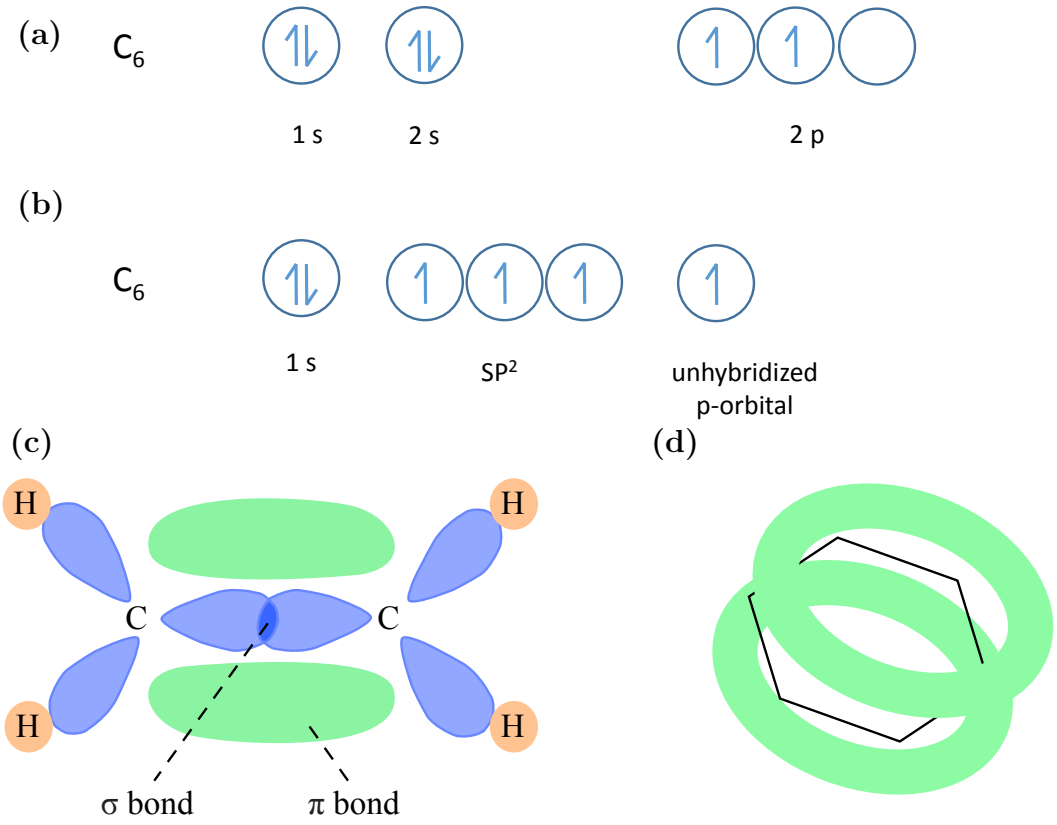


Figure 2.2: Electron configuration of carbon (a) in ground state, (b) in $sp^2$ hybridized state, where 2s orbital hybridized with two of the 2p orbital creating three of $sp^2$ orbitals and an unhybridized p orbital. (c) In ethylene, one carbon atom form 2 single ($\sigma$) bonds and 1 double bond (consists of a $\sigma$ bond and a $\pi$ bond) with adjacent atoms. $sp^2$ hybridized orbitals form single ($\sigma$) bonds and overlapping of unhybridized p orbital lobes form the $\pi$ bond. (d) The delocalized pi electron cloud below and above the benzene ring. (a), (b) and (c) adapted with changes from (Armano and Agnello [2019]), in accordance with the Creative Commons Attribution (CC BY) (License). (d) adapted with changes from (Furukawa et al. [2018]), in accordance with the Creative Commons Attribution (CC BY) (License).

The charge transfer in CNT films follows two mechanisms of intratube and intertube modulations (Li et al. [2003]). In an intratube modulation the charge

transfer occurs in the individual nanotube, and in the intertube modulation charge is transferred at the tube-tube junctions (Abdellah et al. [2013]). The percolation theory has been widely used to study the charge transport behavior in thin films of CNTs. The percolation threshold of CNT films is defined as the critical concentration of CNTs where the conductivity of CNT film changes noticeably (Simien et al. [2008]). Below the threshold, the surface coverage is not sufficient to support a path for charge transporting in thin films. Above a percolation threshold the conductive pathway is formed between CNTs, the charge carriers transfer between the tubes and the electrical conductivity of CNT films increases sharply (Shi et al. [2019]; Xiao et al. [2010]). The percolation threshold can be estimated by the following equation (2.1) (Wypych [2016]):

$$\sigma = \sigma o((N - Nc)/(1 - Nc))^{\alpha} \tag{2.1}$$

where $\sigma$ and $\sigma o$ are the DC conductivity and DC conductivity above the percolation threshold, respectively. $N$ is the density of CNTs bundles, and $Nc$ is the critical density corresponding to the percolation threshold. The value of $\alpha$ indicates the dimension of conductive network (Shi et al. [2019]). The critical density for randomly distributed CNT network is given by the formula (2.2) (Pike and Seager [1974]):

$$Nc = 4.236^2/\pi Ls^2 \tag{2.2}$$

where $Ls$ stands for the length of tubes. Several parameters have significant

influence on the percolation threshold such as the alignment, length, diameter, purity, electronic nature, doping level, and synthesis method of CNTs (Yu et al. [2016]). The simulation studies done by Du et al. [2005] have shown that the surface coverage and alignment of CNTs affect the percolation threshold of the network. They showed that the random distribution of CNTs create a conducting path in the CNT network when the density of CNTs is adequate. Several articles have shown that the random distribution of CNTs is preferred due to the lower percolation threshold (Abdelhalim et al. [2013]; Abdellah et al. [2011, 2013]; Loghin et al. [2016]). Hecht et al. [2006] have shown that the conductivity of SWCNT films increases exponentially by increasing the average CNTs bundle length. They suggested that the longer CNTs show higher conductivity compared to the shorter CNTs with the same tube diameter in a network traversing a sample, which could be due to the lower tube-tube junctions in a network with larger tubes. The dispersion of long CNTs in solution-based deposition methods is an issue, as the length of CNTs can decrease in sonication steps. Another parameter which affects the conductivity of CNT films is the diameter of CNTs. Shin et al. [2009] have shown that the conductivity of a SWCNT network increases by decreasing the average diameter of SWCNT bundles. Simien et al. [2008] demonstrated that the percolation threshold of SWCNT thin film scaled inversely to the aspect ratio CNTs. The presence of structural defects such as amorphous carbon and $sp^3$ hybrid orbitals in the network decrease the conductivity of CNT layers significantly as the charge is scattered in these areas (Yu et al. [2016]).

Chen et al. [2016] have shown that current can flow on the outermost shell of MWCNTs or hop into the inner shells depending on the applied current and the shell diameter. The charge transfer mainly occurs at the outermost shell of MWCNTs at small currents, similar to the high conductance of a graphene sheet

through $\pi$-orbital channels, and the contribution of inner shells is not efficient in increasing the conductivity. At high current, the inner shells can couple to the outer shell by $\pi$-orbital overlapping and more charge carriers are hopping into the inner shells. This can create high anisotropy between the intra- and inter-shell conductivities. The diameter of MWCNTs play an important role in the conductivity of CNTs as the resistance of the outermost layer is inversely proportional to the tube diameter. (Chen et al. [2016]) The individual tubes in MWCNTs with large diameter act metallic (Yu et al. [2016]) and the charge carriers can easier hop into the inner layers (Chen et al. [2016]). While in small diameter (<10 nm) MWCNTs behave more like SWCNTs and the interaction between adjacent shells is negligible (Yu et al. [2016]). Liu et al. [2018] have shown that the electron-tunneling property of CNTs promote the electrocatalytic activity of immobilized glucose oxidase (GO$x$) as well as direct electron transfer between the active sites in GOx and substrate electrodes.

The diameter and symmetry of SWCNTs can change the distribution of bandgap in tubes and shift the electrical conductivity to a mixture of metallic and semiconducting states in SWCNTs (Yang et al. [2014]). The individual semiconducting SWCNT has much higher resistance compared to the metallic SWCNTs at room temperature (Yanagi et al. [2010]). The simulated models by Topinka et al. [2009] have shown that the CNT films with highly pure metallic or semiconducting SWCNTs have higher conductance compared to the SWCNT films with mixture of metallic and semiconducting CNTs. This is due to the fact that the contact resistance between two states of metallic and semiconducting SWCNTs is higher compared to the sheet resistance between CNTs with similar states (Yu et al. [2016]). The model of Topinka et al. [2009] predicts that in SWCNTs when the semiconducting density is more than 70 %, the conduc-

tion does not appear through metallic tubes due to the low density of metallic tubes below the percolation density. With 20 % to 30 % metallic density in the network, the conduction is dominated by Schottky barriers due to the contact resistance between metallic and semiconducting SWCNTs. When the concentration of metallic SWCNTs decreases to less than 10 %, charges bypass the Schottky barrier and start passing through the semiconducting SWCNT paths.

## 2.2 Properties and Applications of CNTs

Thin films of CNTs have wide application in electronics due to their significant properties. The exceptional thermal conductivity (2000-6000 W/mK) (Han and Fina [2011]) and electrical conductivity (as high as $10^6$ to $10^7$ S/m for pure CNTs) (Wang and Weng [2018]) are the remarkable properties of CNTs to be used in electronics. CNTs have been used in thin film transistors (TFT) in mechanical (Chortos et al. [2016]), thermal, chemical (Ellis et al. [2006]), and gas (Loghin et al. [2019]) sensor applications. One of the main advantages of CNT-based gas sensors is the flexibility and low-weight of these sensors (Abdellah et al. [2013]). CNTs have high mechanical properties in particular Young's modulus in the tera pascal (TPa) range, much stiffer than steel, and a tensile strength as high as tens of giga pascal (GPa) (Ruoff et al. [2003]). Due to their significant flexibility, they can be easily deposited on flexible substrates (Abdelhalim et al. [2013]). CNTs have been used for the fabrication of flexible and stretchable mechanical sensors (Yamada et al. [2011]), and flexible temperature sensors (Ren et al. [2016]).

The excellent optical properties of CNTs makes them suitable for the fabrication of thin transparent conducting films (TCFs). Based on the thickness of CNT layers, films with high optical transparancy in the visible range have been fab-

ricated (Kaempgen et al. [2005]). CNT-based transparent conductive electrodes have been previously investigated for organic optoelectronic devices (Falco et al. [2014]) such as organic solar cells (Cho et al. [2014]), organic light-emitting diodes (OLED) (Bondavalli et al. [2009]) and flexible displays. Abundance of raw material (carbon) and the ease of solution processability of CNTs at room temperature are further important benefits of CNTs (Loghin et al. [2016]; Yu et al. [2016]).

CNTs have also wide applications in biomedical, drug and biomolecule delivery systems (Harrison and Atala [2007]; Katz and Willner [2004]; Kumar et al. [2017]). Development of electrochemical biosensors is one of the main application of CNTs for detection of biomolecules. These CNT-based biosensors have detected various biomolecules such as proteins, deoxyribonucleic acid (DNA), glucose, and neurotransmitters (Jacobs et al. [2010]). In recent years, several research groups have developed the CNT biosensors for the detection of cancer cells.

Abdolahad et al. [2012] fabricated vertically aligned MWCNT on nickel-interdigitated microelectrodes and patterned on $SiO_2$/Si substrates as a biosensor for rapid detection and monitoring of cancer cells. In this study CNTs acted as conductive and adhesive layer between cells and metallic electrode for trapping the SW48 human colon cells flowing over the electrodes. They could monitor the presence of cells by changes in the impedance of the electrodes in less than 30 s. The presence of CNT increased the response of the electrode which was not coated by additional adhesive layer or biomarkers. Zanganeh et al. [2016] modified this electrode with amine functional groups by plasma treatment and subsequently folic acid molecules were linked to the amines. Therefore, more cells were entrapped to the electrode due to the specific binding of folic acid molecules to folate receptor existing on the membrane of cancer cells. As a result, a considerable sharper

electrical response was obtained from CNT electrodes modified with folic acid.

In a study done by Liu et al. [2014], MWCNT multilayers were assembled on the surface of amine-functionalized ITO using a dip-coating method. Afterwards, the antibodies of epithelial cell-specific markers were conjugated to MWCNTs via a carbodiimide-mediated wet-chemistry approach. In impedimetric measurements, first the blank values of electrodes were recorded, then electrodes were immersed in HepG2 cell suspensions to achieve cell attachment. Afterwards, the electrodes were washed with PBS and the impedimetric measurements were conducted in the mixture of 5 mM $[Fe(CN)_6]^{3-/4-}$ and 5 mM PBS. Taking advantage of the large specific surface area and good conductivity of CNTs as well as high selectivity and affinity of antibodies, this sensor improved the speed and sensitivity of target cell detection. CNT-based biosensors have been also designed for bacterial detection.

Andrade et al. [2015] developed a CNT-based electrode, in which MWCNTs were drop-coated on a cysteine-modified gold electrode using chemistry crosslinking reactions. Subsequently, antimicrobial peptide clavanin A was chemically modified on CNTs. A small volume of bacteria suspension were dropped on the electrode for 10 min, then electrodes were washed with PBS and impedimetric recording were carried out with Autolab potentiostat/galvanostat. The resulting biosensor showed low limit of detection in concentrated suspensions and it was able to differentiate between different bacterial categories.

Gulati et al. [2020] fabricated biosensors made of vertically aligned multiwalled carbon nanotubes on flexible substrate (PET) by hot press technique. They modified the surface of CNTs in several steps to target doxorubicin treated leukemia K562 cells (Gulati et al. [2019]) or the target DNA (Gulati et al. [2020]). In electrochemical impedance spectra, the impedances had increase pat-

tern by increasing the concentration of target cells or DNA on transducer surfaces. The Biosensors represented good stability and reproducibility. The genosensor showed a detection limit of 0.92 $\mu$M and immunosensor showed detection limit of 10 cells/ml.

In a study done by Vafaiee et al. [2021], multi-walled carbon nanotubes were drop-casted on gold multi electrode array for signal recording from mice brain slices. They observed that the presence of CNTs improved the electrical conductivity of the electrodes while the general electrochemical behavior of CNT modified Au electrode was similar to that of unmodified electrode. Also CNTs created a good interface for neural tissue and the adhesion of the cell to the electrode surface was enhanced.

Foremny et al. [2021] modified the surface of electrocorticographic gold electrodes with a multi-walled CNT-silicone rubber composite to prevent the detachment of CNTs in direct contact with brain tissue during recording. They tested different etching methods to decrease the thickness of insulating shield of silicon on CNTs. Using dry plasma etching technique, the impedance of CNT-silicon electrodes reached slightly higher than the untreated gold electrodes. They successfully recorded auditory evoked potentials by CNT-coated electrodes with similar performance to the untreated gold electrodes.

## 2.3 Fabrication of CNT Transparent Films

The fabrication method of electrode arrays is an important parameter to be considered in industrial applications. Simplicity, low energy consumption, and scalability are the main parameters in the selection of methods. Transfer printing is non-direct method for depositing CNT layers on flexible substrates. The process

of transfer printing is simple, low cost and requires only low temperatures (Abdelhalim et al. [2013]). In this method CNT layers are first deposited on a substrate by different methods such as direct growth methods (Son et al. [2015]), electrophoretic deposition (Pei et al. [2009]), or vacuum filtration (Park et al. [2010]), and afterwards they are transferred to a desired substrate. This technique helps to deposit CNT films on flexible plastic substrates that do not withstand high temperature processes (Abdelhalim et al. [2013]; Son et al. [2015]). Abdelhalim et al. [2013] have sprayed coated CNT films on glass substrates, subsequently transferred it to a PDMS stamp followed by transfering to the PET substrate. They showed that the type of dispersant affects the CNT layer substrate transfer. The SDS-based CNT layers can easily detach from the substrate for transferring them to the other substrate, which is not the case for carboxymethyl cellulose (CMC)-based CNT layers. The transferred SDS-based CNT layers on a PET substrate showed lower Rs compared to the direct deposition of CNTs on PET by spray coating. However, the Rs of CNT layers deposited directly on glass substrates was lower than that of transferred CNT layers on PET, due to the lower roughness of glass than that of PET.

The main disadvantages of transfer printing is its time-consuming process, as CNT films have to be transferred between substrates (Yu et al. [2016]). The presence of air bubbles between the plastic substrate and the overlay can also cause reverse effects on the transferring process (Abdelhalim et al. [2013]). After printing, patterning methods such as $O_2$ plasma etching, direct laser interference (Roch et al. [2014]), or substrate surface modification methods can be used to create patterns on deposited CNT films. For example, Han et al. [2010] have patterned the CNT layers by post-treatment like $O_2$ plasma etching of CNT films transferred to a PET substrate. In $O_2$ plasma etching, the structural defects of

CNTs are bombarded with a high energy plasma. Plasma etching results in the damage of CNTs by changing them to amorphous carbon. Afterwards, the etched CNTs can be dissolved by mild aceton rinsing. (Lu and Panchapakesan [2006]) Yu et al. [2016] have nicely reviewed the current methods for patterning of CNT TCFs.

The direct methods for the fabrication of CNT TCFs are divided into the main categories wet and dry processes. Chemical vapor deposition (CVD) is an example of a dry process in which CNTs are directly grown on metal catalyst particles that are deposited on top of semiconducting or insulating materials. In CVD, the substrate is heated at high temperatures which limit the selection of various substrates. Also acid treatment is required to remove the metal catalyst and/or metal oxides at the end. The CNT TCFs fabricated in dry methods have high conductivity with low defects. (Kumar et al. [2017]; Zhao and Kang [2011]) The wet processes are solution-based techniques that require preparation of a CNT suspension before deposition of CNT films on a substrates. Several methods belong to this category and the most common ones are spin coating, dip coating, spray coating, and inkjet printing. Wet processes are accomplished at atmospheric pressure and room temperature, and various materials such as plastics can be used as substrates for CNT films.

Dip coating is a simple and low-cost method in which a substrate is dipped into the CNT suspension and pulled out to receive CNT film on top. Afterwards, the substrate is dried to evaporate the dispersing solution. Type of dispersant, interaction between the solution and substrate, coating speed, CNT solution concentration, and drying process can all influence the thickness and uniformity of CNT films (Mirri et al. [2012]). Saran et al. [2004] have shown that dip-coated SWCNT films adhere strongly on a PET surface when the nonionic dispersant Tri-

ton X-100 was used, while in case of cetyltrimethylammonium bromide (CTAB) and SDS dispersants films had lower conductivity and did not adhere well to the substrate.

Spin coating is a simple and reproducible method that can create uniform and thin films of CNTs. In this method, a small volume of CNT suspension is dropped on the substrate which is fixed on a sample station by vacuum. The substrate rotates at very high speed and the CNT suspension spreads over the substrate by centripetal force. Afterwards, the sample is heated to increase the rate of solvent evaporation and the dispersant is washed away from the CNT thin film. Viscosity of solvent, time and speed of spinning are the main parameters in spin coating that influence the thickness of the film. Due to the low solubility of CNTs in dispersing fluids, multiple spining steps are required to reach a uniform CNT film with a specific thickness (Piao et al. [2017]; Yu et al. [2016]). The homogeneity of the CNT dispersion has also direct effect in uniformity of spin coated CNT films (Piao et al. [2017]). The spin coating or dip coating methods create CNT layers with lower surface roughness compared to the spray coating (Kim et al. [2010]). Spin coating requires less amount of CNT suspension compared to the dip coating method. In spin coating various substrates can be used. However, it is not possible to deposit CNTs on rough or patterned surfaces (Abdelhalim et al. [2013]). The large-scale production is also limited with this method (Yu et al. [2016]).

Inkjet printing is an economical method for the deposition of CNTs in which less material is required compared to the spin coating. In this method, a drop of CNT suspension is jetted through a nozzle to a specific position on a substrate and this can be continued until a whole pattern is covered with drops. Therefore, CNTs can be printed directly in controllable patterns without the need of masks.

The substrate, solvent and the size of the nozzle play an important role in the quality of deposited films. The hydrophilicity of the substrate is important for the deposition of CNT layers in precise positions. Therefore, substrates can be surface modified or plasma-treated before deposition. The substrate temperature and drop-space have to be optimized to avoid the coffee-stain effect (Dinh et al. [2016]). A solvent with low boiling point can also help to prepare a uniform film with high resolution. Various substrates such as glass, paper, and flexible plastics can be used in this method. In this technique high quality dispersion is required to prevent the formation of a clog in the printer nozzle. (Yu et al. [2016])

Spray coating is a direct method for the deposition of random CNT networks onto various substrates. It is a simple, quick, low cost, and low temperature solution-based deposition technique. Figure 2.3 depicts the setup for spray coating which has been used in this study as well. In this setup, the CNT suspension is sprayed through a nozzle over the substrate. Air atomizing nozzles or ultrasonic spray nozzles provide the finest degree of atomization and break up the CNT suspension into droplets. The geometry and size of the nozzle as well as the physical properties of suspension and gaseous medium surrounding the droplets all affect the nozzle performance (Abdelhalim et al. [2013]). The spray nozzle is attached to an overhead motion platform and moves in X and Y directions with a constant adjustable distance to the substrate. In this technique a shadow mask can be placed on the substrate to create patterns of CNTs on the substrate.

Material flow rate in the nozzle, atomizing gas ($N_2$) pressure, nozzle to sample distance, and speed of spraying are the adjustable parameters in spray coating. These parameters are set based on the dispersant, type of CNT, and the substrate material. Substrate is heated during spray coating to evaporate the solvent in the droplets and let the CNTs and dispersant remain on the substrate. (Abdelhalim

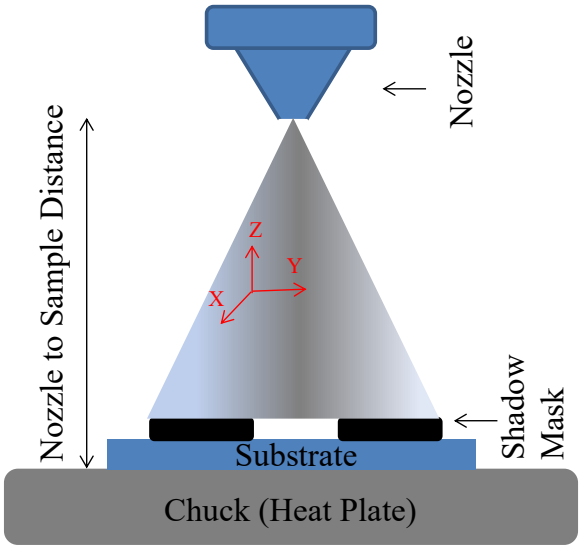


Figure 2.3: Schematic drawing of the spray coating setup. Nozzle to sample distance can be adjusted and the nozzle can move in X and Y directions over the substrate. Figure adapted with changes from (Loghin et al. [2016]) with permission for authors, ©2016 IOP Publishing.

et al. [2013]) This avoids drying-induced aggregation of CNTs (Yu et al. [2016]) and controls the thickness of CNT films. The selected temperature for heating depends on boiling point, vapor pressure of solvent (Abdelhalim et al. [2013]), and heat deflection temperature of the substrate. In this regard, aqueous or alcoholic solvents with low toxicity (Yu et al. [2016]) are selected to prevent release of toxic gas into air or explosions during spray coating.

Kim et al. [2010] have fabricated SWCNT thin films with a Rs of 57 Ω/sq at 65 % transmittance by spray coating of a CNT suspension containing 0.3 wt% SDS in water. Devaraju et al. [2017] have spray coated SWCNTs on a PET substrate using a SWCNT suspension with sulfonated poly(ether sulfone) (SPES) in water. The SWCNT films with Rs of 125 Ω/sq at 87.1 % transmittance showed high electromechanical stability in bending tests. Abdelhalim et al. [2013] did not use

plastic substrates for spray coating of CMC-based CNT solution, due to the long post-treatment in nitric acid $HNO_3$ and a relatively high substrate temperature during spray coating. As CNTs adhere to the substrate weakly (Devaraju et al. [2017]), surface pre-treatment is normally required before spray coating. Abdelhalim et al. [2013] have shown that the plasma cleaning of the surface for 1 min was not enough for CNTs to adhere well to a glass substrate. Therefore, they treated the substrate with (3-aminopropyl)triethoxysilan (APTES) after plasma cleaning for better attachment of CNTs to the substrate.

### 2.3.1 Homogenous Dispersion of CNTs

CNTs have hydrophobic surfaces and they strongly attach together due to the van der Waals forces between tubes (Vaisman et al. [2006]; Zhang et al. [2009]; Zhou and Azumi [2016]). They form aggregates in solvent with the possibility of nanotube entanglement (Thess et al. [1996]) due to their flexibility (Iijima [1996]). One of the main challenges in fabrication of CNT suspensions is to overcome the attractive forces between tubes to achieve homogeneous and stable dispersions. Homogeneous and stable dispersion of CNTs is an essential prerequisite in fabrication of CNT thin films through solution-based methods. The common methods for dispersion of CNTs are chemical and physical treatments of tubes as well as ultrasonication. The main purpose in chemical and physical treatments is to adapt the CNTs to the dispersing fluid and reduce the tendency of tubes to form bundles.

In chemical treatments, the surface chemistry of the tubes are modified to improve the wetting characteristics of CNTs. CNTs are oxidized in concentrated acids to covalently functionalize different groups such as carboxyl (–COOH), oxy-

gen (–C=O), and amino (–$NH_2$) on the tube sidewalls (Dassios et al. [2015]; Lin et al. [2003]). The functional groups are formed at the side walls and mostly at end caps of CNTs or defect sites. The pentagons at the end cap of CNTs are more prone to chemical reactivity compared to the purely hexagonal lattice. (Vaisman et al. [2006]) The covalent functionalization render CNTs more compatible with a chosen solvent, for example CNTs can be dispersed in water without recourse of a dispersant (Yu et al. [2016]; Zhang et al. [2004]). Structural defects can be created on CNTs in strong acid treatments at high temperatures (Zhang et al. [2004]). The chemical functionalization can disrupt the conjugated $\pi$–electrons of tubes and also decrease the length of CNTs (Yu et al. [2016]).

In physical treatment, dispersants or polymers are added to the dispersing fluid containing CNTs. Dispersants reduce the surface tension of water by interactions between the hydrophilic part of the dispersant with water while they are adsorbed on CNTs or self-accumulated into supramolecular structures like micelles (Blanch et al. [2010]; Vaisman et al. [2006]). The chemical structure and the electrical properties of the tubes are not affected in physical treatments. This can be due to the fact that the delocalized electrons in the conjugated $\pi$-system of CNTs are not shared with dispersants in physical treatments. (Blanch et al. [2010]; Dassios et al. [2015])

Dispersants are composed of polar head groups and hydrophobic tail parts with one or few hydrocarbon chains. Based on the charge of the hydrophilic head group, they are classified into cationic, anionic, nonionic, and zwitterionic. Dispersants can physically adsorb on the surface of tubes by non-covalent interactions such as hydrophobic interactions, coulombic attractions, or $\pi$-$\pi$ stacking interactions. Ionic dispersants are preferable when water is selected as a solvent, and nonionic dispersants are proposed when organic solvents are used. Ionic

dispersants can interact with charged surfaces of CNTs through coulombic attractions. The hydrophobic attraction is active between hydrophobic tails of nonionic dispersant and hydrophobic surfaces of CNTs. (Vaisman et al. [2006]) The $\pi$-$\pi$ stacking interactions are created between the aromatic carbon rings of dispersants such as Triton X-100 with surfaces of CNTs (Kaur et al. [2013]).

The parameters such as dispersing fluid, type of dispersant, surface charge of CNTs, and concentrations of CNTs and dispersants can affect the mechanism of interaction between dispersant and CNTs and finally the homogeneity of the dispersion (Blanch et al. [2010]; Ji-Yong Shin et al. [2008]; Shama Parveen et al. [2017]). The length of the hydrophobic tail of a dispersant can also affect the dispersion of CNTs (Ji-Yong Shin et al. [2008]). The simulation studies of Vo et al. [2016] have shown that the parameters such as the number of aggregations, shape, size of dispersant micelles, and their diffusivity in water and or the CNT surface, all can affect the dispersion of CNTs in water.

Sodium dodecyl sulfate is the most common dispersants that is used for dispersion of CNTs (Abdelhalim et al. [2013]; Falco et al. [2014]). This dispersant is water-soluble and can be washed from CNT layers after deposition. Various models have been proposed for structural arrangements of SDS around SWCNTs such as cylindrical micelles (Das et al. [2016]), hemi-micellular adsorption as well as random adsorption with no preferential arrangement (Vo and Papavassiliou [2016]) (Figure 2.4). In a study done by Chastek et al. [2010], fibroblast cells showed abnormal spherical morphology at low concentration of SDS (0.54 mg/ml) in cell culture medium and all cells died at high SDS concentration (14.63 mg/ml). Neupane et al. [2012] have also shown that the density of osteoblasts on $TiO_2$ nanotubular arrays were higher than that of arrays that were fabricated in the presence of SDS. They indicated that the changes in surface roughness and sur-

face energy were the factors that influenced the cell attachment and proliferation on nanotubular surfaces. In a study done by Colombo et al. [2013], breast cancer cell line of 4T1 were incubated with different concentration of PMMA-based nanoparticles. The cells did not survive when the nanoparticles were synthesized with SDS.

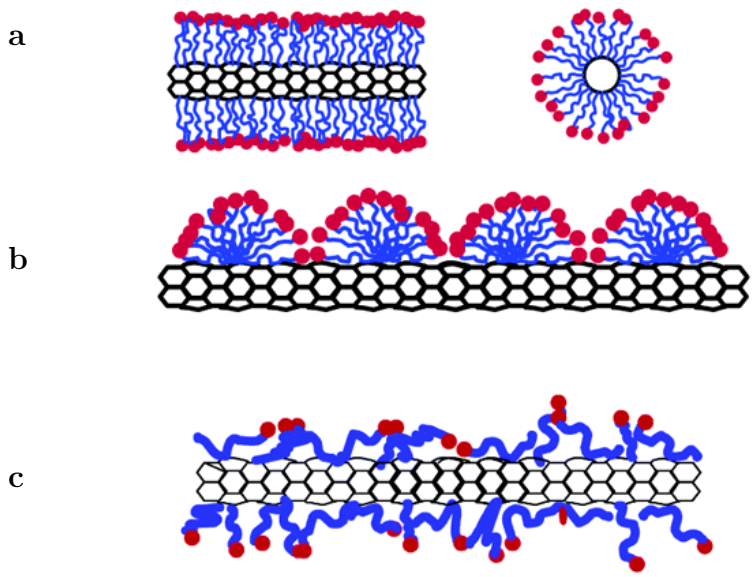


Figure 2.4: Schematic views of the SDS arrangement around SWCNTs in suspension, (a) SDS form a cylindrical micelles around SWCNT (shown in cross-section and side-view), (b) hemi-micellular adsorption of SDS on SWCNT and (c) random adsorption of SDS on SWCNT. Figure is reproduced from (Yurekli et al. [2004]) with permission, ©2004 American Chemical Society.

Carboxymethyl cellulose, a high molecular weight biopolymer, has been reported as an excellent dispersant for dispersing SWCNTs (Minami et al. [2006]). CMC is a water soluble polyanion with carboxymethyl groups (-$CH_2$-COOH) (Abdel-Galil et al. [2014]; Chakraborty et al. [2006]) (Figure 2.5 a). It has been well reviewed in (Fujigaya and Nakashima [2015]) that polymers can wrap the CNTs by specific interaction between a given polymer and the tubes in the

dispersing liquid (Figure 2.5 b). The wrapping mechanism eliminates the hydrophobic interface between the tube and water. Entropic repulsion between polymers surrounding the tubes can act as a barrier among approaching tubes (Shvartzman-Cohen et al. [2004]). CMC has been widely used in different biomedical applications such as magnetite-CMC nanocomposite (Habibi [2014]), CMC-based hydrogels (Reeves et al. [2010]), and CMC—MWCNT hydrogels (Mandal et al. [2016]) in drug delivery systems. In these studies, CMC appeared to be biocompatible and did not cause reverse effects on cells. CNT thin films that are deposited on a substrate from a dispersion of CNT/CMC are wrapped by the polymer matrix of CMC and they are electrically insulated (Tenent et al. [2009]). $HNO_3$ is a common solvent to remove CMC from CNT film to render the films electrically conductive. The acid treatment increases the conductivity of CNT films by reducing the contact resistance between individual CNTs by removing the insulating agents such as SDS and CMC (Zhou and Azumi [2016]).

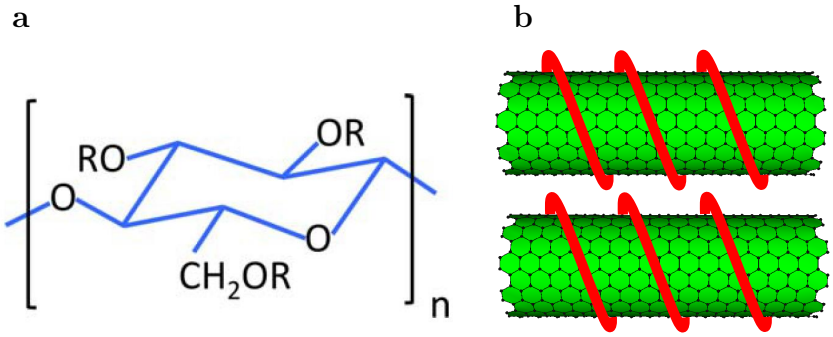


Figure 2.5: (a) Chemical structure of monomer CMC, where R can be H or $CH_2COONa$ (image is copied from Lopez et al. [2015]), (b) Wraping CNTs by polymers in CNT suspension; the polymer chains is shown in red lines. (a) reproduced from (Lopez et al. [2015]), in accordance with the Creative Commons Attribution (CC BY) (License). (b) adapted with changes from (Fujigaya and Nakashima [2015]), in accordance with the Creative Commons Attribution (CC BY) (License).

$HNO_3$ has also a doping effect on CNT TCFs and improves the conductivity of individual CNTs by shifting the Fermi level and increasing the density of charge carriers (Zhou and Azumi [2016]). In a p-doping, electrons are withdrawn from CNTs to the dopant which causes a downshift of the Fermi level into the valence band (Mousavi-Khoshdel et al. [2016]). Therefore, more charge carriers will be available and the Rs decreases. By shifting of Fermi level, the size of the Schottky barrier between semiconducting and metallic SWCNTs is also reduced which can reinforce the charge percolation within the network. (Kim et al. [2016]) Regarding the biocompatibility of $HNO_3$, Vellayappan et al. [2016] demonstrated the $HNO_3$ treatment of metallocene polyethylene modifies the hydrophilicity and blood cloting time of this polymer, resulting in improved hemocompatibility. Donga et al. [2013] have shown that the liquid phase oxidation of SWCNTs with nitric and sulfuric acids remove the possible residual metal catalyst and increase the amount of oxygen (O) content in SWCNT films deposited on a silicon wafer. It was observed that the percentage of apoptotic cells on SWCNTs decreased after acid treatment. This can be due to the higher hydrophilicity of the surface and lower amount of metal catalyst which can behave as an intrinsic toxic element.

CNTs appear mainly bundled in dispersant solution and the outermost CNTs in a bundle have more contact with the dispersant compared to the innermost tubes in a bundle. Therefore, additional mechanical treatments such as sonication is required to open the bundles more efficiently (Vaisman et al. [2006]). In sonication, high shear forces break the intermolecular forces between CNTs and in turn attach CNTs to the dispersants, which noticeably improves the dispersability of CNTs in dispersant solutions (Abdelhalim et al. [2013]). In a mechanism suggested by (Strano et al. [2003]) the high shear force in ultrasonication causes space or gaps at the bundle ends of CNTs where dispersant can propagate between the

bundle and the isolated tube. This will separate the CNT bundles and prevent them from re-aggregating. However, optimum sonication time is required as the long sonication can decrease the aspect ratio of CNTs (Dassios et al. [2015]). After sonication, a centrifugation step is applied to separate the clumps of CNTs that are not well dispersed in water (Abdelhalim et al. [2013]).

### 2.3.2 Hybrid Structure of CNTs

CNTs films have been also fabricated as CNT hybrids in combination with other materials such as metal nanoparticles, nanowires, graphene and conductive polymers instead of chemical dopinng. Various nanoparticles such as silver (Ag), palladium (Pd), gold (Au) have been used for fabrication of CNT-based hybrids for stretchable electronic applications. The presence of nanoparticles increases the conductivity of CNTs films and the presence of CNTs act as a mechanical support and improve the mechanical performance of electrodes. CNTs give high flexibility and stretchability to the electrodes and also increase the charge-transport channels. Park et al. [2010] have fabricated an interconnected network of MWCNT-based hybrid gold nanowires on a PET foil by vacuum filtration and transfer printing techniques. The hybrid film had sheet resistance of 19.4 kΩ/sq at 79.6 % transmittance which was two-fold lower than the sheet resistance of pristine MWCNT films. Lee et al. [2011] have fabricated DWCNTs-based hybrid silver nanoparticles (AgNPs) on a PET substrate with Rs of 53.4 Ω/sq at 90.5 %. They post-annealed the CNT films at 150 °C for 30 min which melted the Ag and increased the contact area on DWCNT. Therefore, the sheet resistance of DWNT-Ag films was improved by 14.23 %. Jing et al. [2014] have fabricated an interconnected network of CNT hybrids with silver nanowires (AgNWs) by

mechanical pressing-transfer process at room temperature. The conductivity of hybrid CNT films highly improved due to the high conductivity of AgNWs. The films had a Rs of 20.9 Ω/sq at 84 % transmittance. The nanowires in thin films can produce hazy optical images due to the light scattering of nanowires (Preston et al. [2013]). The presence of metallic nanoparticles and nanowires in a CNT network can also interface with cells and represent toxic effects to the cells (Chen et al. [2013]).

Graphene is the other material that is used in hybrid structures with CNTs. In a study done by Li et al. [2017], MWCNTs were dip-coated on copper (Cu) foil, and graphene was directly synthesized on MWCNT-coated copper foil by thermal CVD. The CNT/graphene hybrid was transferred to the PET substrate after etching Cu foil. CNTs were uniformly distributed and combined with polycrystalline nature of graphene on PET. The CNT/graphene hybrid with Rs of 5.6 kΩ/sq had higher electrical stability under mechanical stress compared to the graphene film. Kim et al. [2014] have also fabricated hybrid of graphene and SWCNTs on Cu foil by thermal CVD. After patterning of hybrid film, it was transferred onto PET substrate. The Rs of hybrid film was 300 Ω/sq at 96.4 % which was noticeably lower than the Rs of graphene (1000 Ω/sq at 97.0 %), SWCNT (1200 Ω/sq at 97.1 %), graphene coated with SWCNTs (1100 Ω/sq at 96.2 %) films. The contact resistance between graphene and SWCNTs was lower in hybrid form. The presence of SWCNTs in hybrid enhanced the flow of charge through the grain boundaries of the graphene sheet and avoid defect scattering at graphene boundaries. In a study done by Barshutina et al. [2021], hybrid silicone composites with various graphene/CNT mass ratios and concentrations were studied. With optimal parameters, they achieved even distribution of graphene/CNTs in the matrix which provided a better electrical and mechanical properties compared to

composites containing either of graphene or CNTs alone..

Conductive polymers are the other option to make CNT-based hybrids which are cheaper, less toxic, and more flexible compared to the inorganic nanoparticles or nanowires. Beesley et al. [2016] have used PEDOT:PSS in fabrication of hybrid PEDOT:PSS/SWNT films. The film had Rs of 90 Ω/sq at 80 % transmittance. PEDOT:PSS was used as a dispersant for SWCNTs without using dispersant and the suspension was spin-coated on glass substrate. SWCNTs were homogeneously distributed in the PEDOT:PSS suspension without agglomeration after the sonication/centrifugation procedure and the spin-coated hybrid films were uniform as well. In hybrid thin films we can find the properties of more materials. The conductivity of CNT layers increases after hybridization and they show better electrical stability under mechanical stresses.

# Chapter 3

# Application of Electronics in Biology

In this chapter, the required knowledge for the next chapters about cell biology is introduced. Several topics related to the cell proliferation, cell growth phases, and the reaction of cells on a substrate are explained. Also the behaviors such as cell micromotion, and communications between adjacent cells are mentioned. Afterwards, the way how cells are cultured in the lab is explained. At the end of the section, ibidi GmbH as a leading supplier of cellular microscopy products and cell-based assays is introduced. The main purpose of this chapter is to show the application of electronic in biology. Therefore, the theory of ECIS, components, mechanisms of measurements, the ECIS cultureware and related applications are explained.

## 3.1 Biology of Cultured Cells

Single cells are the first organisms to exist since billions of years ago. The cells yet remain the smallest and the most basic unit of life and living organisms. Multicellular organisms consist of many different types of cells, each performs specific functions. For example, the human body consists of a variety of organs and it is not surprising that it contains more than 200 different types of specific cells. The diversity of cells in nature is much greater than the number of the cell types found in human body. Three common cell types in most organs are fibroblast, epithelial, and endothelial cells, and each has specific functions and locations in an organ. Epithelial cells form the outermost layer of the skin, line the cavities such as lungs, gastrointestinal tract, and small intestine. They have various functions, such as protection of organs against bacteria and viruses, secretion of enzymes, and absorption of nutrients. Endothelial cells form the innermost layer of the endothelium in blood vessels. Therefore, the blood flow is in direct contact with endothelial cells. Fibroblasts are the most common cells in connective tissues which synthesize the components of the extracellular matrix such as collagen (Retrouvey et al. [2014]). The connective tissues forms a supportive framework for epithelial cells, muscle fibers, and nervous tissue. Fibroblasts can migrate independently which is very important for their functions (Petrie and Yamada [2015]). They can also migrate into the area of the wound to assist in wound healing by closing up the damage edges. One of the obvious differences between these cell types is in their morphology. (Cain [2002]; Mallinjoud et al. [2014]) Figure (3.1) represents three basic categories of cell morphologies (ThermoFisher [2019]). Cells with epithelial morphology grow on a substrate in patches with polygonal shape (Joshi et al. [2016]), and fibroblastic cells have typically spindle and elon-

gated shape. Lymphoblast-like cells have round morphology growing singly or in clumps in cell culture medium and they do not adhere to the substrate.

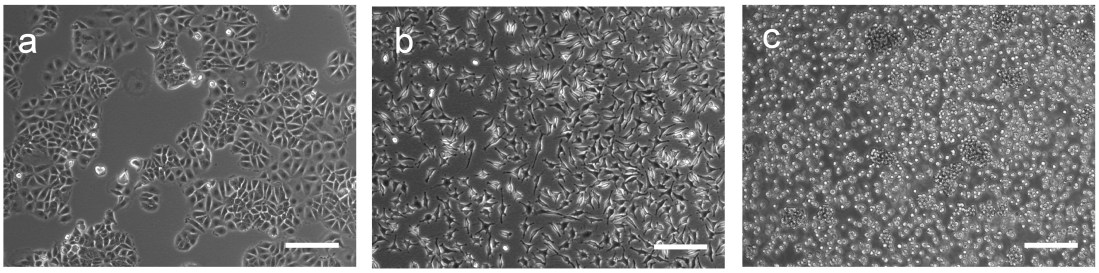


Figure 3.1: (a) MCF7 breast cancer cell line grow with epithelial morphology on a substrate, (b) L929 murine fibroblast cell line grow adherently as monolayer, and (c) Jurkat cell line with spherical morphology which do not adhere to the substrate. The scale bars are 200 $\mu$m.

Cells have different organelles such as mitochondria for the production of energy, endoplasmic reticulum for synthesis and transportation of proteins, ribosomes for proteins synthesis, and cytoskeletal filaments (Figure 3.2). The cytoskeleton of cells consist of actin filaments, microtubules, and intermediate filaments. The cytoskeleton filaments are responsible to position organelles inside the cytoplasm, maintain the structural framework of cells, and also for cell movements and cell division (Fletcher and Mullins [2010]; Ganguly et al. [2012]). All these components are located in an environment called cytoplasm. The control center of the cell is the nucleus where DNA strands containing genetic information are located. The nucleus controls the cell functions, growth, and reproduction. The cytoplasm is surrounded by a membrane which separates the cytoplasm from the surrounding environment called the extracellular matrix. The cell membrane consists of a lipid bilayer that induces different concentrations of ions in extra- and intra-cellular environments. Therefore, the cell membrane can be modeled as a capacitor with an insulating sheet of lipid bilayer separating the two electrically

conductive salt solutions.

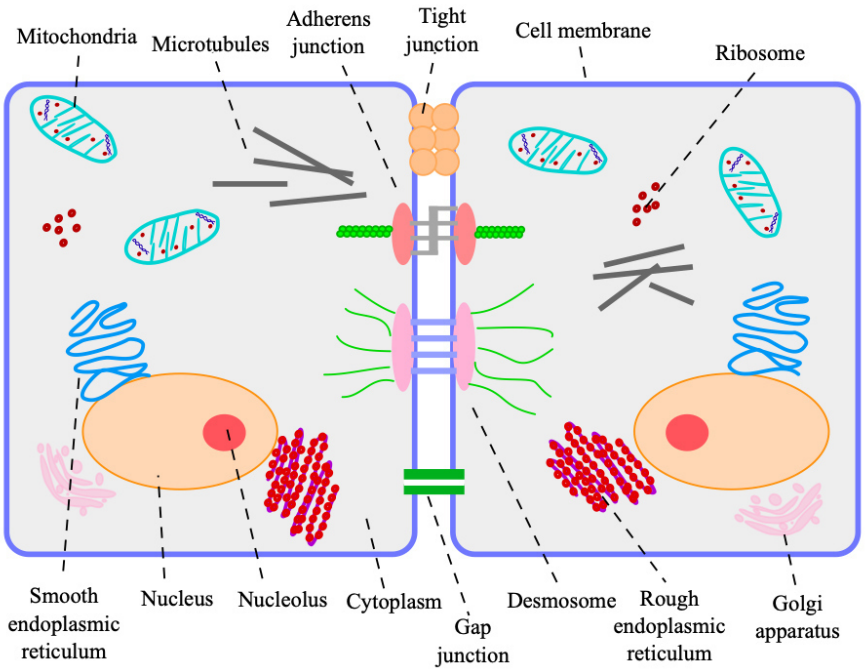


Figure 3.2: Organelles inside the cytoplasm of cells as well as cell-cell junctions between two adjacent cells. Not to scale. Junctions adapted with changes from (Kutova et al. [2020]), in accordance with the Creative Commons Attribution (CC BY) (License).

Most cells are anchorage-dependent and grow as an adherent layer when they are cultured on a surface. There is another type of cells called suspension cells which are anchorage-independent cells. These cells can propagate in cell culture medium without adhering to the substrate. The adherent cells follow several steps to form a monolayer on a substrate. At the beginning after cell seeding, cells have a round-shape morphology on a substrate (Figure 3.3 a). Subsequently they sense the substrate by receptors on their surface and attach to the substrate (Figure 3.3 b,c). On the surface of cells there are receptors such as integrins and transmembrane proteoglycans which have binding sites to interact with molecules

on the extracellular matrix and proteoglycans (Freshney [2005]). The integrins mediate cell-matrix adhesion when a substrate is coated with matrix constituents such as fibronection, collagen, or laminin. After cell adhesion to the surface, cells start spreading over the substrate and divide to increase the cell population (Figure 3.3 d,e). The process of cell development and cell division is known as cell proliferation. The cell membrane is not in complete contact with the substrate when cells adhere and spread on a substrate, but it adheres to a substrate in focal adhesion cites. In focal adhesion sites, integrins are connected to the cytoskeleton and mechanical forces are transmitted between the substrate and the cell (Nicolas et al. [2008]). If the substrate is inert and cells do not adhere, they remain round-shaped on the surface.

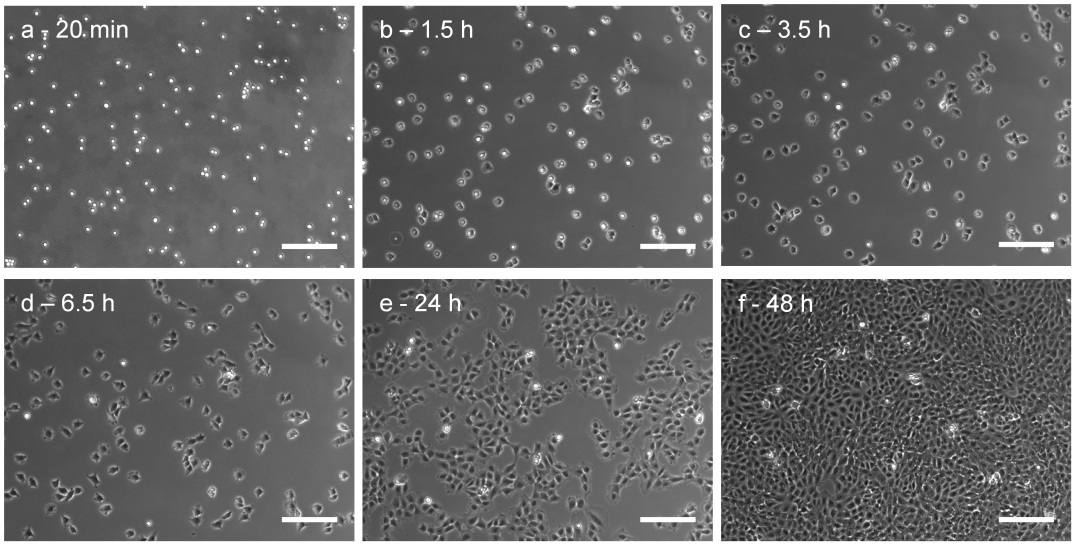


Figure 3.3: (a) The round morphology of Rat1 cells upon seeding on treated $\mu$-Slide 2 Well$^{Ph+}$; (b,c) After cell-substrate adhesion, cells started to spread on the substrate; (d,e) Cells divided and interacted with adjacent cells and (f) finally they fully covered the surface. The scale bars are 200 $\mu$m.

Based on these steps, cell growth has typically four phases shown in Figure 3.4.

In the first phase called 'lag', cells adapt to their medium and the new location after seeding, they spread and prepare for replication. This phase is followed by the log phase where cells start dividing and cell numbers increase exponentially to form a confluent cell layer. Each cell line exhibits a different growth rate in the log phase. Afterwards, they enter the stationary (or plateau) phase where cell proliferation slows down as there is no more room for additional cells. Most normal cells, unlike cancer cells, stop proliferation in this phase due to the density-dependent inhibition of cell division. The last phase is the death phase where cell numbers decrease due to a natural cell cycle. (Alberts et al. [2002]) Several factors can affect the cell growth such as temperature, pH of the cell culture medium, oxygen, and nutrients.

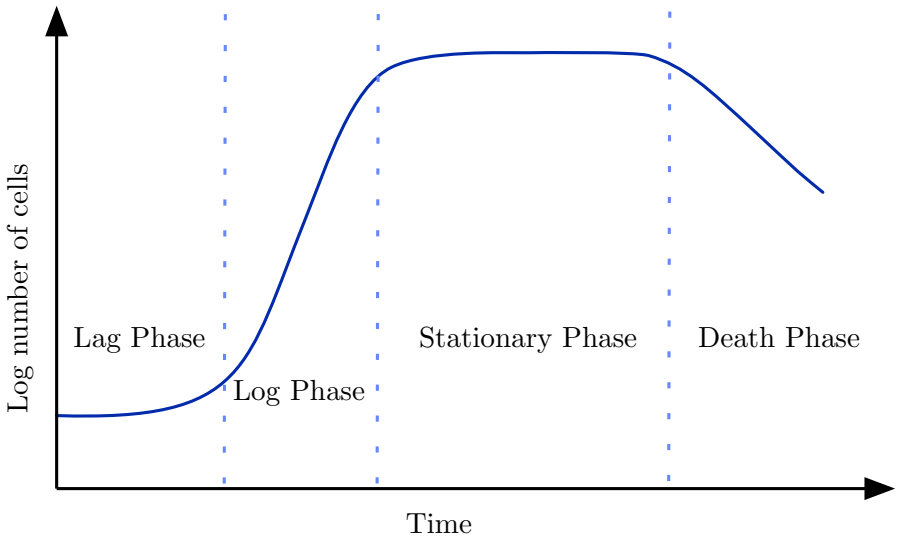


Figure 3.4: The four phases of cell growth in culture. Figure adapted with changes from (Adams et al. [2007]) with permission, © 2007 Humana Press Inc., Totowa, NJ.

The epithelial and endothelial cell lines need to have contact between adjacent cells to grow normally on a substrate or in their natural environment. This

contact is achieved by cell-cell adhesion proteins which form junctions between cells. There are three main types of junctions between cells called tight junction, desmosomes, and gap junctions (Figure 3.2). Tight junctions seal the space between the adjacent epithelial or endothelial cells. Several transmembrane proteins such as claudins and occludens participate in the formation of tight junctions (Freshney [2005]). Tight junctions create a paracellular barrier between cells which are semipermeable to the molecules transporting in the paracellular pathway. The presence of tight junctions can avoid diseases such as inflammatory bowel disease (IBD), infections and cancers in the body. However, they can also behave as a barrier for transport of drugs in treatment of diseases. (Chiba et al. [2008]) Tight junctions also play a role in signal transduction. Desmosomes and adherens junctions are mechanical junctions that fix the cells together and also further strengthen the tight junctions. They are resistant to stretching and twisting. As an example cadherins form adherens junctions between adjacent cells. Gap junction are small channels made of connexon proteins between cells that allow the communication of adjacent cells and transfer of ions between cells.

Cells are dynamic and they are in constant micromotions on a substrate driven by their microfilaments (Keese and Giaever [1994]). The motility is different in cell types, for example fibroblasts tend to migrate as individual cells and they are highly motile when they are not in contact with other cells. The epithelial cells migrate to find other cells and they accumulate in patches. Once a cell touched another cell the migration stops. However, the whole patch may show signs of coordinated movement. In a monolayer epithelial cells are tightly connected to each other. (Freshney [2005])

In a cell biology laboratory, cells are cultured in cell culture flasks before the experiments. In the laboratory the aim is to provide an environment close to the

physiological conditions for cells. Therefore the flasks are placed in incubator to provide 5 % $CO_2$ and 37 °C temperature for the cells. Based on the growth rate of cells, they are subcultured into new flask between once to three times per week. In subculturing or passaging, a defined number of cells from a previous flask is transferred into a new flask with fresh medium.

The ibidi GmbH is a leading supplier for cell-based assays and products for cellular microscopy. It was founded in the year 2001 as a spin-off from the Technische Universität München and it is currently located in Gräfelfing, Germany. ibidi offers various labware, instruments and reagents suitable for applications in the fields of virology, neurobiology, micropatterning, 2D and 3D cell culturing, and live cell imaging. There are several labware produced by ibidi such as open slides, dishes, channel slides, micro-plates, and sticky-slides, which have applications in cell-based assays such as wound healing and cell migration, angiogenesis, chemotaxis, and immunofluorescence. The channel slides and perfusion systems of ibidi have applications in cell culture studies under flow. In addition, ibidi provides several reagents related to the transfection, transduction and membrane fusion studies. ibidi offers software solutions for automated and manual cell image analysis. Regarding the instruments, the Heating and Gas Incubation Systems of ibidi allow live cell imaging under physiological conditions. Also ibidi distribute the ECIS instruments and cultureware of Applied BioPhysics, Inc. (New York, USA) in Europe. ibidi has received numerous awards for its innovation and creativity over last years.

## 3.2 Electric Cell–Substrate Impedance Sensing

### 3.2.1 Theory of ECIS

The electric cell-substrate impedance sensing is a label-free method that monitors living cells electrically. With this method cells are monitored in real-time while growing on electrodes. ECIS is a non-invasive approach for cell monitoring, as there are no detectable effects upon cells on their morphologies and division times between cells growing on electrodes or in cell culture flasks (Giaever and Keese [1986]). Cell studies performed by ECIS can avoid many *in vitro* studies with animals.

The ECIS system is basically composed of the two separate units array station and station controller (Z$\theta$) (Figure 3.5). The array station has signal processing circuits and switching mechanisms which can change the measurements from well to well in an electrode array. The electrode arrays are fixed on the array station during the measurements. The array station is incubated at 37 °C and 5 % $CO_2$ when cells are cultured in the electrode arrays. This can provide the required environmental conditions for the cell growth. The array station is connected to the station controller by a cable, which contains circuits for impedance measurements and oscillators to supply AC currents. The station controller (Z$\theta$) can measure the impedance, capacitance, and resistance of cells growing on the electrodes. The electrical measurement data is computed by the ECIS Biophysics software in a laptop connected to the station controller. (Applied BioPhysics, Inc. [2021])

The mechanism of ECIS measurments is explained with one of the common electrode arrays that is used with this system shown in Figure 3.6. The ECIS® cultureware 8W1E is fabricated in a two-electrode configuration, made of gold

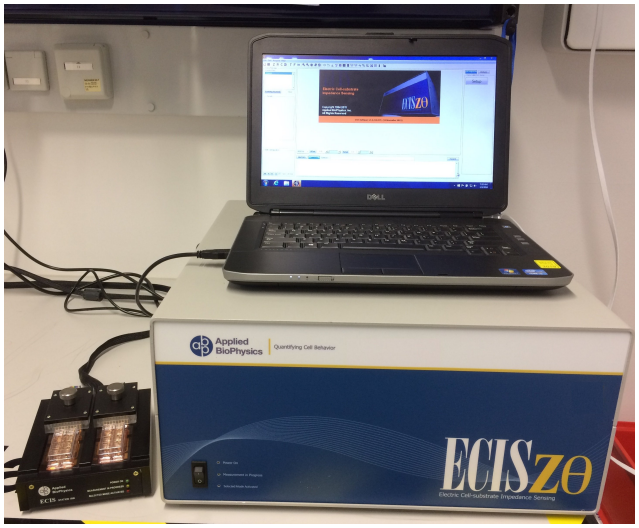


Figure 3.5: The station controller (Z$\theta$) and the array station 16 well. A laptop is connected to the station controller.

on a PET polymeric substrate. It has eight wells and in each well there is one working and one counter electrode. In impedance measurements, the standard cell culture medium is used as an electrolyte, which contains all the required nutrients for the cell growth. A weak AC current ($\simeq 1\,\mu$A) is applied through a 1 M$\Omega$ resistor across the electrodes at the bottom of the ECIS arrays. The current flows between a 250 $\mu$m diameter working electrode and a counter electrode. The counter electrode has a larger area compared to the working electrode. Therefore, the resistance of the working electrode to the AC current is dominant. While cells grow on the electrodes, the AC current is kept constant and the voltage changes are measured across the working and counter electrodes over time. The resistance ($R$) is obtained by the Ohm's law (R=V/I). In AC system, the complex impedance ($Z$) is calculated using the following formula:

$$Z = \sqrt{R^2 + (\frac{1}{2\pi fC})^2} \tag{3.1}$$

In this formula, the complex impedance consists of two parts: the ohmic resistance and the reactance ($\frac{1}{2\pi fC}$), where $f$ stands for frequency of the AC current and C is the capacitance. (Lo et al. [1995]; Rahman et al. [2009]) Based on the Warbung model, the cell-free electrode which is in contact with electrolyte, can be described as a capacitor and a resistor. This model was developed for cell-covered electrodes in contact with cell culture medium (Giaever and Keese [1991]). Before adding cells into the wells, the impedance of the electrodes is constant, as the current can freely move between the working and counter electrodes without any barrier. Once cells are added, they start attaching and spreading on the base of each well and onto the surface of working and counter electrodes. Therefore, the current flow is restricted by cells and thus the electrical resistance changes. The capacitance also changes as the cells grow on the surface of electrodes due to the capacitive effect of the cell membrane (Robilliard et al.). The altered impedance can provide useful information about the cellular behaviors such as cell growth, cell coverage and their dynamic behaviors. (Keese and Giaever [1994])

A typical electrical graph obtained by ECIS measurements is presented in Figure 3.7. This graph shows that in the first minutes the electrodes were equilibrated to prevent drifting of the electrodes during the experiment. Afterwards, cells were inoculated in the wells and they started to attach and proliferate on the surface of the electrodes. The growing cells on the electrodes act as an electrical capacitor and insulator, and they can constrain the current flow and change the path of current. Therefore, the impedance increases as the number of cells on

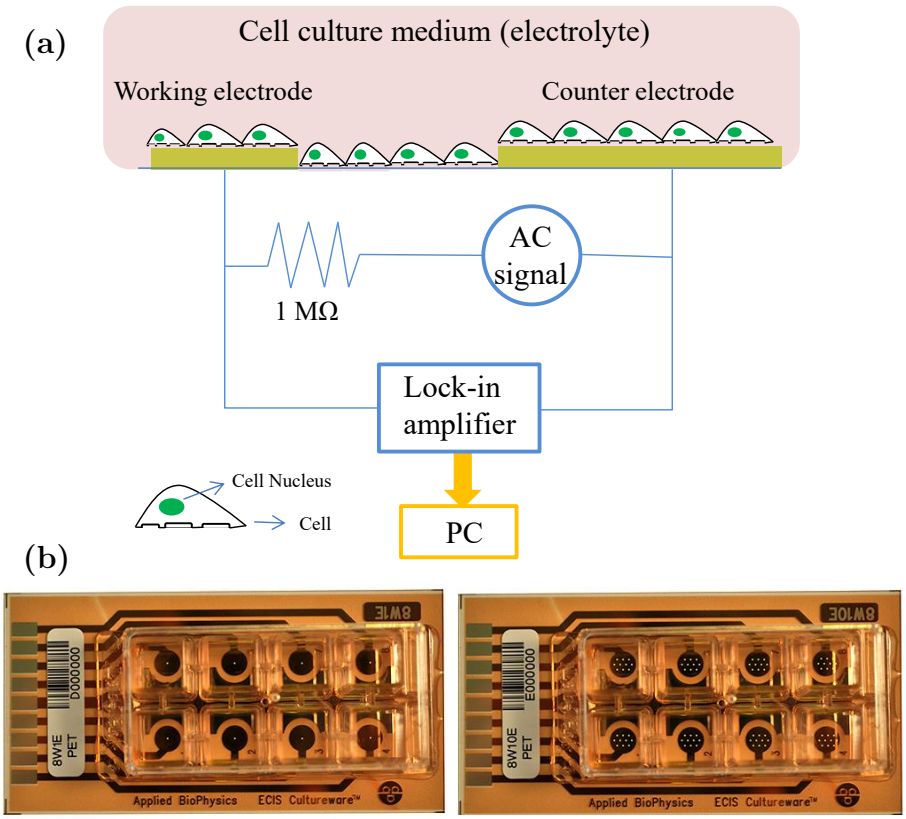


Figure 3.6: (a) Mechanism of ECIS measurments. Figure adapted with changes from (Keese and Giaever [1994]) with permission for authors, ©1994 IEEE. (b) the ECIS® cultureware 8W1E and 8W10E. Figure adapted from (Applied BioPhysics, Inc. [2021]), with permission from Dr. Charles R.Keese, the founder of Applied BioPhysics Inc.

the electrodes is increasing by cell divisions. The impedance reaches a plateau, when the surface of electrode is fully covered with cells. The impedance should theoretically remain in a plateau. However, it can also have a decreasing trend as the cells reach the death phase. Providing fresh medium can help delaying this process. Sometimes the impedance does not remain in the plateau more than couple of hours due to the high cell density in the wells and a lack of enough nutrients. Therefore, the impedance reaches a peak and then starts decreasing.

Cells have constant micromotions on the surface of the electrodes. The ECIS can even sense these small changes and measure them quantitatively. The cell motility on the surface of the electrode alters the effective open area available for the current flow. Therefore, they can cause small fluctuations in the measured impedance (Aas et al. [2002]; Dzementsei et al. [2013]; Giaever and Keese [1991]; Keese and Giaever [1994]).

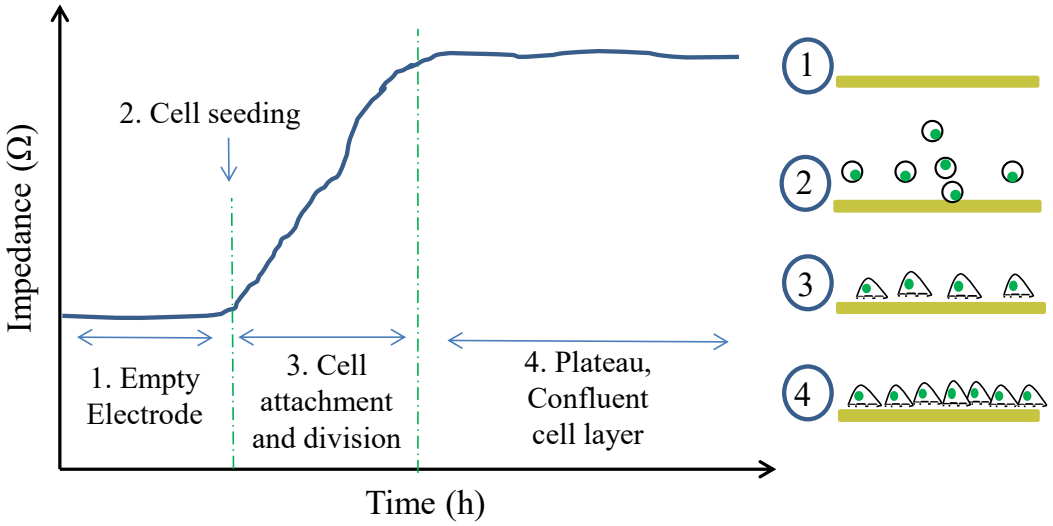


Figure 3.7: Schematic of the typical ECIS impedance graph. Figure adapted with changes from (Applied BioPhysics, Inc. [2021]), with permission from Dr. Charles R.Keese, the founder of Applied BioPhysics Inc.

As it is mentioned before, cells do not fully adhere to the surface of an electrode when they attach and spread. In fact, cells adhere to the substrate in cell-substrate adhesion points and there is a small gap between cells and surface providing channels in between (Giaever and Keese [1991]; Zhang et al. [2012]). The range of the frequency has an important role in defining the path of current through the cells. During ECIS measurements, the AC current is applied to the electrodes with different frequencies ranging from 65 Hz to 64 kHz. Considering

the formula 3.1, in low frequencies the reactance approaches unlimited values and the current flows mainly through the resistance part (Figure 3.6). In high frequencies, the reactance tends to zero values and the current flows through the capacitive part. Coming back to the cells, at low frequencies (<4 kHz) the resistance part of the impedance is more dominating and most of the current flows via paracellular pathways under the cells and between the adjacent cells (Figure 3.8). At higher frequencies, the capacitive part is more dominating and most of the current capacitively couples through the cell layer via the transcellular pathway. In resistance data from cells, the resistance increases when the number of cells on the electrode increases. Also, the cells with tight junction have significant higher resistance peaks compared to cells without tight junctions (Clark et al. [2015]). On the contrary, the capacitance at high frequencies provides information about the surface coverage of the electrodes (Giaever and Keese [1986, 1991]; Izak et al. [2016]). The capacitance decreases when the number of cells on the electrode increases (Szulcek et al. [2014]; Wegener et al. [2000]).

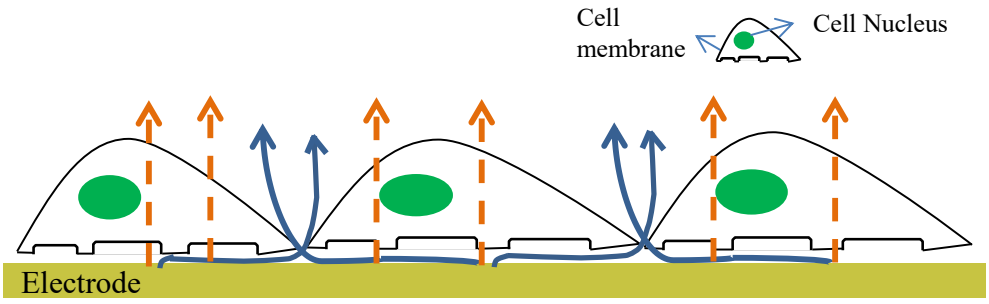


Figure 3.8: The schematic view of current path, where at low frequencies current preferably flows out under and between the cells shown in blue lines. At high frequencies most of current capacitively couples through the cell membranes shown in orange dashed arrows. Figure adapted with changes with permission from the author of (Giaever and Keese [1991]) Dr. Charles Keese.

### 3.2.2 ECIS Cultureware and applications

Applied BioPhysics, Inc. provides several electrode arrays for various impedance-based cell assays in the market. The ECIS® cultureware 8W1E is one of the typical electrode arrays that is used in wound healing assays. In this assay, cells are cultured in the wells of this array until they form a confluent layer over the working electrode. Afterwards, a high current more than 1 mA is applied to the electrodes for a defined time which can kill the cells on the working electrode (Figure 3.9). The high current perforates the cell membrane and the contents of cells leak out to the cell culture medium. Therefore, cells loose the integrity and reshape to round morphologies, either remaining on the electrode or detach from the electrode surface and float in medium. As a result, the impedance decreases sharply close to the initial values before cell seeding. Upon perforation, only cells on the working electrode die and the surrounding cells are not affected, which is similar to creation of a wound in a cell layer that surrounding viable cells have to repair it. Therefore, the cells surrounding the working electrode migrate over the electrode and repair the created wound over time. The impedance increases again with gradual closure of the wound. The wounding assay done by 8W1E electrode arrays replaces the traditional method of scratch assays, and records reproducible and quantitative data.

The wound healing assay can also be combined with toxicity assay which is the other important application of ECIS technology (Keese et al. [2004]). In toxicity assay the effect of different chemicals, drugs or different extracellular matrix proteins on cells' behaviors such as proliferation, dynamic of cell growth, as well as the morphological changes can be studied. Also in toxicity assays we can assess the toxicity of chemicals through the viability of cells in direct and non-

direct contact with chemicals. Therefore, different materials such as chemicals, biomolecules, or drugs can be added to the cell culture medium after wounding. Then, we could monitor the cell growth over time and compare them with cells in control conditions. The combination of these two assays is an alternative to the animal testing.

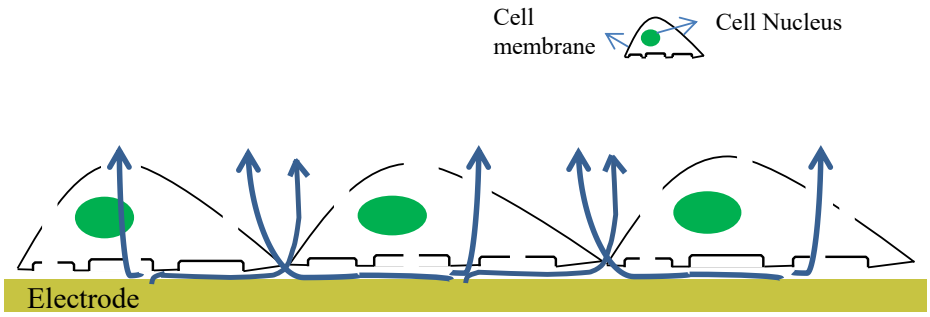


Figure 3.9: Schematic of the cell membrane perforation by high current in wound healing assay. Figure adapted from (Applied BioPhysics, Inc. [2021]), with permission from Dr. Charles R.Keese, the founder of Applied BioPhysics Inc.

The next common electrode array is ECIS® cultureware 8W10E which has close configuration to the 8W1E array. This array has 10 working electrodes (each 250 $\mu$m diameter) per each well and it is in two-electrode configuration. All ten parallel-connected electrodes on a common gold pad in a well influence the final impedance. The 8W10E array includes more cells in the measurements compared to the 8W1E array as the electrodes in 8W10E cover larger areas in a well for cell analysis and this can limit bias of the data by uneven inoculation (Szulcek et al. [2014]). The fluctuations recorded from micromotions are reduced in 8W10E compared to the 8W1E. This array is suitable to quantitatively study the cell proliferation, cell differentiation, barrier function, cell invasion, and cytotoxicity in real time and continuously (Applied BioPhysics, Inc. [2021]). For

wound healing assay, the 8W1E electrode array is more preferred compared to the 8W10E electrode array. In 8W1E array all the perforation current is applied to just one electrode, while in 8W10E the current is divided to 10 electrodes. Therefore, destroying of all cells on all 10 working electrodes could not be as efficient as destroying of all cells on only one electrode in 8W1E array.

The impedance of cells can also be recorded when cells are under flow. In blood or lymphatic vessels, endothelial cells are in direct contact with flow of fluids. The flow causes a shear stress over the cells which can affect the functional properties of cells (Chistiakov et al. [2017]). The flow ECIS arrays are popular arrays for this purpose, available in different configurations. These arrays are connected to the ibidi perfusion system to simulate physiological conditions for the cell growth. The flow of cell culture medium causes shear stress over cells *in vitro*, which resembles the shear stress that endothelial cells experience *in vivo*. Thanks to these arrays the biological functions can be studied not only in static conditions but also in dynamic conditions and in circumstances more similar to the origin environment of cells.

The gold electrodes have broad applications in electrical recordings specially in studies related to the cell biology. However, the limitations in optical microscopy have restricted the monitoring of cells both electrically and optically at the same time. Considering the low transparancy of gold electrodes, the inverse microscopy of cells, grown on gold electrodes is problematic. On the other hand, the gold material is deposited on the polymeric substrate by vapor deposition technique which results in high waste of raw materials. Transparent conductive electrodes could provide alternative materials for relevant applications. In next chapters, we present the application of CNTs as transparent conductive electrode in impedimetric measurement of cells.

# Chapter 4

# Materials and Methods

This chapter is dedicated to the process of CNT electrode fabrication, characterizations and electrical measurements. Each step is presented in details and the main ones are as follows: The aqueous suspensions of SWCNTs and MWCNTs, mixed with different dispersants, were spray coated on treated-COP foil. The transparency and sheet resistances of CNT multilayers were measured to find the optimum combination of CNTs and dispersant with required number of layers. The surface characterizations such as scanning electron microscopy, atomic force microscopy, and profilometry were applied on CNTs to study their surface topography. Different cell-based assays such as viability assay and immunostaining were applied to reveal the biocompatibility of CNTs and the quality of their microscopic images. Fluorescence spectroscopy and cell culturing were also performed for different photoresists to select a biocompatible photoresist with lowest auto-fluorescence for the electrode fabrication. Finally, the CNT electrode arrays were fabricated by spray coating and photolithography techniques. The subsequent electric cell–substrate impedance sensing measurements were combined with optical microscopy of cells grown on the fabricated electrode arrays.

## 4.1 Fabrication of Electrode Arrays

### 4.1.1 Spray Coating of CNTs

To prepare CNTs for spray coating, they were mixed with the following dispersants in aqueous suspensions as follows: The SDS and CMC were dissolved in deionized (DI) water to obtain 1 and 0.5 wt% solutions, respectively and stirred overnight at 1200 rpm. These chemicals reduces the surface tension of water in which CNTs are dispersed. Afterwards, 60 mg of MWCNTs (Hanos CM-250, Hanwha Chemical, Seoul, South Korea) was mixed with 60 g of SDS solution to obtain the final concentration of 0.1 wt% MWCNT/SDS suspension. SWCNT (Carbon Solutions, Inc., California, USA) suspensions were prepared in SDS and CMC dispersant solutions with 0.03 wt% final concentration for both dispersants. The mixture of CNTs and dispersant solutions were carried out in the glove box under nitrogen ($N_2$) atmosphere. The suspensions were sonicated using a horn sonicator (Branson Sonifier S-450D, Connecticut, USA) at amplitude levels alternating between 200 and 120 W in 5 min intervals for a total time of 30 and 15 min for SDS and CMC dispersants, respectively. Sonication was performed, in an ice water bath, to disperse the CNTs homogeneously in dispersant solutions. Then they were centrifuged at speed of 15000 rpm for 1.5 h to remove the aggregated CNTs. 80 % of centrifuge solution was taken from top as final solution for spray coating, and stored at room temperature (RT) before use.

A transparent atmospheric-pressure plasma-treated cyclic olefin polymer (*treated−COP*) foil with thickness of 188 $\mu$m was selected as a substrate to fabricate the electrode arrays. This polymer is flexible, biocompatible and suitable for cell culturing applications. A gold electrode pattern was deposited on the substrate

through a shadow mask by physical vapour deposition technique (Figure 4.1 a, right side). The areas of working electrodes were etched away by gold etchant for 1 min, washed with enough amount of DI water, and dried with nitrogen stream (Figure 4.1 a, left side). A shadow mask was fixed onto the gold-patterned substrate (Figure 4.1 b), and then the counter electrodes and wires were covered with tape to prevent spray coating of CNTs on these areas and to coat the CNTs only on working electrodes areas (Figure 4.1 c). For characterization experiments, CNTs were spray coated over the whole surface area of treated-COP substrates ($2.5 \times 2.5\,cm^2$) without using the mask.

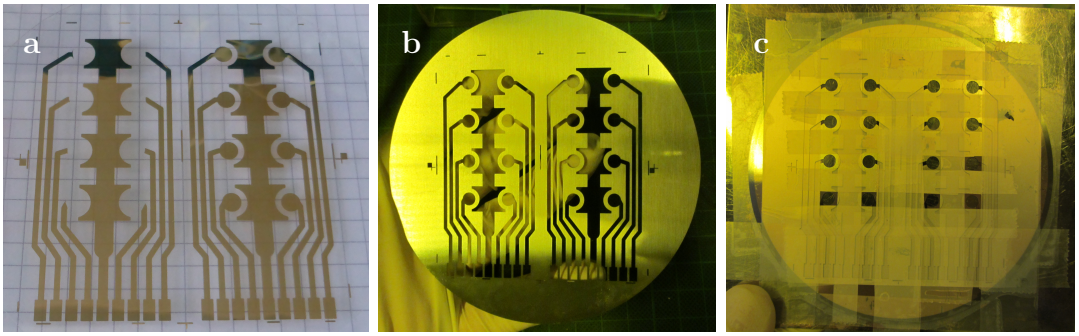


Figure 4.1: The gold electrode pattern on treated-COP foil (a, right side) with etched working electrode areas (a, left side); (b) The mask for CNT spray coating, (c) which was placed over the substrate and taped to spray-coat CNTs only on working electrode areas. (b) adapted from (Teymouri et al. [2019]) with permission, ©2019 Copyright The Materials Research Society.

The spray coating technique was used to deposit CNTs on the substrates in different layers. In this technique, an industrial air atomizing spray valve (Nordson EFD, USA) mounted on an automated overhead motion platform was used to generate fine droplets of a water-based carbon nanotube ink. Spray parameters such as atomizing gas ($N_2$) pressure, orifice opening, material pressure, and spray valve to substrate distance were optimized in other studies to obtain uniform

CNT layers (Abdellah et al. [2011],Abdellah et al. [2013], Loghin et al. [2016]). The spray coating parameters used in this study are presented in Table 4.1. Several spray cycles were performed to achieve CNT multilayers. MWCNT:SDS and SWCNT:SDS suspensions were spray coated in 20, 40, 60 and 80 layers. SWCNT:CMC suspension was spray coated in 10, 20, 30, and 40 layers. One of the issues in spray coating of MWCNT:SDS and SWCNT:SDS suspensions was that in spray coating the nozzle had to be purged after spray coating of every 5 layers. Substrates were heated up to 63 and 80 °C during spray coating of CNT suspensions with SDS and CMC dispersants, respectively.

Table 4.1: The parameters for spray coating of CNT layers

| CNT:Dispersant | MWCNT:SDS | SWCNT:SDS | SWCNT:CMC |
|---|---|---|---|
| Atomizing gas pressure (Mpa) | 0.05 | 0.05 | 0.5 |
| Material pressure (Mpa) | 0.04 | 0.03 | 0.4 |
| Valve to substrate (mm) | 50 | 50 | 50 |
| Speed (mm/s) | 200 | 200 | 150 |
| Number of CNT layers | 20-80 | 20-80 | 10-40 |

After spray coating, the samples with CNT:SDS layers were immersed in DI water between 15 to 30 min to remove the SDS from deposited layers and dried at 40 °C. The samples with CNT:CMC layers were immersed in $HNO_3$:DI water (1:4) solution overnight and dried at 70 °C. Afterwards, they were washed in DI water for 5 min and heat-treated at 90 °C for two hours to remove the possible residues of CMC and the weakly absorbed $HNO_3$. The COP foil was chemically resistant to the acid treatment. Even though the dispersants were washed away and removed from CNT layers, the characterization samples and electrode arrays are named based on the CNT suspensions that have been used for spray coating, as SWCNT:SDS, MWCNT:SDS, and SWCNT:CMC with the number of layers.

### 4.1.2 Photoresist Coating and Photolithography

After the spray coating process, the spray coated CNT layers were covered with upside down tape to protect CNTs from oxidation in plasma treatment step. The whole electrode array except the covered CNT layers was oxygen plasma treated in a Faraday cage for 12 s at $O_2$ pressure of 0.4 mbar and generator power of 90 W using the Femto low-pressure plasma system (diener electronic GmbH, Ebhausen, Germany). The mild plasma treatment changed the hydrophobic surface of gold to hydrophilic surface. This improved the surface adhesion of gold and allowed the uniform coating of photoresist over the electrode array and substrate. However, the CNT layers were covered to prevent their sheet resistance increase during plasma treatment, which was reported by Falco et al. [2014].

Afterwards, the photoresist SU8-2 (MicroChem Corp., Massachusetts, USA) was spin coated on the array (1000 rpm) followed by soft-baking process on a hotplate (at 65 and 95 °C for 1 and 3 min, respectively) to reduce the solvent concentration in the photoresist. The array was placed in a mask aligner to align the photomask on the electrode array and exposed it to UV light (360 nm) with exposure energy of 90-105 mJ/cm$^2$. SU8-2 is a negative photoresist and it polymerizes by exposure of UV light. After exposure the array was post-baked (at 65 and 95 °C for 1 and 3 min, respectively) to complete the crosslinking in exposed areas initiated by UV exposure. The array was soaked in developer mr-Dev 600 (micro resist technology GmbH, Berlin, Germany) for 70 s to remove the non-polymerized photoresist from the working and counter electrodes, washed with isopropyl alcohol (IPA) and dried with a stream of nitrogen.

For ECIS measurements, sticky-Slide 8 Well (ibidi GmbH, Gräfelfing, Germany) was mounted on the electrode array (Figure 4.2). The eight well elec-

trode arrays were named as 8W10E and 8W1E for electrode arrays with 10 and 1 working electrodes per well, respectively (Figure 4.3). The electrodes were imaged by AMG EVOS$^{TM}$ FL microscope and the diameter of working electrodes were measured by ImageJ (image processing software, Schneider et al. [2012]).

Figure 4.2: The sticky-Slide 8 Well; The image is taken from the website of ibidi GmbH.

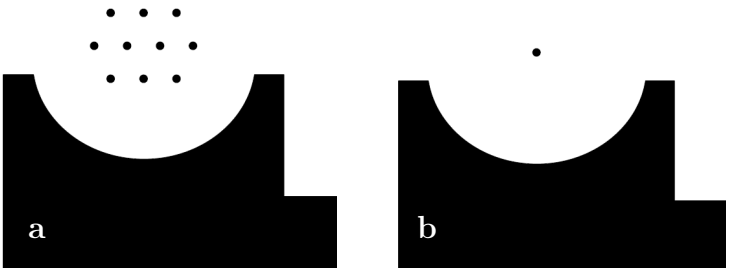


Figure 4.3: The counter electrode and the working electrodes per well, (a) ten working electrodes, and (b) one working electrode per well.

The auto-fluorescence property, thickness and biocompatibility of photoresists SU8-2, ma-N1420, and AZ4562 were studied to select a suitable photoresist for the arrays. For the characterization experiments, the photoresists were spin coated on the treated-COP substrates followed by a photolithography process. The photolithography step created polygonal patterns with surface areas between

0.03 $mm^2$ and 0.07 $mm^2$ on the photoresists that were suitable areas for measuring the thickness of the photoresist.

The positive photoresist AZ4562 (Microchemicals GmbH, Ulm, Germany) was spin coated with speed of 6000 rpm, followed by 5 min baking at 100 °C on a hotplate. The photoresist was exposed to UV light with energy exposure of 300 $mJ/cm^2$. After 2 min development in the suitable developer AZ400K, the sample was washed with DI water and dried in a nitrogen stream. The negative photoresist ma-N1420 (micro resist technology GmbH, Berlin, Germany) was coated with a spin speed of 1000 rpm, and baked on a hotplate at 100 °C for 2 min. The UV exposure was done with energy exposure of 100 $mJ/cm^2$. The photoresist was developed with ma-D 533/S developer (micro resist technology GmbH, Berlin, Germany) for 50 s, washed with DI water and dried with nitrogen.

## 4.2 Characterization of CNT Electrode Arrays

### 4.2.1 Fluorescence Spectroscopy

The auto-fluorescence properties of photoresists SU8-2, ma-N1420, and AZ4562 spin coated on treated-COP foils were compared by a spectrofluorimeter FluoroMax®3. Three ranges of excitation and emission wavelengths were selected which cover three fluorescence filter sets (Table 4.2). In each range the excitation wavelengths were scanned with 10 nm intervals and excited to the surface of photoresists. The emitted autofluorescences from the surface (in the specified emission wavelength ranges) were directed to the emission monochromator and subsequently to the detector. Afterwards, the control software represented the five excitation and emission wavelength-pairs with the highest peaks of fluorescence intensity in

each range. The treated-COP foil and air were used as controls. This technique provides information about the auto-fluorescence properties of these photoresists, which can be problematic in fluorescence microscopy of cells (Tamai et al. [2015]). The autofluorescence of photoresist can interfere with the fluorescence signals of labeled cells. This can reduce the accuracy of the observation or completely block the signal information coming from the cite-specific fluorescence labeling of cells. The fluorescence images from cells that are grown over the photoresist with high auto-fluorescence becomes blurred and the information gets hidden in the background noise (Tamai et al. [2015] and Hirai et al. [2015]).

Table 4.2: The selected ranges of excitation and emission wavelengths in fluorescence spectroscopy

| **Selected wavelength ranges** | **1** | **2** | **3** |
|---|---|---|---|
| Excitation wavelength (nm) | 380-465 | 465-532 | 532-600 |
| Emission wavelength (nm) | 380-670 | 465-600 | 532-700 |

### 4.2.2 Absorbance Spectroscopy

The transmittance spectra of spray coated CNT layers were recorded in the wavelength range of 300 - 1000 nm using a 300 W xenon arc lamp. The light was chopped at a frequency of 210 Hz by a mechanical chopper wheel and passed through an Oriel Cornerstone$^{TM}$ 260 1/4 m monochromator to narrow the bandwidth of light. The monochromatic light was illuminated to the sample and the transmitted photons were directed onto a silicon-based photodiode with a transconductance amplifier. The photodetector measured the light intensity and amplified the current signal to a voltage signal. A 70105 Oriel Merlin digital lock-in amplifier (Newport Corporation, California, USA) was used to increase the signal-to-noise ratio of a small AC voltage signal.

The amplified signals were analyzed by the data acquisition and spectroscopy software TracQ$^{TM}$ Basic. The sample and detector were placed in a covered dark box in order to avoid interference with ambient light. Prior to the measurements, the known spectral response of monochromatic light was measured to determine the amount of photons arriving at a certain distance and to ensure the calibration of setup. The transmittance spectrum of treated-COP foil was recorded as reference to determine the respective transmission of the carbon nanotube layers. The measurements were performed for different multilayers of MWCNT:SDS, SWCNT:SDS and SWCNT:CMC. CNTs were spray coated on treated-COP foil ($2.5 \times 2.5\,\mathrm{cm}^2$). The transmittance were recorded for three identical samples per each condition and represented as an average value for each wavelength.

### 4.2.3 Electrical Properties

The sheet resistance, the resistance of a thin sheet of material, was recorded using a four-point probe head (Jandel, Leighton Buzzard, UK) connected to a Keysight B2901A source measuring unit (SMU) (Figure 4.4). Using the SMU, a constant current was sourced across the sample via the two outer needles of the probe with high input impedance. The potential drop was measured across the inner two needles of the probe. A constant current of $100\,\mu\mathrm{A}$ was sourced for all measurements in single shot measurement operation mode. Different layers of MWCNT:SDS, SWCNT:SDS, and SWCNT:CMC were spray coated on treated-COP substrates and the sheet resistances were measured on the same day after the dispersants were washed away from CNT layers. The sheet resistance of SWCNT:SDS layers were compared at RT and $37\,^{\circ}\mathrm{C}$. The measurements were averaged over ten different spots on two identical samples per each condition and

represented as an average value. An indium tin oxide substrate was used as a control before the measurements.

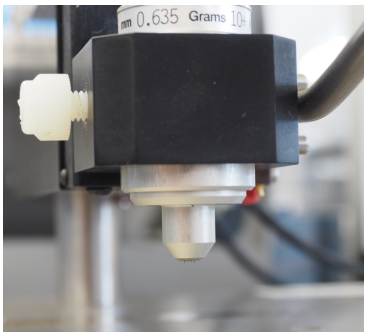


Figure 4.4: The four-point probe head used in sheet resistance measurements.

The paired t-test with two-tailed distribution was used for statistical analysis. The null hypothesis was chosen which indicates that the differences between the paired population means is equal to 0. The t value in paired t-test is calculated by the Formula 4.1:

$$t = \frac{\bar{X}_{diff}}{S_{\bar{x}}}, S_{\bar{x}} = \frac{S_{diff}}{\sqrt{n}} \tag{4.1}$$

where $\bar{X}_{diff}$ is the average of the differences between two conditions, and $S_{\bar{x}}$ is the standard error of the mean. $S_{diff}$ is the standard deviation of the differences between two conditions and n is the number of the observations in each condition. The t values are compared to the critical t values from the t-distribution table and the respective $p$–values are compared with the significance level ($\alpha$) of 0.05. The t values lower than the critical t value and the $p$–value higher than the $\alpha$ do not reject the null hypothesis and a significant difference between the two conditions can not be concluded. The t values higher than the critical t value

and the $p$–value lower than the $\alpha$ reject the null hypothesis and a significant difference between the two conditions does exist. (Kim [2015])

The sheet resistances of SWCNT:SDS, MWCNT:SDS, and SWCNT:CMC layers were measured at different time-points during 45 days. The samples were stored at RT in the open air.

## 4.3 Surface Topography of CNT Films

### 4.3.1 Surface Profilometry

The surface topography of SWCNT:SDS layers and the thicknesses of photoresists were evaluated by means of mechanical profilometry (Bruker DekTakXT). In this method, a diamond-tipped stylus moved over the sample's surface while applying a force to the surface controlled by a force compensation mechanism. The displacements of the stylus were converted to electrical signals by a linear variable differential transformer connected to the stylus. These signals provided information about the surface variations of the sample. The parameters such as stylus force on the sample surface (1 mg), Y length of scan (100 $\mu$m), and time of scan (30 s) were adjusted before the stylus scan the surface. The calibration was performed by a DektakXT drawer prior to the measurements.

The SU8-2, ma-N1420 and AZ4500 photoresists were spin-coated on treated-COP foils. By photolithography, patterns were created on photoresists to yield open areas in the treated-COP surface. The thickness of photoresists was measured around these open areas in more than 10 different spots.

The profilometry was performed for SWCNT:SDS which was spray coated in 20, 40, 60, and 80 layers on treated-COP foils. The surface roughness and

average maximum height of SWCNTs were calculated over 15 scanned areas. The skewness and kurtosis were also calculated from the height distribution which represents the symmetry of the variations about the mean line and the spikiness of the height distribution, respectively (Figure 4.5). On a surface with kurtosis of more than 3 the distribution curve has relatively many high peaks and low valleys whereas it has relatively few high peaks and low valleys as the kurtosis decreases to less than 3. The height distribution has deep scratches or peaks removed for skewness less than zero, and in positive skewness the height distribution is skewed below the average line. (Gadelmawla et al. [2002])

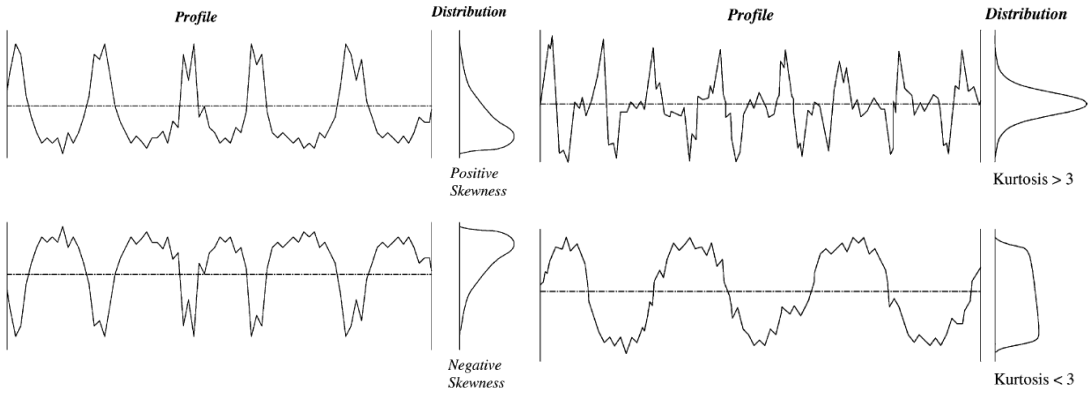


Figure 4.5: The Skewness represents the symmetry of roughness shape using the average line as the center. In skewness less than zero the height distribution is skewed above the average line, and in skewness more than zero the height distribution is skewed below the average line. The kurtosis measures the sharpness of the roughness profile. The height distribution is spiked with sharp peaks when the kurtosis is more than 3, whereas the distribution profile has relatively few high peaks and low valleys when the kurtosis is less than three. Figure adapted from (Gadelmawla et al. [2002]) with permission, ©2002 Elsevier Science B.V.

### 4.3.2 Atomic Force Microscopy

The surface morphologies of MWCNT films, spray coated on treated-COP foil, were characterized using a JSPM-5200 scanning probe microscope (JEOL, Tokyo, Japan). In each case, five areas of $4\times4\,\mu m^2$ were scanned in tapping mode under air and at RT. The silicon AFM probe (Type: Tap300DLC, Budget Sensors, Sofia, Bulgaria) coated with diamond-like-carbon on tip side of the cantilever had resonant frequency of 300 kHz, and force constant of 40 N/m. The scan rate was 1 Hz. The surface roughness (Ra) and the average maximum height of roughness profile were calculated by the Gwyddion image processing software. To compare the uniformity of MWCNT layers on treated-COP substrate, the AFM images were displayed in 3D formats.

### 4.3.3 Scanning Electron Microscopy

To compare the surface topography of CNT layers, scanning electron microscope (SEM) images were taken from different layers of MWCNT:SDS, SWCNT:SDS, and SWCNT:CMC. CNTs were spray coated on treated-COP foil. The SEM images were recorded with a field-emission scanning electron microscope (NVision 40, Carl Zeiss Microscopy GmbH, Jena, Germany) with an acceleration voltage of 7 kV and an extractor voltage of 5 kV. The working distance was adjusted in a range of 5 to 5.5 mm. In this technique, a focused high-energy beam of electrons was directed to the surface of the sample. The interaction of the incident beam with the valence electrons of the constituent atoms in the sample generated the secondary electrons, which were detected by the detector and provided information about the surface topography of CNT layers.

## 4.4 Cell Culture

### 4.4.1 Cell Morphologies on Photoresists

The L929 mouse fibroblasts and MCF7 human breast adenocarcinoma cell line were used for the cell-based assays. The L929 cells were purchased from DSMZ (Braunschweig, Germany). The MCF7 cells were supplied by CLS GmbH (Eppelheim, Germany).

To determine the biocompatibility of the photoresists, SU8-2, ma-N1420 and AZ4500 were spin-coated on treated-COP foils. The photolithography technique was used to remove the photoresist in some areas and the sticky-Slide 8 Well was attached on top of the photoresist. This allowed cells to adhere to photoresist layers as well to the treated-COP areas in each well. The treated-COP areas in each well were considered as control because the L929 cells grow on treated-COP with fibroblast-shaped morphology which is considered as normal morphology.

The L929 cells were seeded on photoresist samples with initial cell concentration of $4\times10^3$ cells/cm$^2$ in RPMI 1640 medium supplemented with 10 % fetal bovine serum and 1 % penicillin-streptomycin (P/S). Table 4.3 represents the components of the RPMI 1640. The samples were incubated for five days at 37 °C in a 5 % $CO_2$ atmosphere and phase contrast images were taken on third and fifth days with AMG EVOS$^{TM}$ FL microscope. Also, L929 cells were seeded ($7.5\times10^3$ cells/cm$^2$) on fibronectin coated (1.5 $\mu$g/cm$^2$) SU8-2 and ma-N1420 photoresists and they were imaged after two days incubation at 37 °C in a 5 % $CO_2$ atmosphere.

Table 4.3: The components of the RPMI 1640 Sigma-Aldrich [2019b]

| Components | RPMI 1640 (g/L) |
|---|---|
| $MgSO_4$ (anhydrous) | 0.05 |
| $Ca(NO_3)_2.4H_2O$ | 0.1 |
| $NaHCO_3$ | 2.0 |
| $Na_2HPO_4$ (anhydrous) | 0.8 |
| NaCl | 6.0 |
| KCl | 0.4 |
| $KH_2PO_4$ | – |
| Amino acids | ✓ |
| Vitamins | ✓ |

### 4.4.2 Viability Assay

The viability assay was performed to observe the live and dead cells grown on the surface of SWCNT:CMC (20 layers) electrode. Fluorescein diacetate (FDA) and propidium iodide (PI) were used to stain the viable and nonviable cells, respectively. The MCF7 cells were cultured with an initial cell concentration of $2\times10^4$ cells/cm$^2$ and incubated at 37 °C in a 5 % $CO_2$ atmosphere. After three days, 30 $\mu$M of FDA and 20 $\mu$M of PI in RPMI 1640 (supplemented with 200 mM L-glutamine without phenol red) were added to the cells and incubated for 4 min. The staining solution was washed away by PBS and replaced by RPMI 1640 without phenol red. Afterwards, images were captured with a Nikon ECLIPSE Ti microscope.

### 4.4.3 Immunofluorescence Assay

The following immunofluorescence protocols were carried out to compare the quality of fluorescence microscopy images on 80 layers of SWCNT:SDS, 20 layers of SWCNT:CMC, and gold electrodes.

MCF7 cells were cultured on electrode array of SWCNT:CMC with 20 layers. After a day, cells were fixed with formalin solution (containing 10 % formalin and 4 % formaldehyde) for 30 min at RT. For permeabilization, PBS containing 0.1 % Triton X-100® and 10 % (v/v) FCS was added to the cells for 30 min. The cells were then blocked with PBS containing 1 % bovine serum albumin (BSA) and 0.2 % Triton X-100® to avoid nonspecific antibody bindings. Primary antibody incubation was done in 1 % BSA–0.05 % Triton X-100®-PBS, with monoclonal mouse anti-$\alpha$-tubulin (1 $\mu$l/ml) overnight at 4 °C. Afterwards, cells were incubated in anti-mouse IgG-Atto 594 secondary antibody (1 $\mu$l/ml) and DAPI in 1 % BSA–0.05 % Triton X-100®–PBS for 1 h. The images were taken with a Nikon ECLIPSE Ti microscope.

The effect of the auto-fluorescence properties of photoresist ma-N1420 on fluorescence microscopy images was examined. The L929 cells were cultured with an initial concentration of $3\times10^4$ cells/cm$^2$ on a 8W10E electrode array of MWCNT:SDS passivated with ma-N1420 photoresist. After four days, cells were fixed with formalin solution and subsequently permeabilized with PBS containing 0.5 % Triton X-100® for 5 min. The blocking buffer of 1 % BSA in PBS was added to the cells, followed by incubation in 0.5 % BSA–PBS containing phalloidin (Alexa Fluor® 660) and DAPI for one hour. The images were taken with a Nikon ECLIPSE Ti microscope. In addition, the same immunostaining protocol with DAPI and phalloidin was performed for L929 cells cultured on the 8W10E electrode array with 80 layers of SWCNT:SDS for one day.

The MCF7 cells were also cultured ($15\times10^4$ cells/cm$^2$) on electrode array of SWCNT:CMC 20 layers without pre-coating of the wells. The wells were washed gently three times with PBS to compare the stability of cells grown on pre-coated and non-coated SU8-2 and SWCNT:CMC surfaces.

## 4.5 Impedimetric Measurements and Optical Microscopy

The 8W1E electrode arrays of SWCNT:CMC 20 layers with SU8-2 photoresist were fabricated as explained in section of 4.1. The wells were pre-coated with collagen IV (1.5 $\mu$g/cm$^2$). The MCF7 cells (with different initial cell concentrations of $2\times10^4$ and $15\times10^4$ cells/well) were seeded to observe the cell proliferation or to perform the wound healing assay. The wells without cells were used as the control. The cell culture medium of RPMI 1640 medium supplemented with 10 % fetal bovine serum and 1 % P/S was used for MCF7 cells and control wells. The impedimetric measurements were done in multiple frequencies (eleven default frequencies) in the range of 62.5 Hz to 64 kHz. The ECIS® cultureware 8W1E was used as control array, made of gold electrodes.

The impedimetric measurements were combined with live microscopy of cells growing on the electrodes. A home-made array holder was designed at ibidi GmbH suitable for electrical measurements and at the same time suitable for optical microscopy (Figure 4.6). For electrical measurements the electrode array was placed in this array holder that was connected to the ECIS® array station. For optical microscopy the array holder was located on the imaging stage of a Nikon ECLIPSE Ti microscope. The array holder was connected to the Heating and Gas Incubation Systems (ibidi GmbH) to provide the required temperature of 37 °C and 5 % $CO_2$ for cell growth during the microscopy and measurements.

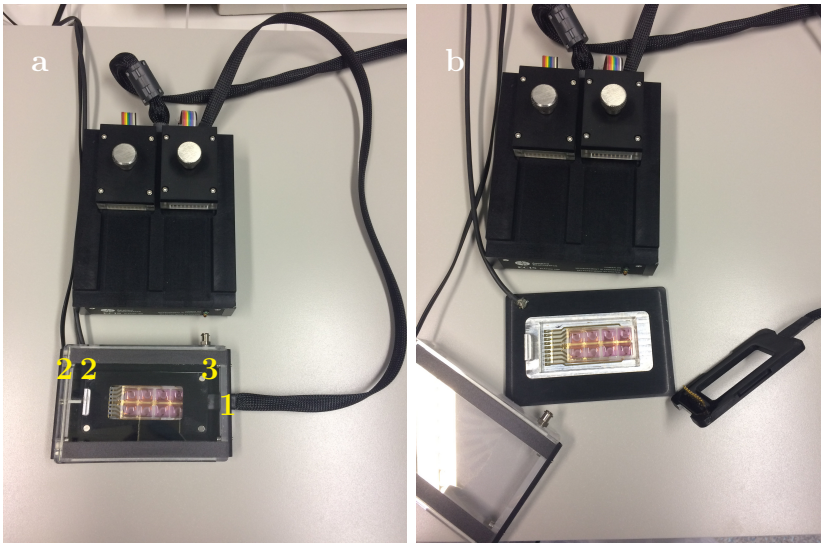


Figure 4.6: (a) The home-made array holder that is connected to the array station for ECIS measurements via port 1. For optical microscopy the array holder is placed on the imaging stage of microscope. The array holder connects to the ibidi Heating System and ibidi Gas Incubation System via ports 2 and 3, respectively. (b) The array holder is opened.

# Chapter 5

# Results and Discussions

In this study, it was investigated how CNT thin films can be optimized to be used in an electrode array for impedimetric measurement of cells. For this purpose, CNTs were tested in different dispersants to find an optimum combination suitable for spray coating of CNTs as working electrodes. Different characterization methods were applied to choose CNT films with high transparency, low sheet resistance, and surface uniformity. Additional studies related to the photoresists, such as auto-fluorescence properties, biocompatibility, and photoresist thickness were performed. Finally, the electrode arrays made of CNT working electrodes were fabricated, followed by impedimetric measurements accompanied with cell microscopy. The CNT electrodes improved not only the quality of cell microscopy images, but also the electrical recordings remained comparable with the recordings achieved by gold electrodes. In this chapter, all results related to the fabrication of electrodes, characterizations, cell microscopy, and impedimetric measurements are presented. The work that is presented in the following is substantially adapted from a previous publication authored by (Teymouri et al. [2019]).

## 5.1 The CNT Electrode Array

The electrode array established in this study is shown in Figure 5.1. The working electrodes were made of CNT multilayers. The substrate was a plasma treated-COP foil. The wires and counter electrodes were made of gold layer with 30 nm thickness. The transparent SU8-2 photoresist was spin-coated on the array and the patterns of counter and working electrodes were created by the photolithography technique. The final electrode array was assembled with a sticky-Slide 8 Well mounted on top for cell culture studies and ECIS measurements. The working electrodes were imaged by an AMG EVOS$^{TM}$ FL microscope (Figure 5.2) and the diameter of the electrodes was measured by ImageJ. The diameter of working electrodes were 244.5 ($\pm$ 8.87) $\mu$m (n=10).

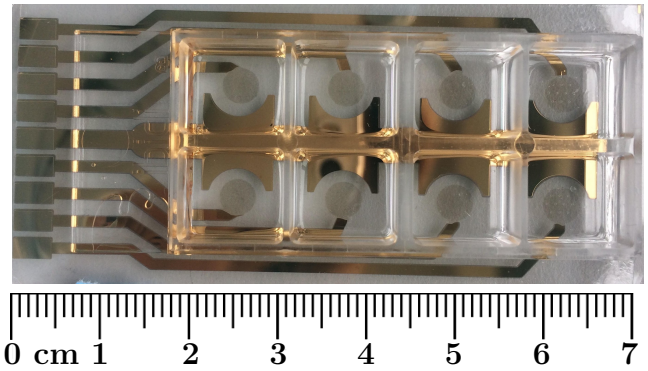


Figure 5.1: The CNT electrode array made by spray coating of CNTs as working electrodes. The counter electrodes and wires were made of gold. A sticky-Slide 8 Well was mounted on top. Figure adapted with changes from (Teymouri et al. [2019]) with permission, ©2019 The Materials Research Society.

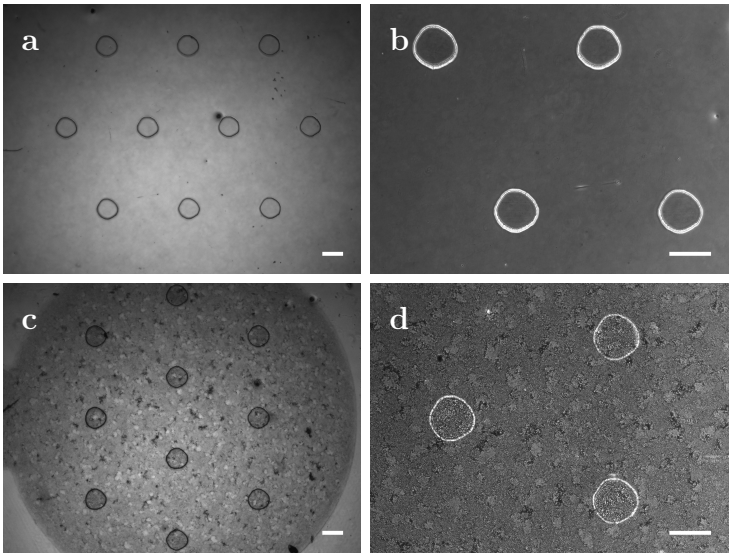


Figure 5.2: The working electrodes made of (a, b) 8W10E SWCNT:CMC 20 layers and (c, d) 8W10E SWCNT:SDS 80 layers, surrounded by transparent SU8-2. The patterns were created by photolithography. All the scale bars are 250 $\mu$m.

## 5.2 The Photoresist Characterization

The positive photoresist AZ4562 and negative photoresists ma-N1420 and SU8-2 were spin-coated on treated-COP foil. Some patterns were created in the photoresists by photolithography to remove the negative photoresists or to polymerize the positive photoresist in these areas to allow for the measurement of the thickness of the different photoresists. The thickness measurements were performed by a profilometer and the results are presented in Table (5.1). The SU8-2 had an average thickness of 4.1 $\mu$m close to the average thickness of the photoresist (4.0 $\mu$m) that is used in the commercial ECIS® cultureware (Applied BioPhysics, Inc.). The thickness of AZ4562 layer was high enough for cells to slow down the cell coverage on top of photoresist layer in the first days. The related results are presented later in this chapter (section of cell morphology on photoresists).

Table 5.1: The average thicknesses of photoresists spin-coated on treated-COP foil. (n=10)

| Photoresist | Average Thickness ($\mu$m±STD) |
|---|---|
| SU8-2 | 4.1 ± 0.3 |
| ma-N1400 | 2.8 ± 0.2 |
| AZ4562 | 8.5 ± 0.2 |
| ECIS® Photoresist | 4.0 ± 0.03 |

### 5.2.1 Fluorescence Spectroscopy

To compare the auto-fluorescence properties among the photoresists, the fluorescence spectrum of photoresists were recorded (Cao et al. [2012] and Pai et al. [2007]). The photoresists were exposed to three ranges of excitation wavelengths and the maximum emitted fluorescence intensities from the surface of the photoresists were detected. Figure 5.3 represents the maximum fluorescence intensities that were recorded in each range. The fluorescence intensities show the different auto-fluorescence properties of photoresists. The ma-N1420 had higher fluorescence intensities than the other photoresists in wavelengths 400 to 700 nm, which indicates that this photoresist shows more auto-fluorescence properties compared to the other photoresists. The fluorescence intensities detected from ma-N1420 in wavelenghts before 500 nm were higher than intensities in the region of 500 to 700 nm.

It is noticeable that the fluorescence intensities detected from the surface of SU8-2 were even lower than the intensities detected from the surface of treated-COP. As high quality fluorescence images could be obtained from cells grown on treated-COP substrate, the achievement of high quality fluorescence cell images on SU8-2 surface were expected. The related results are provided in following sections. AZ4562 also had low fluorescence intensities in 400 - 600 nm range and

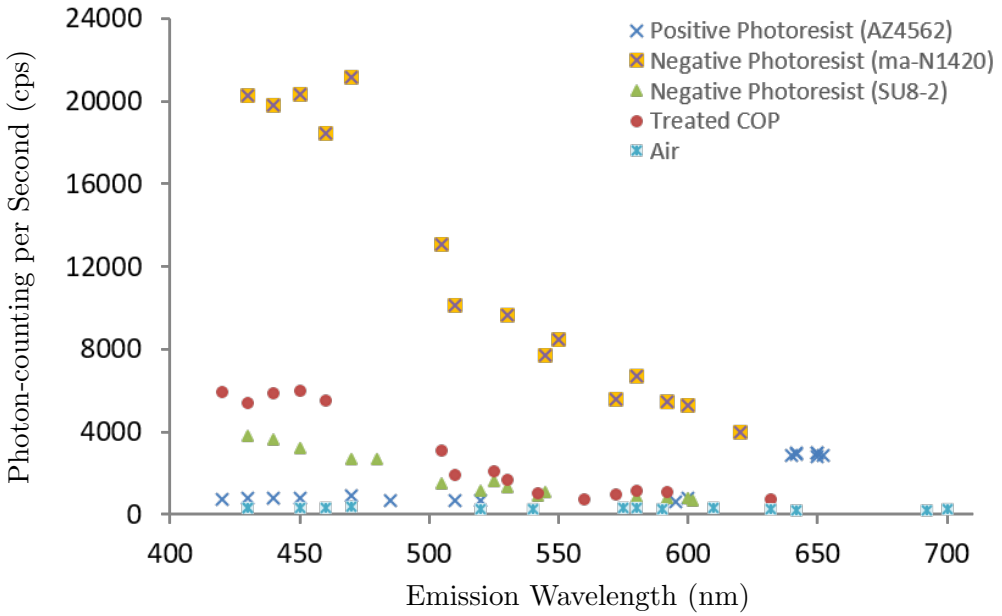


Figure 5.3: The fluorescence intensities of photoresists AZ4562, ma-N1420, and SU8-2 excited in wavelenghts of 380 - 600 nm.

showed slightly increase in emission intensities after 600 nm.

To show the effect of auto-fluorescence properties in fluorescence microscopy, the immunostaining of L929 cells cultured on ma-N1420 was studied. The ma-N1420 photoresist was spin-coated on MWCNT:SDS multilayers and the surface of MWCNTs were open in some areas by a photolithography process. L929 cells grown on ma-N1420 and MWCNT layers were stained with DAPI and phalloidin (Figure 5.4 a). DAPI labeled the nuclear DNA of cells and phalloidin stained the actin filaments of cells. It was observed that the nuclei of cells grown on photoresist areas were blurred, whereas the nuclei of cells over CNT layers were clearly visible (Figure 5.4 b). The actin filaments of cells grown on photoresist had lower signal intensities compared to the actin filaments of cells grown on CNT layers (Figure 5.4 c). In fact, the immunostaining and the fluorescence spectroscopy results both indicated that the ma-N1420 was not a suitable photoresist for pas-

sivation of SWCNT electrode array.

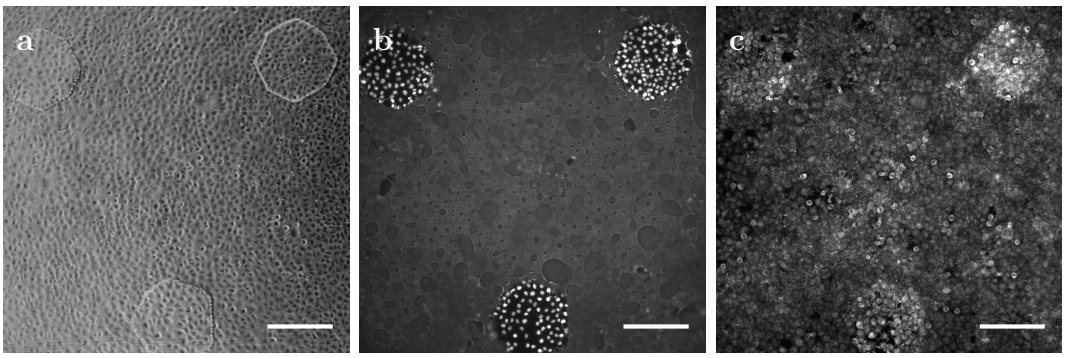


Figure 5.4: (a) Phase contrast image of L929 cells cultured on ma-N1420 and MWCNT:SDS surfaces after four days. Inside the patterns the CNT layers were open and the rest of the surface was coated with ma-N1420. The fluorescence images of (b) nuclei of cells stained with DAPI and (c) actin flaments of cells stained with phalloidin. Only nuclei of cells grown on CNT layers were visible in image b. The fluorescence intensities of actin filaments were stronger for cells grown on CNT multilayers than for cells grown on photoresist layer. The scale bars are 250 $\mu$m.

### 5.2.2 Cell Morphology on Photoresists

In bioapplications, the photoresist must not be toxic for cells and does not cause cell lysis (death) or inhibit the cell proliferation during the cell growth (Wang et al. [2013a]). In this regard, the direct and indirect cell-substrate contact tests were both carried out by seeding the L929 cells directly on top of the several photoresists as well on the treated-COP layer in the same wells. The photoresists were spin coated on treated-COP foil and the sticky-Slide 8 Well was mounted on top for cell culturing. L929 cells were cultured on the photoresists with open patterns that enabled monitoring of cells on the photoresist layer beside the treated-COP surface in one well. The phase contrast images were taken on third and fifth days after cell seeding (Figure 5.5).

It was observed that the L929 cells grew with fibroblast-shaped morphology on treated-COP surface next to the SU8-2 photoresist layer after three days (Figure 5.5 a). However, they grew with round and elongated morphologies on SU8-2 which resulted in the formation of cell clumps after five days (Figure 5.5 d). On the ma-N1420 layer as well as the treated-COP surface, cells had round and elongated morphologies after three days and formed clumps of cells after five days (Figure 5.5 b and e). On the positive photoresist AZ4562 with 8.5 $\mu$m thickness, cells did not cover the surface of photoresist after three days while they formed a confluent layer on surrounding treated-COP areas (Figure 5.5 c). At the end, cells covered the surface of the AZ4562 photoresist with normal morphology after five days (Figure 5.5 f).

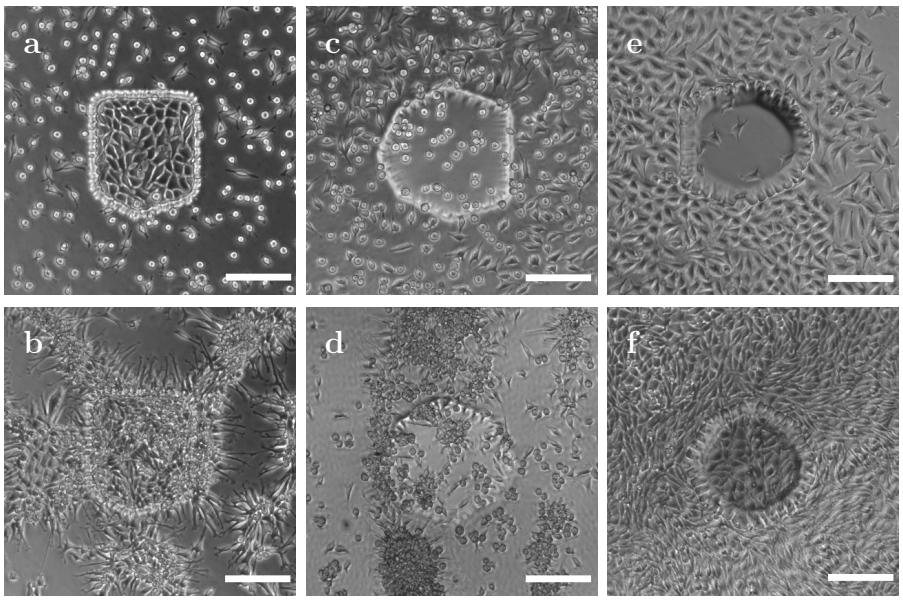


Figure 5.5: L929 cells cultured on (a, b) a treated-COP substrate surrounded by SU8-2, (c, d) treated-COP substrate surrounded by ma-N1420, and (e, f) AZ4562 surrounded by treated-COP substrate. The images in the first and second rows were taken after 3 days and 5 days, respectively. The scale bars are 150 $\mu$m.

Oh and Lee [2013] and Liberio et al. [2014] have shown that the lack of binding

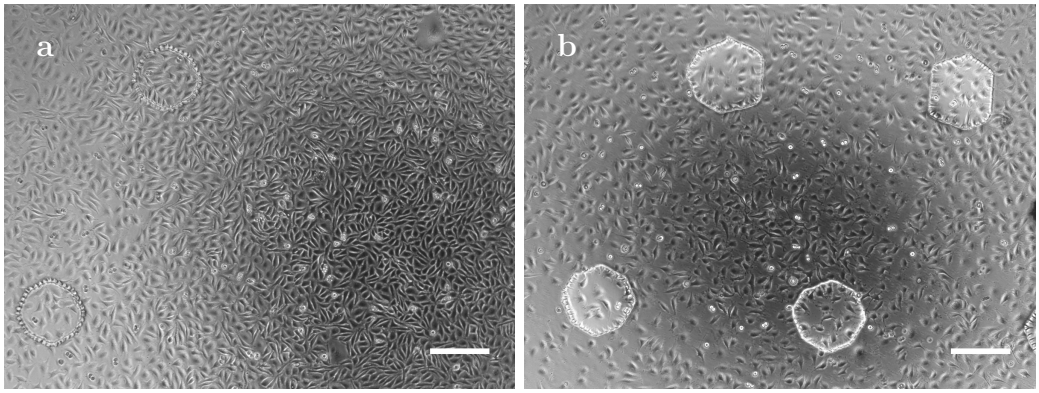


Figure 5.6: Phase contrast images of L929 cells grown on (a) SU8-2 and (b) ma-N1420 layers. The photoresists were pre-coated with fibronectin before cell seeding. Inside the patterns the treated-COP layers were open. The scale bars are 250 $\mu$m. (a) adapted from (Teymouri et al. [2019]) with permission, ©2019 The Materials Research Society.

sites on the substrate for cell attachment can alter the morphology of cells to round-shape morphology. Dai et al. [2016] have shown that the pre-coating of SU-8 with fibronectin makes the photoresist suitable for cell attachment. Xue et al. [2014] have also shown that the fibronectin created higher protein adsorption to the SU-8 surface compared to collagen type I. They showed that the better affinity of covalently coated fibronectin caused higher mesenchymal stem cells density on SU-8 surface after several days. Therefore, the photoresists SU8-2 and ma-N1420 were pre-coated with fibronectin prior to the cell seeding. It was observed that the L929 cells grew with unaltered morphologies on the surface of both photoresists SU8-2 and ma-N1420 as well as the surrounding treated-COP areas (Figure 5.6). However, the SU8-2 layer was more populated with cells than the ma-N1420 photoresist after two days.

## 5.3 Characterization of CNT layers

### 5.3.1 Transparency and Sheet Resistance

MWCNT:SDS, SWCNT:SDS, SWCNT:CMC were spray coated on treated-COP foil with different numbers of total layers. MWCNT:SDS and SWCNT:SDS had 20, 40, 60, and 80 layers whereas the SWCNT:CMC was spray coated in 10, 20, 30, and 40 layers. The transmittance data of CNT layers, recorded from 300 to 800 nm wavelengths, is presented in Figure 5.7. The results showed that CNTs have an optical transparency in the visible wavelength region.

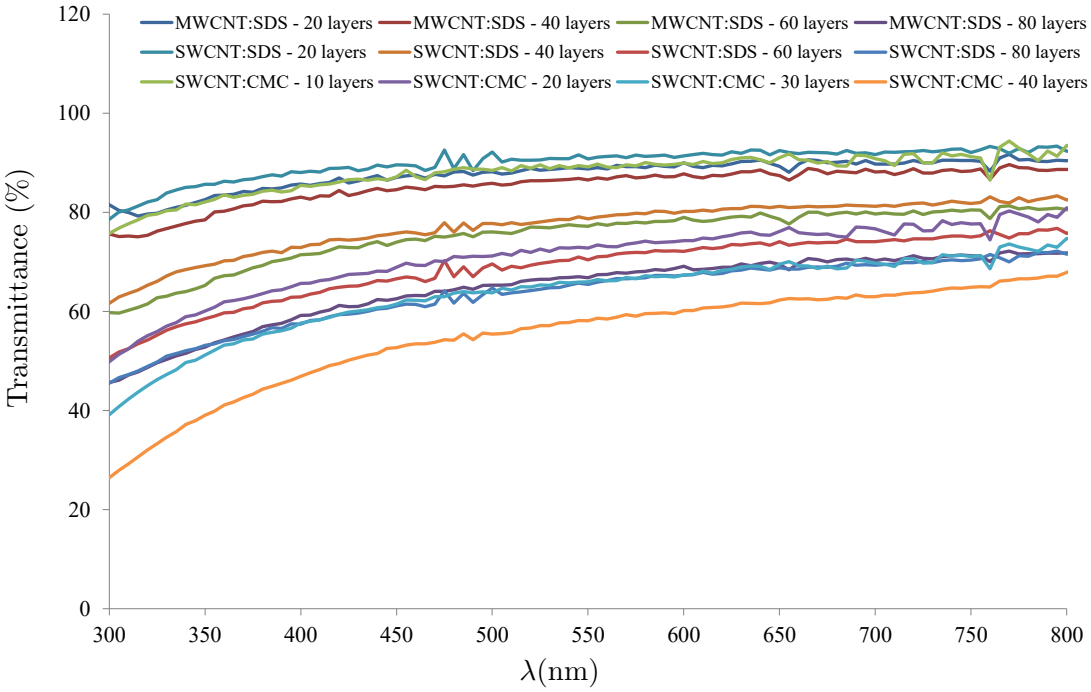


Figure 5.7: The average values of transmittance for MWCNT:SDS and SWCNT:SDS spray coated in 20, 40, 60, and 80 layers, and SWCNT:CMC spray coated in 10, 20, 30, and 40 layers (n=3).

The transmittance at wavelength 550 nm were selected to compare the transparency of CNT multilayers. The selection of this wavelength is common in most

of the current literature for characterization of optical properties of CNT films (Yu et al. [2016]). In Figure 5.8, transmittances are plotted against the respective sheet resistance of each sample. It was observed that the transparency and sheet resistance of MWCNT and SWCNT films decreased as the number of CNT layers increased. The transmittance of MWCNT:SDS films with 20 to 80 layers decreased from 89 % to 67 %, and the sheet resistances changed from 13.33 kΩ/sq to 2.78 kΩ/sq. In SWCNT:SDS, the transmittance of film with 20 layers was 91 %, while it reached to 66 % for 80 layers with the minimum sheet resistance of 694 Ω/sq in this group. In SWCNT:CMC, the sheet resistance for film with 40 layers reached to 119 Ω/sq (58 % transparency) and it increased to 270 Ω/sq for 20 layers with transparency of 73 %.

The sheet resistance of SWCNT:SDS films were lower than the sheet resistance of MWCNT films with the same number of layers. This could be due to the fact that the SWCNTs have lower diameter than that of MWCNTs. Therefore, the amount of SWCNTs in a number of spray coated layers was higher than the amount of MWCNTs in the same number of layers and consequently the conductivity of SWCNT layers increased. The number of CNT layers also affected the transparency of thin CNT film. The transparency of SWCNT:SDS and MWCNT:SDS films decreased with rising numbers of layers as there were more CNTs coated on the substrate in higher layer numbers. The transparency of SWCNT:SDS films, after spray coating of 40 layers, were lower than the transparency of MWCNT:SDS films with the same number of CNT layers. However, the transparency of SWCNT:SDS 60 and 80 layers were still acceptable for optical microscopy within the range of 60 % to 70 %.

The sheet resistances of SWCNT:CMC films were considerably lower than the sheet resistance of SWCNT:SDS and MWCNT:SDS films. In the final washing

step, $HNO_3$ was used to remove CMC from SWCNT layers overnight. Before acid treatment, the CNT layers were electrically insulated as they were encapsulated in polymer matrix of CMC (Tenent et al. [2009]). Due to the CMC removal, the thickness of CNT layers collapses and the CNT-CNT junctions and electrical percolation networks are formed and the CNT layers become highly conductive (Tenent et al. [2009]). Simultaneously, the $HNO_3$ unintentionally dopes the CNTs which can reduce the sheet resistance of SWCNT:CMC layers (Falco et al. [2014], Hu et al. [2010], Loghin et al. [2016] and Jackson et al. [2008]). The doping enhances the charge carrier density and decreases the contact resistance of CNT-CNT junctions (Zhou and Azumi [2016]).

The sheet resistances and transmittances in Figure 5.8 were fitted in Matlab to the Tinkham's formula (Tinkham [1956]),

$$T = (1 + \frac{Z_0}{2R_s}.\frac{\sigma_{op}}{\sigma_{dc}})^{-2} \tag{5.1}$$

where T and $R_s$ represent transmittance and sheet resistance, respectively. $Z_0$ is the impedance of free space and equal to $120\pi$. The $\sigma_{dc}$ is the electrical conductivity (assumed to be independent of thickness) and $\sigma_{op}$ is the optical conductivity of the CNT layers. The ratio between the latter two parameters is referred as $\gamma$, which enables to compare the sheet resistances and transmittances of CNT layers. $\gamma$ is a figure of merit to quantify the performance of a transparent conducting material. (Hirai et al. [2015] and Falco et al. [2014]) The low value of $\gamma$ indicates that the CNT film has higher sheet resistance at a given transmittance.

The MWCNT:SDS film had the lowest $\gamma$ of 0.24, and the $\gamma$ of SWCNT:SDS and SWCNT:CMC films were 0.95 and 2.94, respectively. It is noticeable that the SWCNT:CMC films were even spray coated in a lower number of layers compared

to MWCNT:SDS and SWCNT:SDS films.

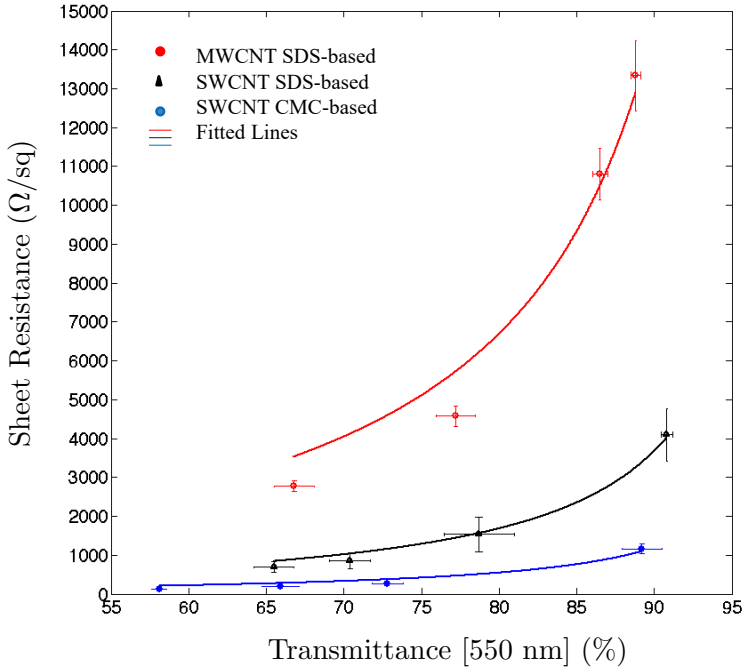


Figure 5.8: The transmittance (n=3) and sheet resistance (n=15) of MWCNT:SDS and SWCNT:SDS films spray coated in 20, 40, 60, and 80 layers, and SWCNT:CMC films spray coated in 10, 20, 30, and 40 layers. The sheet resistance was measured at RT after the dispersants were washed away. The dispersants were removed on the same day or the day after spray coating. Figure adapted from (Teymouri et al. [2019]) with permission, ©2019 The Materials Research Society.

To analyze the effect of temperature, sheet resistance was measured for SWCNT:SDS films at RT and 37 °C. The values are presented in Figure 5.9. The sheet resistances of all CNT layers decreased slightly when the temperature of the samples increased to 37 °C. However, there were no significant differences between the sheet resistances measured at RT or at 37 °C in each category ($\rho$>0.05). The 20 layers of CNT showed a tendency of lower sheet resistance at higher temperature which was a non-significant difference according to the paired t-test. Therefore, all the sheet resistance measurements presented in this work were performed at

RT.

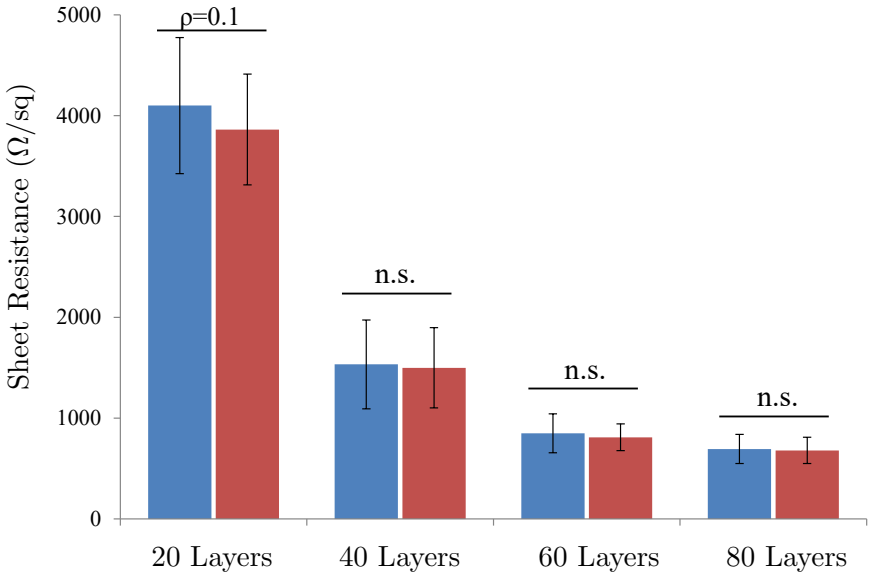


Figure 5.9: The sheet resistances of different layers of SWCNT:SDS (20, 40, 60, 80 layers) spray coated on treated-COP substrate. The measurements were done at RT and 37 °C. n.s.=non-significant (n=15). Figure adapted with changes from (Teymouri et al. [2019]) with permission, ©2019 The Materials Research Society.

During the spray coating, the CNTs formed clumps in the valve of the nozzle and the spray coating of 80 layers of MWCNT or SWCNT mixed with SDS dispersant was time-consuming. The SWCNT:CMC did not form clumps in the nozzle and the spray coating process of 40 layers was carried out without purging the valve.

The MWCNT:SDS, SWCNT:SDS, and SWCNT:CMC multilayer were stored at RT in open air for 45 days and the sheet resistance was measured at different time-points (Figure 5.10). It was observed in all groups that sheet resistances of CNT multilayers with high number of layers followed a stable behavior during 45 days. MWCNT:SDS (60, 80 layers), SWCNT:SDS (60, 80 layers), and SWCNT:CMC (20, 30, 40 layers) were the selected films with mainly constant

sheet resistance in this incubation time.

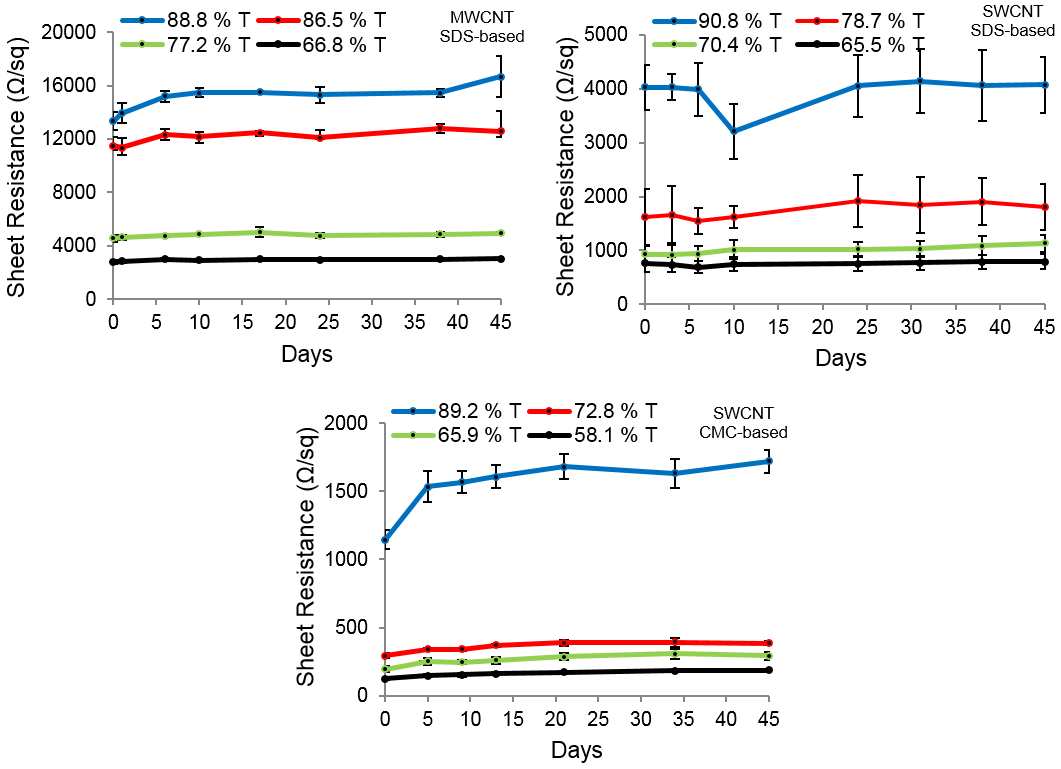


Figure 5.10: The sheet resistances of MWCNT:SDS and SWCNT:SDS films (20, 40, 60, and 80 layers), and SWCNT:CMC films (10, 20, 30, and 40 layers) spray coated on treated-COP substrate. The samples were stored in dry condition at RT. Error bars represent standard deviation of each group. (n=15)

## 5.4 Surface Topography of CNT Films

### 5.4.1 Atomic Force Microscopy

The surface topography of spray coated MWCNTs on treated-COP foil was observed by atomic force microscopy. The morphology of 20, 40, 60, and 80 layers of MWCNTs in 2D and 3D is demonstrated in Figures 5.11 and 5.12. The surface roughness and the average maximum height of the roughness profile is presented in Figure (5.13). It was observed that bundles of CNTs were created randomly on the substrates coated with 40, 60, and 80 layers of CNTs (Figure 5.11). The number of spray-coated CNT layers effected the homogeneous distribution of CNTs on the treated-COP substrate. CNT films with 60 and 80 layers covered the substrates more uniformly compared to the films with 20 and 40 layers, where the CNTs covered the substrates partly (Figure 5.12). The surface roughness of MWCNT:SDS films increased as the number of CNT layers increased (Figure 5.13). The 20 layers of MWCNTs showed a surface roughness of 14 nm, while it increased to 31 nm for 80 layers. The average maximum height of the layers also increased from 110 nm for 20 layers to 240 nm for 80 layers (Figure 5.13).

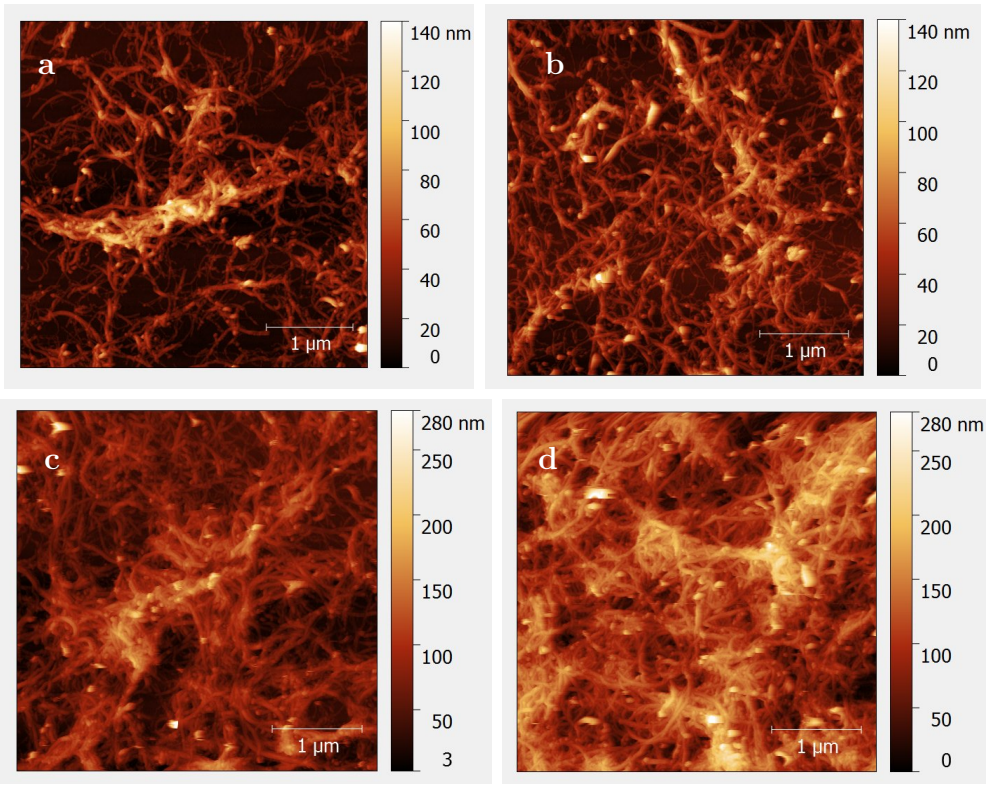


Figure 5.11: The AFM images of MWCNT:SDS films spray coated on treated-COP foil in different layers, (a) 20 layers, (b) 40 layers, (c) 60 layers, and (d) 80 layers. The scale bars are 1 $\mu$m.

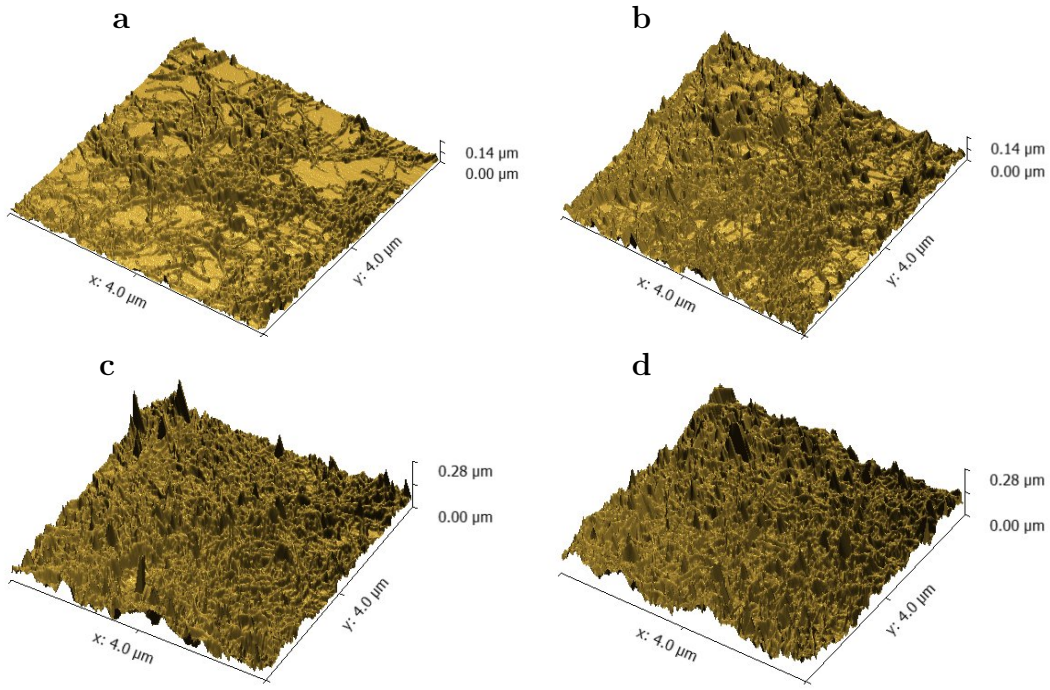


Figure 5.12: The AFM 3D images of MWCNT:SDS films spray coated on treated-COP foil in different layers, (a) 20 layers, (b) 40 layers, (c) 60 layers, and (d) 80 layers.

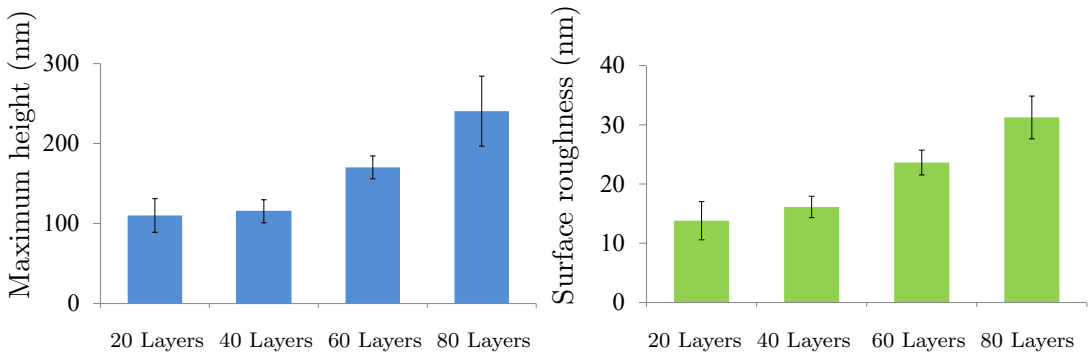


Figure 5.13: The surface roughness and the average maximum height of roughness profiles of MWCNT:SDS films.

### 5.4.2 Scanning Electron Microscopy

The SEM images of spray coated MWCNT and SWCNT films with different layers on treated-COP foil are presented in Figures 5.14, 5.15, and 5.16. In MWCNT:SDS samples, the substrates were not fully covered by 20 and 40 layers of CNTs, whereas they were mostly covered after spray coating of 60 layers (Figure 5.14). In SWCNT:SDS films, CNTs agglomerated and formed large network of bundles over the treated-COP substrate. The CNT layers did not cover the substrates uniformly even after spray coating of 80 layers (Figure 5.15). Tenent et al. [2009] have also shown that the sprayed SWCNTs formed agglomeration on glass substrate when the SDS dispersant was used. In SWCNT:CMC, the CNTs already formed uniform and homogeneous layers on the substrate after spray coating of 10 layers. The SWCNT:CMC covered the substrates uniformly and homogeneously for all layer numbers (Figure 5.16).

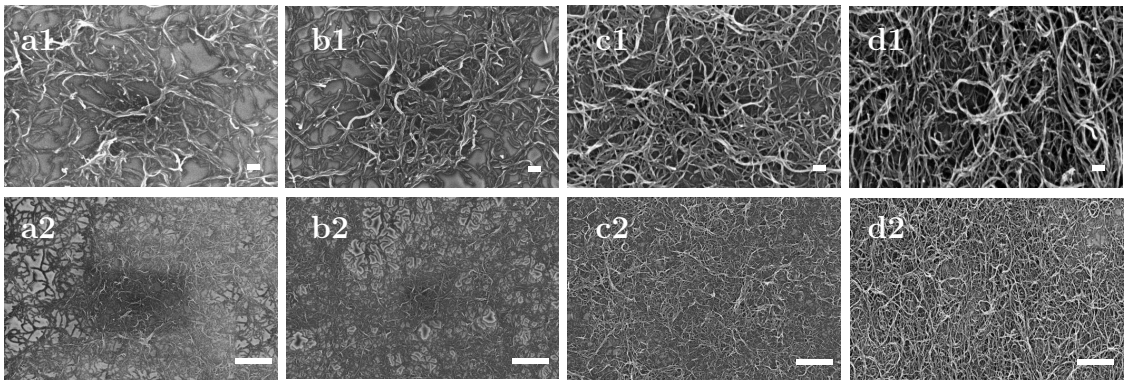


Figure 5.14: The SEM images of MWCNT:SDS films with different layers spray coated on treated-COP foil. Each column has a different number of CNT layers: (column a) 20 layers, (column b) 40 layers, (column c) 60 layers, and (column d) 80 layers. The scale bars are 100 nm in the first row and 1 $\mu$m in the second row. (a2, b2, c2, d2) adapted from (Teymouri et al. [2019]) with permission, ©2019 The Materials Research Society.

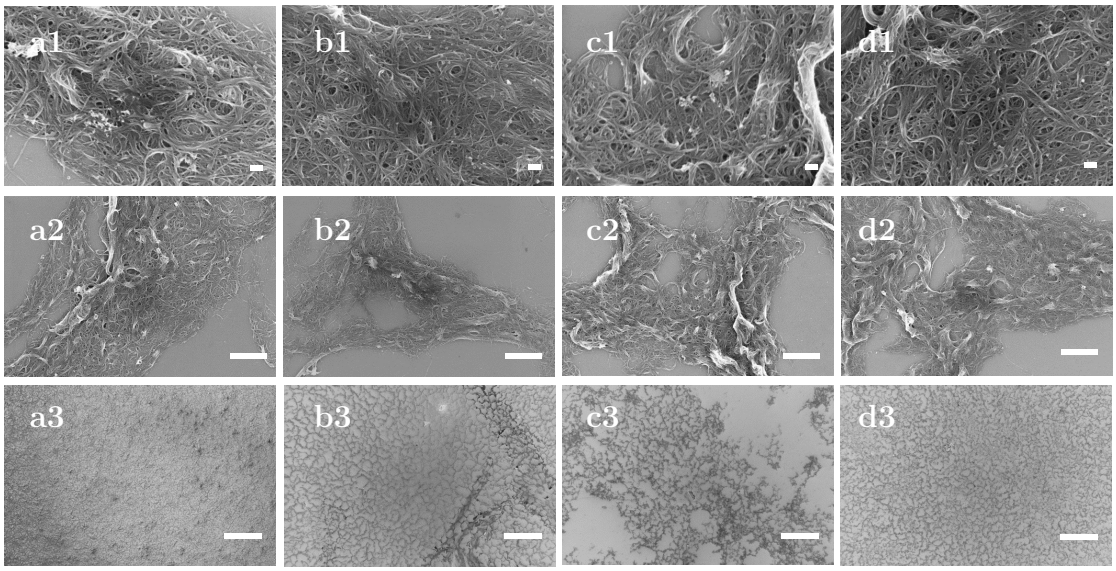


Figure 5.15: The SEM images of SWCNT:SDS films with different layers spray coated on treated-COP foil. Each column has a different number of CNT layers: (column a) 20 layers, (column b) 40 layers, (column c) 60 layers, and (column d) 80 layers. The scale bars are 100 nm in the first row and 1 $\mu$m in the second row, and 100 $\mu$m in the third row. (a2, b2, c2, d2) adapted from (Teymouri et al. [2019]) with permission, ©2019 The Materials Research Society.

It is reported in the literature that CMC is an excellent dispersant to homogeneously disperse SWCNTs in water (Takahashi et al. [2004] and Loghin et al. [2016]) and to deposit the SWCNT layers with high uniformity (Tenent et al. [2009]). The residue CMC can decrease the conductivity of CNT layers. The IR spectra of SWCNT:CMC spray coated on a silicon wafer have shown that the CMC is not completely removed from CNT layers after 4 M $HNO_3$ treatment (Tenent et al. [2009]). They have shown that the 16 M nitric acid could remove the remaining CMC polymers. Takahashi et al. [2011] has suggested that a vacuum heat treatment of SWCNTs (at 200 °C for 1 h) could remove the residual dispersant. In the present study, the higher concentrated acid and temperatures

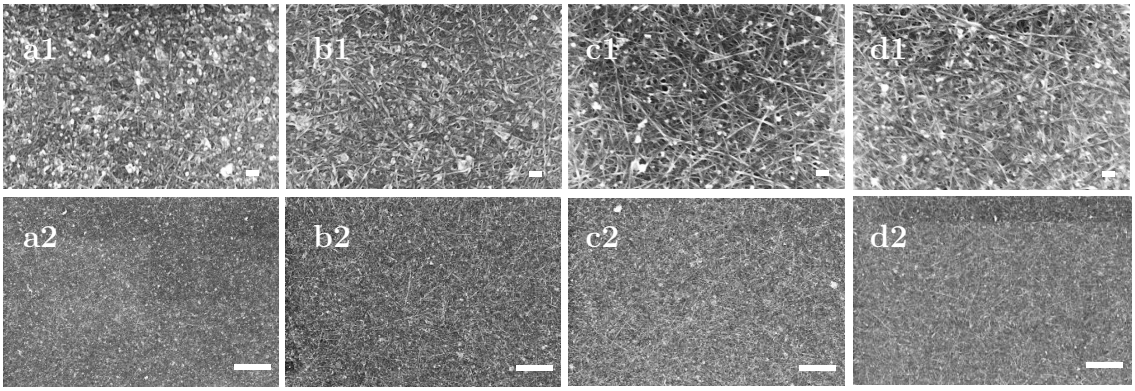


Figure 5.16: The SEM images of SWCNT:CMC films with different layers spray coated on treated-COP foil. Each column has a different number of CNT layers: (column a) 10 layers, (column b) 20 layers, (column c) 30 layers, and (column d) 40 layers. The scale bars are 100 nm in the first row and 1 $\mu$m in the second row. (a2, b2, c2, d2) adapted from (Teymouri et al. [2019]) with permission, ©2019 The Materials Research Society.

above 100 °C could damage and deform the COP substrate. Therefore, the CNT layers were heat treated at 90 °C for 2 hours, which significantly removed weakly adsorbed dispersant. In a study done by Loghin et al. [2016], heat treatment effectively removed $HNO_3$ residues on CNTs, approved by Raman spectroscopy.

### 5.4.3 Profilometry of CNT Films

The surface topography of SWCNT:SDS films spray coated on treated-COP foil was examined by a profilometer. The parameters such as surface roughness, maximum height of the roughness profile, skewness, and kurtosis were measured on different spots of three parallel samples and represented as an average value in Figure 5.17. The average maximum height of SWCNT:SDS layers increased from 105 nm for 20 layers to 326 nm for 80 layers. The surface roughness also increased from 16 nm for 20 layers to the maximum value of 60 nm for 80 layers.

The skewness and kurtosis values for all layers were above 0 and 3, respectively.

The profilometry studies showed that the formation of bundles increased the surface roughness and the average maximum height of SWCNT:SDS compared to the MWCNT:SDS layers. It was also reported by Abdelhalim et al. [2013] that the presence of CNT bundles increase the surface roughness of CNT layers. The average maximum height of SWCNT:SDS was up to 326 nm for 80 layers which was higher than the average maximum height of MWCNT:SDS 80 layers (240 nm). The kurtosis and skewness of SWCNT:SDS layers also indicated the formation of bundles over the treated-COP substrate. The 20 layers had the highest number of kurtosis (5.8) compared to the other layers, while the kurtosis values were above 3 for all layers.

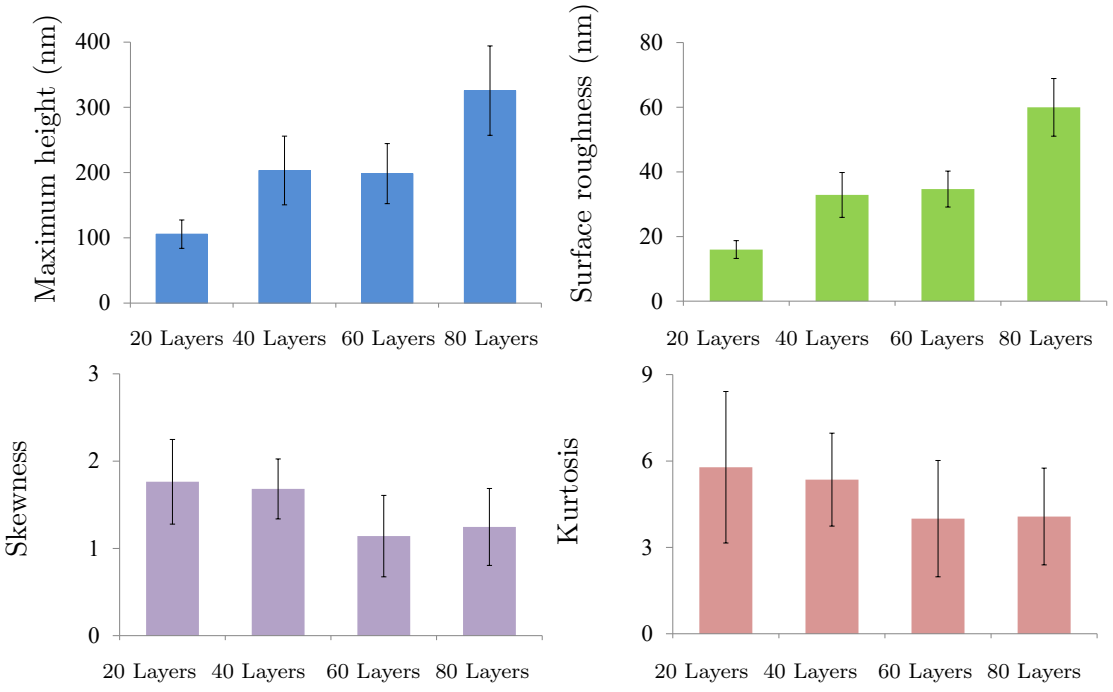


Figure 5.17: The surface roughness, average maximum height of the roughness profile, skewness, and kurtosis of SWCNT:SDS films. (n=15)

## 5.5 Interaction of Dispersant with SWCNTs

The CNTs have hydrophobic surfaces and they strongly stick together in water due to the van der Waals forces between them (Zhang et al. [2009], Vaisman et al. [2006] and Zhou and Azumi [2016]). In the literature, the type of the interaction of dispersants with CNTs is considered as a factor which can affect the homogeneous dispersion of CNTs in water (Vaisman et al. [2006]). The surface charge of SWCNTs plays an important role in the interaction mechanism of SWCNTs with dispersants (Vaisman et al. [2006]). The SWCNT that were used in this study contained 1.0-3.0 atomic% carboxylic acid according to the manufacturer. Therefore, the surface of SWCNTs was slightly coated with carboxyl groups.

The interactions between dispersant and water, and between dispersant and CNTs all affect the dispersion of CNTs (Abdelhalim et al. [2013]). CMC is a water soluble polyanion due the presence of carboxymethyl groups (–$OCH_2COO$–$Na^+$) in the chemical structure (Abdel-Galil et al. [2014] and Chakraborty et al. [2006]). There are several hydroxyl groups ($OH^-$) in cellulose which enable the hydrogen bonding between the oxygen atom of this group and the hydrogen atom of carboxyl groups on CNTs. Considering the fact that CMC is hydrophilic, it can dissolve well in water and nicely bridge the adjacent CNTs. In comparison, the SDS is an anionic dispersant which has a negative charge on its hydrophilic end (Kong et al. [2001]). The SDS can form micelles in the solution and adsorb on the surface of CNTs. The adsorption is based on the hydrophobic interaction between the hydrophobic tail of SDS with CNTs (Vaisman et al. [2006] and Vo et al. [2016]). The hydrophilic part of SDS interact with water and pull CNTs into water. SDS can form micelles in water and does not separate the CNT bundles well.

Shi et al. [2013] have shown that several parameters can affect the dispersion of SWCNTs in SDS solution such as the concentration of SDS solution, concentration of SWCNTs in SDS solution, the time and temperature of sonication. The concentration of SDS is one of the important properties that must be considered not to be higher than the critical micelle concentration (c.m.c), where the micelles are formed (Vo et al. [2016]). Sakhawat Shah and Muhahammad Khan [2008] have shown that the c.m.c of SDS in water is $8\times10^{-3}$ mol/l at 25 °C and atmospheric pressure. In this study the SDS concentration ($35\times10^{-3}$ mol/l) was higher than the concentration suggested by Sakhawat Shah and Muhahammad Khan [2008]. Also the concentration of SWCNTs in SDS solution (0.3 mg/ml) were close to the optimized values suggested in Shi et al. [2013]. Besides, the sonication was performed in an ice water bath to prevent the temperature increase of the SWCNT:SDS solution. However, after 30 min sonication the suspension beaker was warm in hand due to the energy of sonication. Shi et al. [2013] have shown that at high temperature (more than 30 °C) the SWCNTs formed bundles in SDS solution.

Tenent et al. [2009] have also suggested that the high temperature of the substrate (80 °C) led to the phase separation of the SWCNT:SDS dispersion and forms CNT agglomeration on glass substrates. Abdelhalim et al. [2013] declared that the low deposition rate is required in spray coating of CNT suspension with SDS dispersant onto the substrates. They set the temperature of substrate to 60 °C during spray coating of CNTs with atomizing gas pressure of less than 0.5 bar. They showed in AFM images that CNTs form bundles over the glass substrate. In this study, the substrate temperature was 63 °C to increase the evaporation of water during the spray coating of SWCNT:SDS suspension. However, the presence of bundles are still noticeable.

For CMC dispersant, the sonication time was decreased to 15 min in this study. The sonication could debundle the CNTs, and with longer time of sonication the length of CNTs is reduced and the percolation threshold is increased (Tenent et al. [2009]). Tenent et al. [2009] have shown that the lower sonication time of SWCNTs in CMC solution decreased the resistivity and increased the transparency of deposited CNT layers. The CMC dispersed SWCNTs better in water compared to the SDS and this created more uniform CNT layers on a treated-COP substrate after spray coating. Falco et al. [2014] also suggested that the SDS is a weak dispersant to avoid the formation of bundles and to create homogeneous layer of SWCNT over the substrate.

## 5.6 Cell Growth on SWCNT:SDS Films

The L929 cells were cultured on 8W10E electrode arrays of SWCNT:SDS 60 and 80 layers pre-coated with fibronectin for four days. The surfaces of CNTs were opened in the working electrodes areas by photolithography. The L929 cells grew with fibroblast-like morphologies on SWCNT:SDS layers as well as the SU8-2 photoresist. However, some dark spots were visible on the phase contrast images of cells shown in Figure 5.18 a. In phase contrast images with the focus of the microscope set on the CNT layers, it was observed that the black spots originate from the CNT layers (Figure 5.18 b). The dark spots in the phase contrast images of SWCNT:SDS 80 layers were more prominently apparent than in phase contrast of SWCNT:SDS 60 layers (Figure 5.19).

The L929 cells were seeded on a fibronectin pre-coated 8W10E electrode arrays of SWCNT:SDS 80 layers and they were immunostained with DAPI and phalloidin after one day of culturing. To compare the fluorescence images of

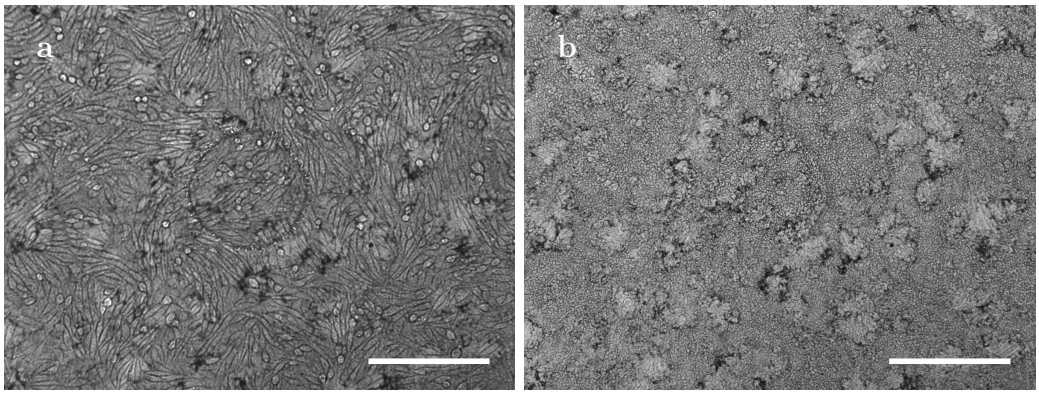


Figure 5.18: (a) Phase contrast image of L929 cells on electrode array of SWCNT:SDS (80 layers). (b) The surface of SWCNT:SDS film which shows the same area in part a with the camera focus on the CNT surface. The scale bars are 250 $\mu$m. Figure adapted from (Teymouri et al. [2019]) with permission, ©2019 The Materials Research Society.

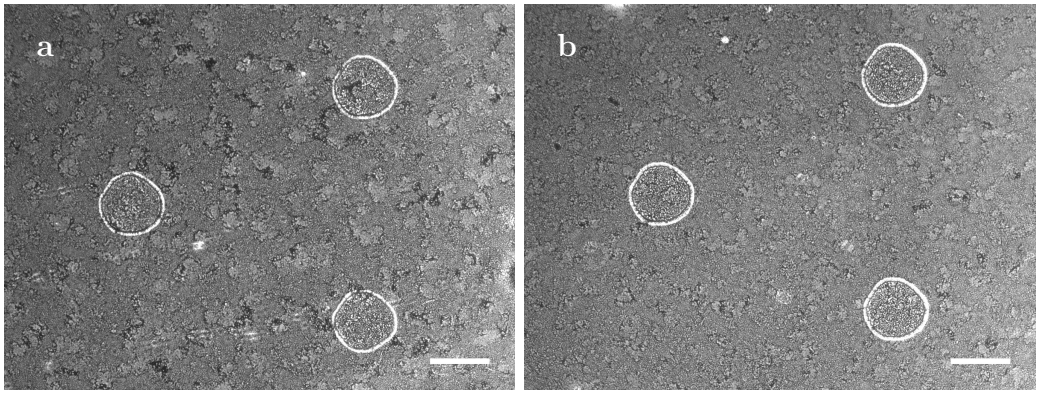


Figure 5.19: Phase contrast images of 8W10E electrode arrays of (a) SWCNT:SDS 80 layers and (b) SWCNT:SDS 60 layers. The scale bars are 250 $\mu$m.

cells grown on treated-COP and the SWCNT:SDS (80 layers) surfaces, the fluorescence images were recorded at the border region of these two areas. The fluorescence signals from nuclei and actin filaments were observed in cells grown on SWCNT:SDS surface as well as the treated-COP area (Figure 5.20 a and b). However, some irregular lines were formed in nuclei and cytoplasm of cells grown on SWCNT:SDS surface. These lines did not appear in fluorescence images of cells grown on treated-COP (Figure 5.20 c and d). The dark spots and irregular lines in microscopic images are very likely the effect of SWCNT bundles deposited on treated-COP substrate.

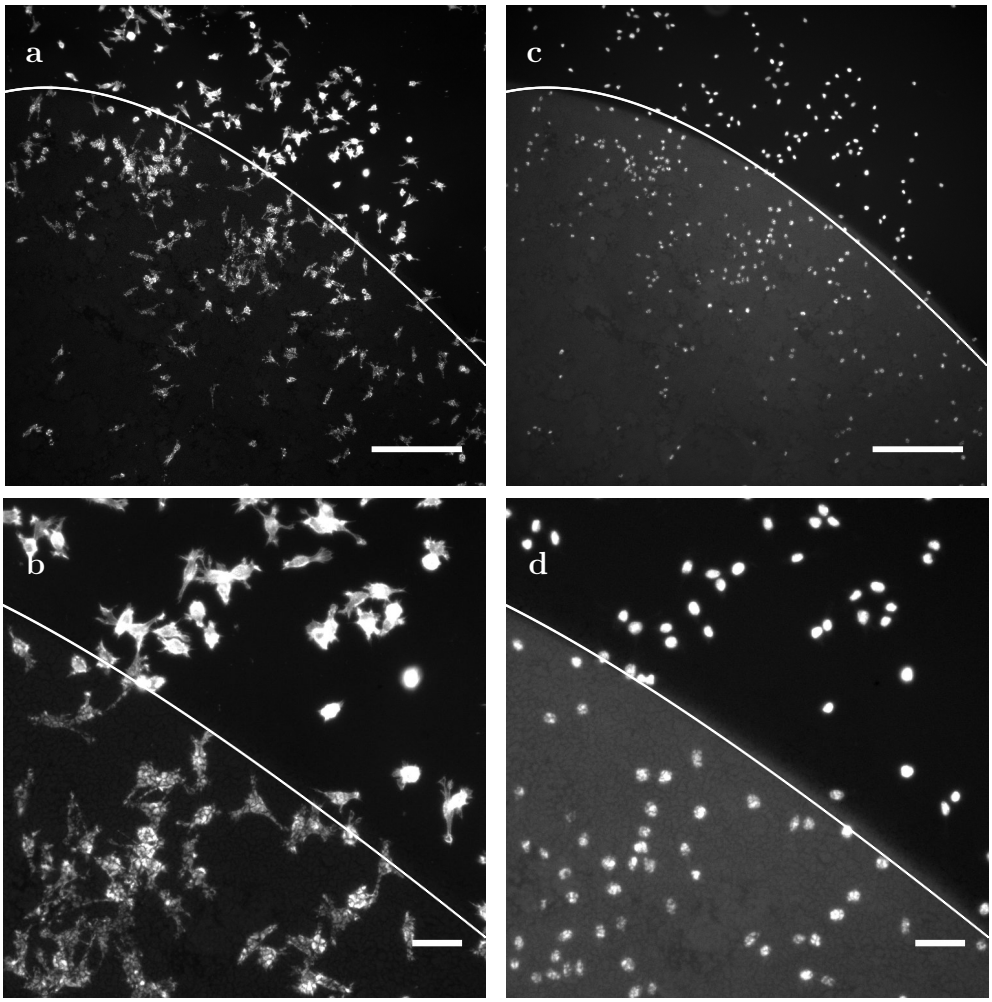


Figure 5.20: The fluorescence images of L929 cells cultured on SWCNT:SDS (80 layers) and treated-COP surfaces, both coated with SU8-2 photoresist. The white line on the images is the border line between the CNT and COP regions. (a) actin filaments of cells are stained with phalloidin. (c) the nuclear DNA of cells are labeled with DAPI. (b) and (d) are selected magnified areas from a and c, respectively. The scale bars for a and b are 250 $\mu$m , and for c and d are 50 $\mu$m. (a,b) adapted with changes from (Teymouri et al. [2019]) with permission, ©2019 The Materials Research Society.

## 5.7 Cell Growth on SWCNT:CMC Films

MCF7 cells were cultured on a 8W1E electrode array of SWCNT:CMC 20 layers pre-coated with collagen IV. On 8W1E SWCNT:CMC (20 layers), cells grew with epithelial-like morphology in a confluent layer. Also the dark shadows that were observed on SWCNT:SDS film did not appear in phase contrast images of SWCNT:CMC electrodes (Figure 5.21 a). The 8W1E gold electrode was used as control. On gold electrodes, the MCF7 cells formed a confluent layer as well; however the morphology of cells was not clearly visible in phase contrast images (Figure 5.21 b). Due to low transparancy of gold, most of the transmitted light was absorbed and therefore higher intensities of the light source were required.

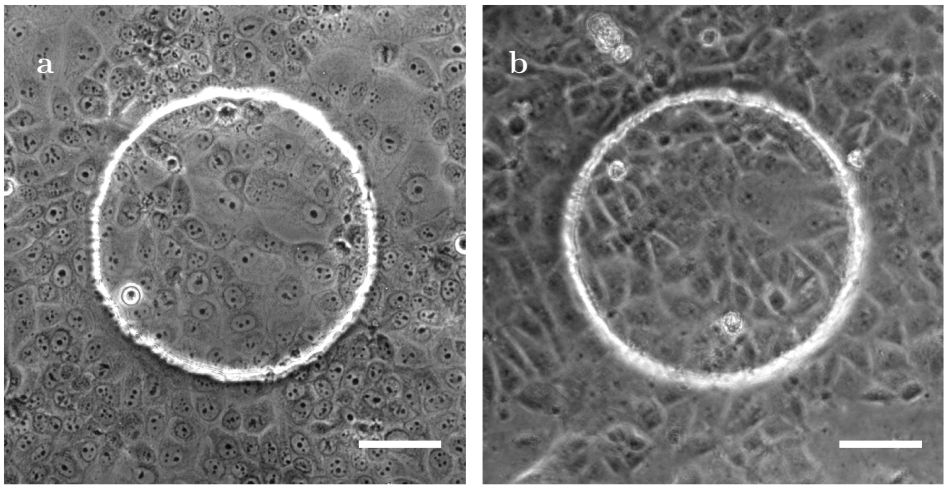


Figure 5.21: Phase contrast image of MCF7 cells grown on (a) 8W1E electrode array of SWCNT:CMC 20 layers, and (b) 8W1E ECIS® cultureware. The scale bars are 75 $\mu$m.

The MCF7 cells cultured on SWCNT:CMC (20 layers) and the gold electrodes were immunostained to observe the nuclei and microtubules of the cells. The live dead assay was also performed on SWCNT:CMC electrodes to observe the viabil-

ity of MCF7 cells grown on these electrodes. The MCF7 cells formed a confluent layer with epithelial-like morphology on SWCNT:CMC surface. In figure 5.22 a the viable cells are shown in green color and the dead cells in red color. More than 99 % of cells were viable grown on SWCNT:CMC and SU8-2 surfaces. The microtubules were stained with red fluorophores shown in red color and the nuclei were stained with DAPI shown in blue color (Figure 5.22 b). On the other hand, on gold electrodes the fluorescence images of both assays were blurred and the fluorescence signals were weak (Figure 5.22 c).

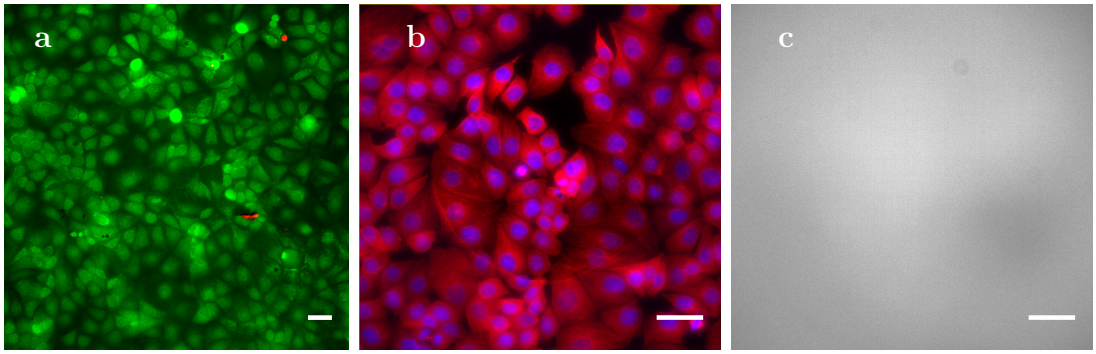


Figure 5.22: (a) The fluorescence image of MCF7 cells grown on a 8W1E electrode array of SWCNT:CMC (20 layers), in which the live cells are shown in green color and the dead cells are in red color. (b) The fluorescence image of MCF7 cells grown on 8W1E electrode array of SWCNT:CMC (20 layers), in which the microtubules and the nuclei are shown in red and blue, respectively. (c) The fluorescence image of MCF7 cells grown on 8W1E electrode array of ECIS® cultureware, in which fluorescence signals are blurred. The scale bars are 50 $\mu$m. (a) and (c) adapted from (Teymouri et al. [2019]) with permission, ©2019 The Materials Research Society.

MCF7 cells were cultured on a 8W10E electrode array of SWCNT:CMC (20 layers) without pre-coating of substrate. It was observed that MCF7 cells can grow on non-coated SWCNT:CMC layers as well as on the SU8-2 layer (Figure 5.23 a). However, the rate of cell proliferation on a fibronectin coated substrate was higher than on the non-coated substrate, as higher number of cells grew on fibronectin coated substrate after one day (Figure 5.23 b). Also 95 % of cells grown on non-coated CNT electrodes and photoresist layer were detached after three times washing the cells with PBS (Figure 5.23 c). The remaining 5 % of attached cells were still attached to the CNT surfaces at two working electrodes (Figure 5.23 d). The detached sheet of cells from the SU8-2 area partly removed the layer of cells from the CNT surface (Figure 5.23 e). The MCF7 cells on the pre-coated substrate did not detach in washing steps, as the fibronectin promoted the adhesion between the cells and the substrate. It has been also demonstrated by Imaninezhad et al. [2018] that the early attachment and spreading of cells is promoted when the surface of CNT is coated with ECM proteins.

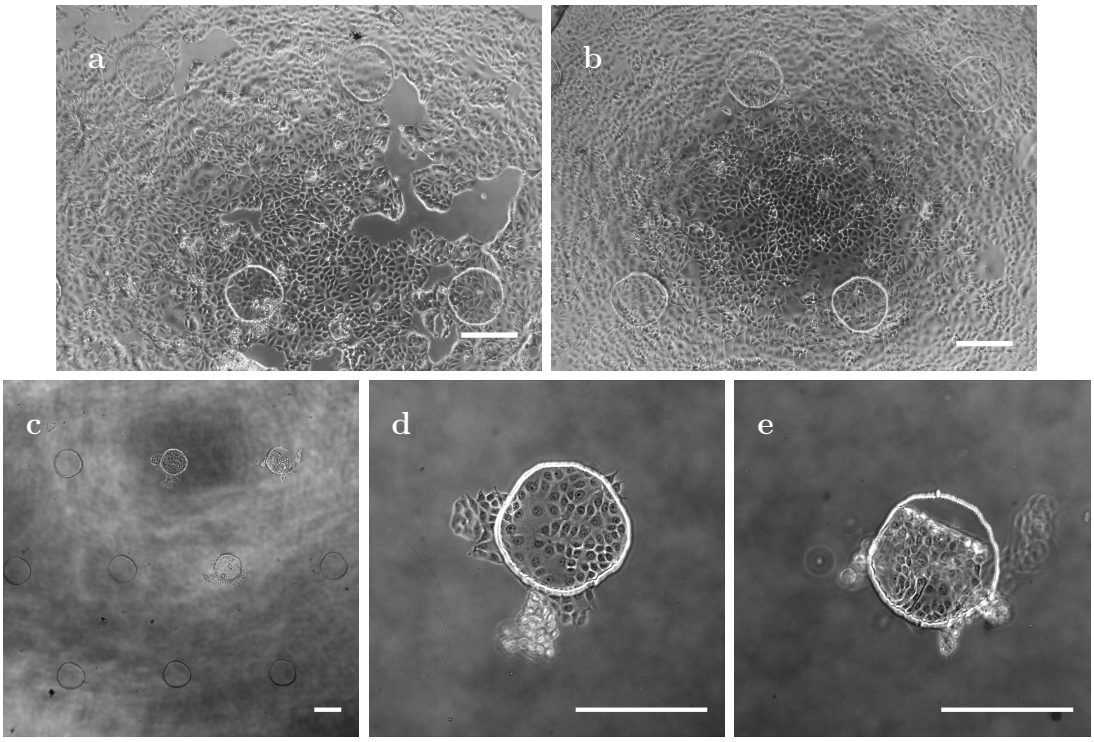


Figure 5.23: Phase contrast images of MCF7 cells grown on 8W10E electrode array of (a) non-coated SWCNT:CMC (20 layers), (b) fibronectin pre-coated SWCNT:CMC (20 layers). (c) The cells shown in part A were washed three times with PBS and most of the cells were detached from the surface, (d and e) except in a couple of working electrodes. All the scale bars are 250 $\mu$m. (a) and (c) adapted from (Teymouri et al. [2019]) with permission, ©2019 The Materials Research Society.

## 5.8 Impedimetric Measurement of Cell Growth

The MCF7 cells were cultured on the CNT electrode arrays and their electrical impedance were measured, while some of the measurements were conducted simultaneously with optical microscopy of cells. The ECIS® cultureware 8W1E was the control electrode array. In the following subsections, the main results achieved from these electrode arrays are presented and discussed.

### 5.8.1 SWCNT:CMC Electrode Arrays

The 8W1E electrode array was made of SWCNT:CMC (20 layers) working electrodes, gold counter electrodes and gold wires. The MCF7 cells were cultured with an initial concentration of $15\times10^4$ cells per well. The wells were pre-coated with collagen IV. The wells without cells were the control. The impedimetric measurements were conducted over 19 hours. The same experiment was conducted on ECIS® cultureware 8W1E as a control electrode array. After cell seeding, cells adhered to the bottom of wells, and proliferated in the whole area of well and on the working electrode. As a result, the impedance in all wells increased over time due to the cell coverage on working electrodes, while the control wells had a constant behavior (Figure 5.24). The impedances increased until the surface of the working electrodes were fully covered with cells, and reached the maximum values of around 37 kΩ and 40 kΩ for SWCNT and gold electrodes, respectively.

Figure 5.25 a, b and c show the measured impedance, capacitance and resistance at 19th hour as a function of frequency for gold and SWCNT electrodes. It is clearly indicated that the impedance is frequency dependent and the most sensitive frequency for each electrode is different. Also the impedance of cell-covered electrodes were higher than the impedance of cell-free electrodes over the range

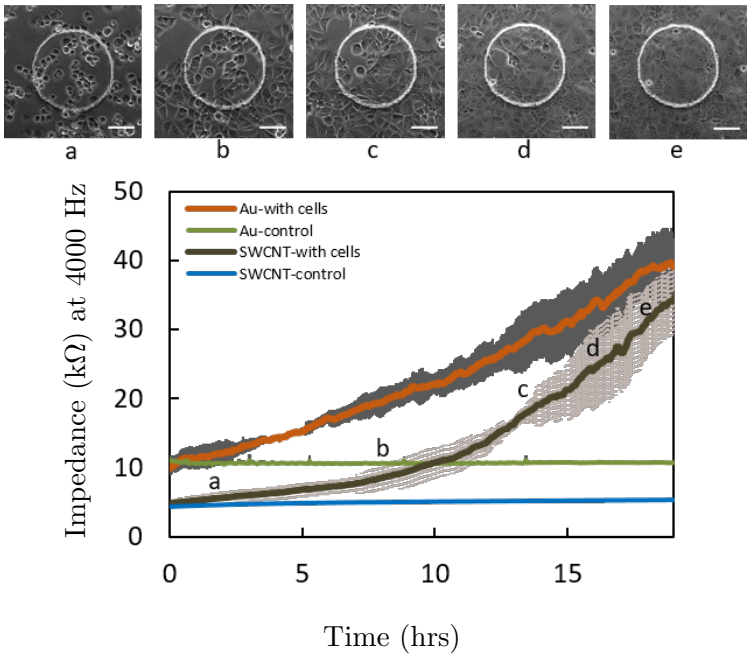


Figure 5.24: The impedance of MCF7 cells grown on gold and SWCNT:CMC 8W1E electrode arrays (n=4). The control wells were free of cells (n=4). For the SWCNT electrode the relevant phase contrast cell images are shown on top of the graph. The scale bars are 80 $\mu$m. Graph adapted with changes from (Teymouri et al. [2019]) with permission, ©2019 The Materials Research Society.

of frequencies. At low frequencies (<62.5 Hz) the impedance of both electrodes were dominated by the high resistance of electrode at the electrode-cell culture medium interface, which was observed before for gold electrode by Wegener et al. [2000]. The capacitance part of impedance were more dominated at higher frequencies and the resistances were more dominated at lower frequencies for both electrodes. In the high frequency end, the constriction resistance dominates and the impedance tends to flatten out and becomes frequency-independent (Stolwijk et al. [2015]). The most sensitive frequency for impedance, capacitance, and resistance at 19th hour was calculated using the formula (5.2):

$$|Z|norm \quad = \quad |Z|c/|Z|fc \tag{5.2}$$

$|Z|_{\mathrm{c}}$ and $|Z|_{\mathrm{fc}}$ are the impedance magnitudes of fully cell covered electrodes and the impedance of control electrodes without cells. The gold and SWCNT electrode showed different range of frequencies for recording the impedances with highest sensitivity (Figure 5.25 d). The most sensitive frequencies for capacitance were in the range of 4-16 kHz and 16-32 kHz for SWCNT and gold electrodes, respectively (Figures 5.25 e). Also the most sensitive frequencies for resistance were in the range of 0.5-2 kHz and 1-4 kHz for SWCNT and gold electrodes, respectively (Figures 5.25 f). Compared to gold electrodes, SWCNT electrodes showed higher normalized impedance magnitude in capacitance, while gold electrodes showed higher sensitivity in resistance compared to SWCNT electrodes. In fact, the larger specific surface area (Aval et al. [2018]) of SWCNTs compared to gold electrode could be the main reason for higher sensitivity of SWCNTs in capacitance recordings.

In another experiment, MCF7 cells were cultured with an initial cell concentration of $2\times10^4$ cells/well in collagen coated wells for 60 hours and simultaneously the resistances were measured (Figure 5.26). In wells with cells, the resistances progressively increased during the first 40 hours, as the cells were growing on the working electrodes. When the surfaces of the working electrodes were fully covered with cells (almost after 45 hours) the resistances reached a plateau. There were fluctuations in resistances due to the micromotion of cells on the electrodes, which has been previously observed for gold electrodes (Keese et al. [2004]). As it is expected the initial cell concentration has influence on the time of reaching

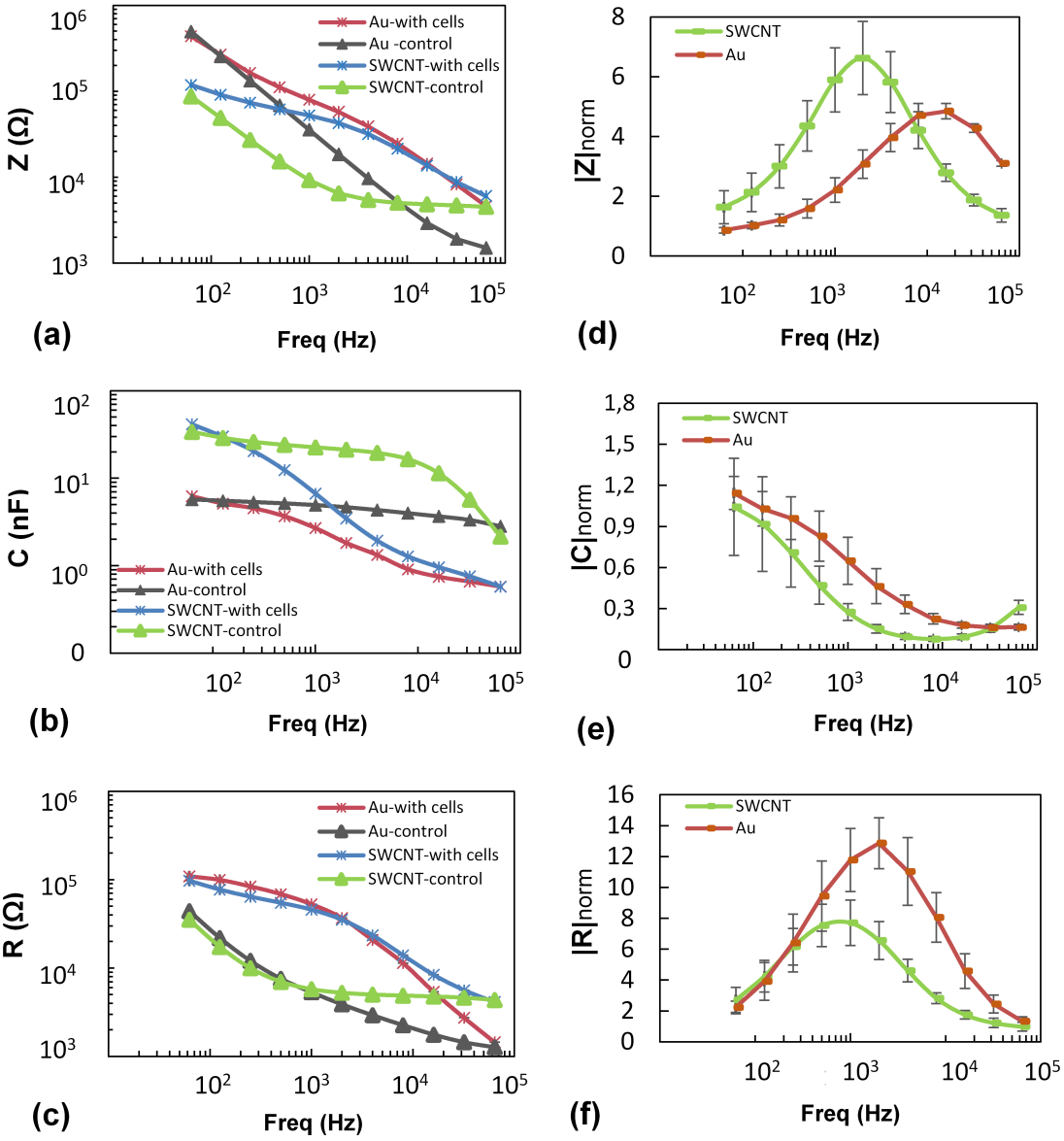


Figure 5.25: (a) The impedance spectra, (b) the capacitance spectra, and (c) the resistance spectra of MCF7 cells grown on gold and SWCNT CMC-based electrodes as a function of frequency. The parameters are measured 19 hours after cell seeding for cell-free electrodes and cell-covered electrodes. The normalized (d) impedance, (e) capacitance and (f) resistance of gold and SWCNT electrodes measured 19 h after cell seeding. (Cell-covered electrodes (n=4), cell-free electrodes (n=4)). Figure adapted from (Teymouri et al. [2019]) with permission, ©2019 The Materials Research Society.

the full cell coverage on the electrode. It was observed that the surface of the SWCNT:CMC working electrodes with initial concentration of $15\times10^4$ cells/well reach the cell full coverage during the first 19 hours. While on the SWCNT:CMC working electrodes with lower initial cell concentration ($2\times10^4$) the full cell coverage was achieved 45 hours after cell seeding. This was not only optically observed but also electrically measured by CNT electrodes.

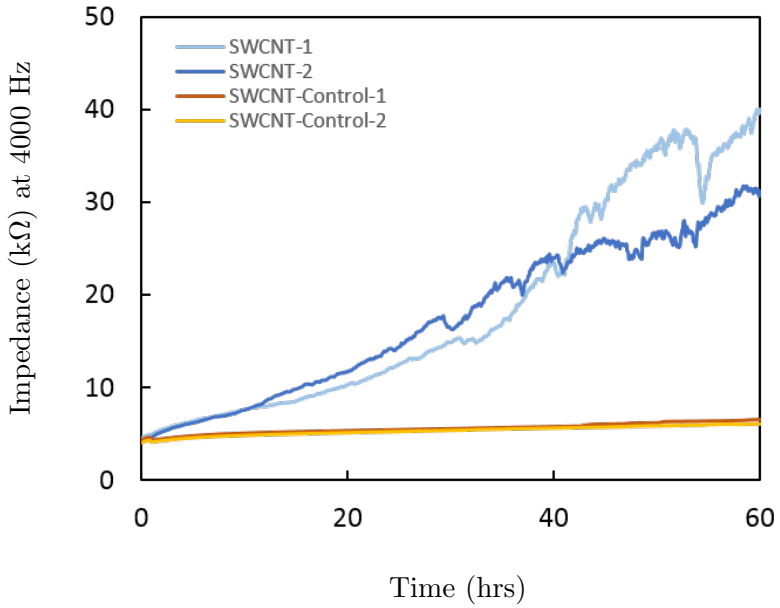


Figure 5.26: The impedance spectra of MCF7 cells grown on SWCNT:CMC electrode as a function of time.

### 5.8.2 Wounding Assay

A wounding assay was performed by SWCNT:CMC electrodes to check the feasibilty of performance of such assays by these electrodes (Figure 5.27 a). To apply the wounding current, the whole surface of electrode must be fully covered with cells. This avoids the transfer of current through the empty areas on the electrode surface but through the cell layer, which led to the cell death. Therefore, MCF7 cells were grown on 8W1E electrode arrays made of SWCNT:CMC (20 layers) as well as gold materials with high initial cell concentration of $15\times10^4$ cells/well (Figure 5.27 b1), to achieve a full covered electrode within a day. The impedance elements of capacitance and resistance both changed over time due to the cell proliferation on electrodes. The resistance on both electrodes increased to the maximum change of 18.6 kΩ and 17.5 kΩ for gold and SWCNT electrodes, respectively. The capacitance also decreased to the maximum change of -4.3 nF and -12.6 nF for gold and SWCNT electrodes, respectively. The reasons behind the changes of capacitance and resistance due to the cell growth on electrodes are throughly explained in introduction (chapter 3 - subsection of 3.2.1 Theory of ECIS).

The cell culture medium in the wells was refreshed 30 min before applying the wounding current to provide enough nutrients for the cells after wounding. Afterwards, the wounding current of 1.4 mA was applied to the electrodes for 40 seconds at around 20th hour, when the surface of electrodes were fully covered by cells (Figure 5.27 b2, b3). Upon wounding, the high current perforated the cell membranes and cells lost their integrity (Figure 5.27 b4). In other words, the high current killed the cells grown on top of the working electrode. In ECIS experiment usually the default wounding time is initially applied and after that the

wounding time is increased gradually. This method is used to find the optimum time for killing all the cells on the electrode and to prevent electrode damage. On gold electrode, we observed that $2\times20$ s wounding time was sufficient to measure that all MCF7 cells on the gold electrode were dead as the resistance decreased to values close to the control well. Therefore, for this experiment the wounding current was applied in one step of 40 s. As a result of the wounding, the resistance sharply decreased to values close to the initial value, and the capacitance sharply increased to values close to initial values as well. The cell membranes were ruptured and cells lost their integrity and decreased in size. The presence of dead cells on top of the wounded electrodes and the contents of cells in the cell culture medium caused a slight difference between final values after wounding and the initial values after cell seeding for both capacitance and resistance. After wounding, cells around the working electrode started to repopulate the working electrode (Figure 5.27 b5, b6) and they fully covered the electrode at around 30th hour. Therefore, resistance values increased again until they reached the maximum values of fully covered electrodes and the capacitances decreased to minimum values for fully covered electrodes.

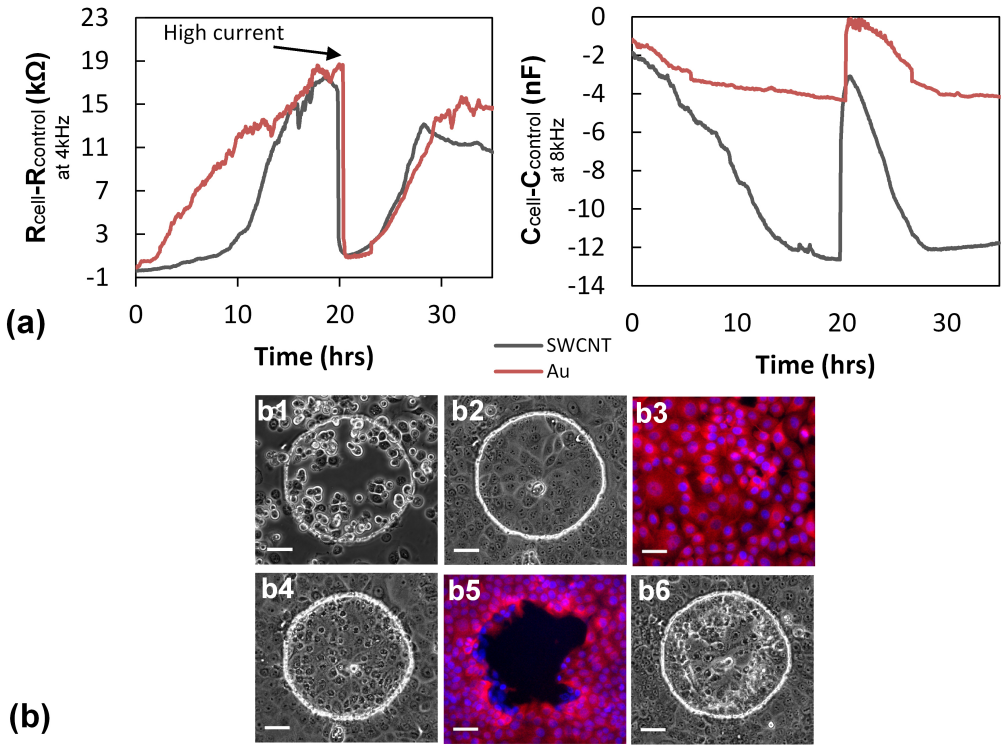


Figure 5.27: (a) The resistance and capacitance change of MCF7 cells grown on SWCNT:CMC (20 layers) and gold electrode arrays during proliferation and after applying the wounding current. (b) The relevant optical images of cells during impedimetric mesurements. Figure adapted from (Teymouri et al. [2019]) with permission, ©2019 The Materials Research Society.

# Chapter 6

# Conclusions and Outlook

In this study, one of the initial steps in electrode design was to find the most suitable photoresist for the passivation of electrode array. As the photoresists were in direct contact with the living cells, the biocompatibility of photoresist was an important criteria for the selection of the photoresist. It is reported in the literature that SU-8 has a hydrophobic surface and does not support cells in attachment and proliferation (Hamid et al. [2015] and Pai et al. [2007]). In this study, the MCF7 cells were able to grow with epithelial-like morphology on negative photoresist SU8-2. However, the fibroblast L929 cells grew with round-shaped morphology on this photoresist. The L929 cells were in round shape in the beginning of culturing and the lack of adhesion cites on the surface of the photoresist layer could prevent them from adhering and spreading for several days. The pre-coating of the surface with extracellular matrix proteins provided the interaction sites for the cells' surface receptors (Khalili and Ahmad [2015]). After fibronectin coating, the L929 cells were able to grow with normal morphology on the SU8-2 layer and the MCF7 cells did not detach from the surface of photoresist in PBS washing steps. After all, the ECIS experiments were performed with ECM protein pre-coated wells to be sure that the cells attach to both the CNT electrode

and the surrounding photoresist in a well.

The other important criteria in photoresist selection was the auto-fluorescence property of the photoresist. This property plays an important role in the quality of fluorescence microscopy images from the photoresist. In literature, it is reported that the SU-8 has a high level of auto-fluorescence during fluorescence microscopy of cells (Tamai et al. [2015]) and for biosensors that rely on fluorescence detection (Cao et al. [2012]). The SU-8 is an epoxy-based photoresist and the *pi*-electrons of the benzene rings cause this behavior. In this study we understood that the auto-fluorescence property of SU8-2 did not affect the fluorescence images of cells. Taking into account that COP foils provide high quality images in fluorescence microscopy, the photoresist SU8-2 had even lower detected fluorescence intensity compared to the treated-COP foil. The major difference between the SU8-2 applied in this study and the SU-8 photoresists that are used in the literature is the lower viscosity of SU8-2 and as a result lower thickness of the photoresist layer. Therefore, the SU8-2 was selected for the passivation of CNT electrode arrays, due to its biocompatibility and negligible auto-fluorescence property. This photoresist is suitable for fluorescence microscopy observation of cells and it didn't blur the fluorescence images. The SU8-2 is colorless and the fabricated ECIS electrode arrays were transparent. Therefore, it is a suitable photoresist for transparent electrode arrays that are applied for cell-based assays.

In this study the MWCNTs were first chosen for the fabrication of the working electrodes due to their lower cost, better availability and easier dispersability compared to the SWCNTs (Moisala et al. [2006] and Vaisman et al. [2006]). The lowest sheet resistance in MWCNT layers was 2.77 kΩ/sq (66.8 % transmittance) which was achieved by spray coating of 80 layers. However, the electrode arrays of 8W10E made of 80 layers of MWCNT working electrodes had initial impedances

around 10 kΩ in ECIS experiments. Therefore, the conductivity of electrode arrays was too low to be sensitive enough to measure the impedance changes during the evolving cell-coverage of the electrodes. Consequently, 2.77 kΩ/sq was considered as a high sheet resistance for CNT layers to be used for fabrication of an 8W1E electrode array. Although, the sheet resistances were measured in ambient air and the impedimetric measurements were performed in aqueous solution at 37 °C. Nevertheless, higher values of sheet resistance gave electrodes with lower conductivity, and lower sheet resistances result in electrode arrays with better conductivity.

The type of CNT, dispersant and the number of coated layers, all affected the sheet resistance and transparency of the final CNT multilayers. The SWCNT was the alternative electrode material and the lowest sheet resistance for SWCNT:SDS was 0.69 kΩ/sq (65.5 % transmittance) by spray coating of 80 layers. The lack of uniformity of SWCNTs on treated-COP substrate and the formation of CNT bundles were the main drawback for the SWCNTs dispersed with SDS dispersants. The CNT bundles appeared as dark spots in phase contrast images, and irregular lines in fluorescence images of cells.

The uniformity of SWCNT layers on treated-COP substrate was the main improvement for the quality of microscopic images. In this regards, the dispersant CMC was used for a homogeneous dispersion of CNTs in water. The SEM images showed the spray coated SWCNT:CMC layers were uniform even in the lowest number of CNT layers (10 layers). The hydrophilicity of dispersants and the chemical interaction of dispersants with SWCNTs played an important role in the homogeneous dispersion of SWCNTs in water and consequently in uniformity of the deposited CNT layers on the substrate. The uniformity of SWCNT:CMC layers improved the quality of microscopic images in electrode arrays compared

to the gold and SWCNT:SDS electrodes. In fluorescence microscopy images of viable MCF7 cells grown on CNT:CMC electrodes, the nuclei and microtubules were observed free of background line noises.

The sheet resistances of SWCNT:CMC layers were considerably lower than the sheet resistances of SWCNT:SDS and MWCNT:SDS layers. The sheet resistances and trasmittances were fitted to the Tinkham's formula to measure the ratio ($\gamma$) between electrical conductivity and the optical conductivity coefficient of CNT multilayers. The SWCNT:CMC had the highest $\gamma$ among the other CNTs. This indicates that at a given transmittance the SWCNT:CMC has a lower sheet resistance compared to the MWCNT:SDS and SWCNT:SDS layers. Considering the lower sheet resistances of SWCNTs with acceptable transmittances, the SWCNT:CMC layers were selected between these three groups for creating ECIS electrode arrays.

In the present study, the lowest sheet resistance among SWCNT:CMC films was achieved by spray coating of 40 layers, which had sheet resistance of 119.1 $\Omega$/sq and transmittance of 58.1 %. Although the sheet resistances of 30 and 40 layers of SWCNT:CMC were lower than for the 20 layers but their transparencies decreased to less than 66 %. The 10 layers had higher transmittance compared to 20 layers, while the sheet resistance was noticeably higher. Therefore, the best trade-off in this group was 20 layers of SWCNT:CMC with transmittance of 73 % and sheet resistance of 269.9 $\Omega$/sq. The 8W1E electrode array was fabricated with 20 layers of SWCNT:CMC working electrodes.

The surface of SWCNTs were pre-coated with ECM protein before cell culturing, as the cell layer showed more stability on electrode layer during staining process compared to non-treated electrode surface. The high binding affinity of CNTs to biological molecules (Namgung et al. [2011]) as well as large specific sur-

face area (Perepelytsina et al. [2018]) and the nanometer surface roughness (Price et al. [2004]) of CNTs provided a suitable electrode surface for attachment and growth of MCF7 cells. The SWCNT:CMC multilayers were optically smooth and highly uniform on substrate. The morphologies of cells, stained nuclei and microtubules, live and dead cells had a good visibility on SWCNT:CMC electrodes. In comparison on gold electrode, the morphology of MCF7 cells were not obvious and the fluorescence microscopy images were blurred due to the high background fluorescence. Also, the formation of CNT bundles in SWCNT:SDS multilayers limited the quality of cell microscopic images on these electrodes. Therefore, both phase contrast and fluorescence microscopy of cells on SWCNT:CMC had higher optical quality compared to the gold and SWCNT:SDS electrodes.

The electrical measurements showed that the SWCNT:CMC electrodes are very sensitive and they could even sense the micromotion of cells. The effect of initial cell concentration on cell proliferation was clearly observable on SWCNT electrodes. The wounding assay was also carried out successfully with SWCNT:CMC electrodes. SWCNT electrode represented the same behavior as the gold electrodes during wounding assay regarding the changes in resistance and capacitance. The maximum resistance changes that cells induced on fully covered electrodes were in the same range for SWCNT:CMC and gold electrodes. We combined the ECIS measurements with optical imaging of cells. The effect of cell growth on electrical changes are visibly identified. Both electrical graphs and the optical images indicated that the cells were able to repopulate the wounded electrode and the resistance increased over time. While the capacitance sharply increased by wounding current and afterwards it decreased gradually by cell repopulation on electrode. By transparent SWCNT electrodes, the microscopy of electrodes improved noticeably while the performance of the electrodes remained

comparable with gold electrodes.

With transparent electrodes we could understand the cell's behaviors on the electrode in more details during the electrical measurements. This could be specially interesting for designing CNT electrode arrays suitable for flow systems, where cells could be cultured under flow and at the same time the electrical properties are measured. With transparent electrode, the impedimetric measurements can be combined with various staining techniques without limitation in microscopy which can open a new horizon in developing better environments and conditions for cells and consequently new drugs and disease diagnosis.

# References

V. Aas, S. Torbla, M.H. Andersen, J. Jensen, and A.C. Rustan. Electrical stimulation improves insulin responses in a human skeletal muscle cell model of hyperglycemia. *Annals of the New York Academy of Sciences*, 967:506–515, 2002. 45

A. Abdel-Galil, H.E. Ali, A. Atta, and M.R. Balboul. Influence of nanostructured $TiO_2$ additives on some physical characteristics of carboxymethyl cellulose (CMC). *Radiation Research and Applied Sciences*, 7:36–43, 2014. 26, 90

A. Abdelhalim, A. Abdellah, G. Scarpa, and P. Lugli. Fabrication of carbon nanotube thin films on flexible substrates by spray deposition and transfer printing. *Carbon*, 61:72–79, 2013. 12, 14, 18, 20, 21, 22, 23, 25, 28, 29, 89, 90, 91

A. Abdellah, A. Yaqub, C. Ferrari, B. Fabel, P. Lugli, and G. Scarpa. Spray deposition of highly uniform CNT films and their application in gas sensing. *IEEE 11th International Conference on Nanotechnology*, pages 1118–1123, 2011. 12, 54

A. Abdellah, A. Abdelhalim, F. Loghin, P. Köhler, Z. Ahmad, G. Scarpa, and

P. Lugli. Flexible carbon nanotube based gas sensors fabricated by large-scale spray deposition. *IEEE Sensors*, 13:4014–4021, 2013. 11, 12, 14, 54

M. Abdolahad, M. Taghinejad, H. Taghinejad, M. Janmalekib, and S. Mohajerzadeh. A vertically aligned carbon nanotube-based impedance sensing biosensor for rapid and high sensitive detection of cancer cells. *Lab Chip*, 12: 1183–1190, 2012. 15

D. Adams, R. Korke, and W. Hu. *Application of Stoichiometric and Kinetic Analyses to Characterize Cell Growth and Product Formation*. Humana Press, 2007. 38

B. Alberts, A. Johnson, J. Lewis, M. Raff, K. Roberts, and Walter.P. *Molecular biology of the cell. 4th edition*. New York: Garland Science, 2002. 38

C.A.S. Andrade, J.M. Nascimento, I.S. Oliveira, C.V.J. de Oliveira, C.P. de Melo, O.L. Franco, and M.D.L. Oliveira. Nanostructured sensor based on carbon nanotubes and clavanin A forbacterial detection. *Colloids and Surfaces B: Biointerfaces*, 135:833–839, 2015. 16

Applied BioPhysics, Inc. `http://www.biophysics.com/`, 2021. [Online; accessed 19-June-2021]. 41, 44, 45, 48

A. Armano and S. Agnello. Two-Dimensional Carbon: A Review of Synthesis Methods, and Electronic, Optical, and Vibrational Properties of Single-Layer Graphene. *Carbon*, 5, 2019. 8, 10

L.F. Aval, M. Ghoranneviss, and Pour G.B. High-performance supercapacitors based on the carbon nanotubes, graphene and graphite nanoparticles electrodes. *Heliyon*, 4:e00862, 2018. 102

P.R. Bandaru. Electrical properties and applications of carbon nanotube structures. *Nanoscience and Nanotechnology*, 7:1–29, 2007. 8

M.N. Barshutina, V.S. Volkov, A.V. Arsenin, D.I. Yakubovsky, A.V. Melezhik, A.N. Blokhin, A.G. Tkachev, A.V. Lopachev, and V.A. Kondrashov. Biocompatible, electroconductive, and highly stretchable hybrid silicone composites based on few-layer graphene and CNTs. *Nanomaterials*, 11:1143, 2021. 30

D.J. Beesley, B.K. Price, S. Hunter, M.S.P. Shaffer, and J.C. de Mello. Direct dispersion of SWNTs in highly conductive solvent-enhanced PEDOT:PSS films. *Nanocomposites*, 2:135–140, 2016. 31

A.J. Blanch, C.E. Lenehan, and J.S. Quinton. Optimizing surfactant concentrations for dispersion of single-walled carbon nanotubes in aqueous solution. *Phys. Chem. B*, 114:9805–9811, 2010. 24, 25

P. Bondavalli, P. Legagneuxa, and D. Pribat. Carbon nanotubes based transistors as gas sensors: State of the art and critical review. *Sensors and Actuators B: Chemical*, 140:304–318, 2009. 15

M. Cain. *Discover Biology 2nd edition*. W.W. Norton and Company, Inc., 2002. 34

C. Cao, S.W. Birtwell, Høgberg J., H. Morgan, A. Wolff, and D.D. Bang. Gold nanoparticles-coated SU-8 for sensitive fluorescence-based detections of DNA. *Diagnostics*, 2:72–82, 2012. 72, 110

T. Chakraborty, I. Chakraborty, and S. Ghosh. Sodium carboxymethylcellulose-CTAB interaction: a detailed thermodynamic study of polymer-surfactant interaction with opposite charges. *Langmuir*, 22:9905–9913, 2006. 26, 90

T.T. Chastek, A. Wadajkar, K.T. Nguyen, S.D. Hudson, and T.Q. Chastek. Polyglycol-templated synthesis of poly(N-isopropyl acrylamide) microgels with improved biocompatibility. *Colloid and Polymer Science*, 288:105–114, 2010. 25

L-Y. Chen, Y-J Chen, and C-S. Chang. Electric current distribution of a multiwall carbon nanotube. *AIP Advances*, 6:075216, 2016. 12, 13

S. Chen, A.E. Goode, S. Sweeney, I.G. Theodorou, A.J. Thorley, P. Ruenraroengsak, and et al. Sulfidation of silver nanowires inside human alveolar epithelial cells: a potential detoxification mechanism. *Nanoscale*, 5:9839–9847, 2013. 30

H. Chiba, M. Osanai, M. Murata, T. Kojima, and N. Sawada. Transmembrane proteins of tight junctions. *Biochim. Biophys. Acta*, 1778:588–600, 2008. 39

D.A. Chistiakov, A.N. Orekhov, and Y.V. Bobryshev. Effects of shear stress on endothelial cells: go with the flow. *Acta Physiologica*, 219:382–408, 2017. 49

K. Cho, D-Y.and Eun, S-H. Choa, and H-K. Kim. Highly flexible and stretchable carbon nanotube network electrodes prepared by simple brush painting for cost-effective flexible organic solar cells. *Carbon*, 666:530–538, 2014. 15

A. Chortos, G.I. Koleilat, R. Pfattner, D. Kong, P. Lin, and R. Nur. Mechanically durable and highly stretchable transistors employing carbon nanotube semiconductor and electrodes. *Adv. Mater.*, 28:4441–4448, 2016. 14

P.R. Clark, R.K. Kim, J.S. Pober, and M.S. Kluger. Tumor necrosis factor disrupts claudin-5 endothelial tight junction barriers in two distinct NF-kB-dependent phases. *PLOS One*, 10:e0120075, 2015. 46

C. Colombo, M. Lupi, P. Ubezio, and D. Moscatelli. Cytotoxicity of PMMA-based nanoparticles synthesized adopting SDS and Tween 80. *Macromol. Symp.*, 324: 134–139, 2013. 26

X. Dai, W. Zhou, T. Gao, J. Liu, and C.M. Lieber. Three-dimensional mapping and regulation of action potential propagation in nanoelectronics innervated tissues. *Nat. Nanotechnol.*, 11:776–782, 2016. 76

S.K. Das, S. Sengupta, and L. Velarde. Interfacial surfactant ordering in thin films of SDS-encapsulated single-walled carbon nanotubes. *Phys. Chem. Lett.*, 7:320–326, 2016. 25

K.G. Dassios, P. Alafogianni, S.K. Antiohos, C. Leptokaridis, N-M. Barkoula, and T.E. Matikas. Optimization of sonication parameters for homogeneous surfactant-assisted dispersion of multiwalled carbon nanotubes in aqueous solutions. *Phys. Chem. C*, 119:7506–7516, 2015. 24, 29

A.P. Demchenko. *Introduction to Fluorescence Sensing.* Springer Science and Business Media, 2015. 2

S. Devaraju, T. Lee, A.K. Mohanty, Y.K. Hong, and K.H. Yoon. Fabrication of durable and flexible single-walled carbon nanotube transparent conductive films. *RSC Adv.*, 7:19267, 2017. 22, 23

N.T. Dinh, E. Sowade, T. Blaudeck, S. Hermann, R.D. Rodriguez, and et al. High-resolution inkjet printing of conductive carbon nanotube twin lines utilizing evaporation-driven self-assembly. *Carbon*, 96:382–393, 2016. 21

C. Donga, A.S. Campella, R. Eldawuda, G. Perhinschia, Y. Rojanasakulb, and

C.Z. Dinu. Effects of acid treatment on structure, properties and biocompatibility of carbon nanotubes. *Applied Surface Science*, 264:261–268, 2013. 28

F. Du, J.E. Fischer, and K.I. Winey. Effect of nanotube alignment on percolation conductivity in carbon nanotube/polymer composites. *Phys. Rev. B*, 72: 121404(R), 2005. 12

A. Dzementsei, D. Schneider, A. Janshoff, and T. Pieler. Migratory and adhesive properties of xenopus laevis primordial germ cells in vitro. *Biology Open*, 2: 1279–1287, 2013. 45

J.E. Ellis, U. Green, D.C. Sorescu, Y. Zhao, and A. Star. Mechanism of $NO_2$ detection in carbon nanotube field effect transistor chemical sensors. *Appl. Phys. Lett.*, 88:123112, 2006. 14

A. Falco, L. Cina, G. Scarpa, P. Lugli, and A. Abdellah. Fully-sprayed and flexible organic photodiodes with transparent carbon nanotube electrodes. *ACS Appl. Mater. Interfaces*, 6:10593–10601, 2014. 15, 25, 55, 79, 92

D.A. Fletcher and R.D. Mullins. Cell mechanics and the cytoskeleton. *Nature*, 463:485–492, 2010. 35

K. Foremny, W.S. Konerding, A. Behrens, P. Baumhoff, U.P. Froriep, A. Kral, and T. Doll. Carbon-nanotube-coated surface electrodes for cortical recordings in vivo. *Nanomaterials*, 11:1029, 2021. 17

R.I. Freshney. *Culture of animal cells.* John Wiley and Sons, Inc., 2005. ISBN 9780471747598. 37, 39

T. Fujigaya and N. Nakashima. Non-covalent polymer wrapping of carbon nanotubes and the role of wrapped polymers as functional dispersants. *Sci. Technol. Adv. Mater.*, 16:024802, 2015. 26, 27

S. Furukawa, M. Fujita, Y. Kanatomi, M. Minoura, M. Hatanaka, K. Morokuma, K. Ishimura, and M. Saito. Double aromaticity arising from sigma and pi rings. *Communications Chemistry*, 1, 2018. 10

E.S. Gadelmawla, M.M. Koura, T.M.A. Maksoud, I.M. Elewa, and H.H. Soliman. Roughness parameters. *Materials Processing Technology*, 123:133–145, 2002. 62

A. Ganguly, H. Yang, R. Sharma, K. D. Patel, and F. Cabral. The role of microtubules and their dynamics in cell migration. *J. Biol. Chem.*, 287:43359–43369, 2012. 35

A.K. Geim and K.S. Novoselov. The rise of graphene. *Nature Mater.*, 6:183–191, 2007. 8

V. Georgakilas, J.A. Perman, J. Tucek, and R. Zboril. Broad family of carbon nanoallotropes: classification, chemistry, and applications of fullerenes, carbon dots, nanotubes, graphene, nanodiamonds, and combined superstructures. *Chem. Rev.*, 115:4744–4822, 2015. 8

I. Giaever and C.R. Keese. Monitoring fibroblast behavior in tissue culture with an applied electric field. *PNAS*, 81:3761–3764, 1984. 1

I. Giaever and C.R. Keese. Use of electric fields to monitor the dynamical aspect of cell behavior in tissue culture. *IEEE Transactions on Biomedical Engineering*, 33:242–247, 1986. 41, 46

I. Giaever and C.R. Keese. Micromotion of mammalian cells measured electrically. *PNAS*, 88:7896–7900, 1991. 43, 45, 46

P. Gulati, P. Kaur, M.V. Rajam, T. Srivastava, P. Mishra, and S.S. Islam. Vertically aligned multi-walled carbon nanotubes based flexible immunosensor for extreme low level detection of multidrug resistant leukemia cells. *Sensors and Actuators B: Chemical*, 301:127047, 2019. 16

P. Gulati, P. Mishra, M. Khanuja, J. Narang, and S.S. Islam. Nano-moles detection of tumor specific biomarker dna for colorectal cancer detection using vertically aligned multi-wall carbon nanotubes based flexible electrodes. *Process Biochemistry*, 90:184–192, 2020. 16

N. Habibi. Preparation of biocompatible magnetite-carboxymethyl cellulose nanocomposite: Characterization of nanocomposite by FTIR, XRD, FESEM and TEM. *Spectrochimica Acta Part A: Molecular and Biomolecular Spectroscopy*, 131:55–58, 2014. 27

Q. Hamid, C. Wang, J. Snyder, and W. Sun. Surface modification of SU-8 for enhanced cell attachment and proliferation within microfluidic chips. *Biomed. Mater. Res. B: Appl. Biomater.*, 103:473–484, 2015. 109

K.N. Han, M-P.N Li, C.A. and. Bui, and G.H. Seong. Patterning of single-walled carbon nanotube films on flexible, transparent plastic substrates. *Langmuir*, 26:598–602, 2010. 18

Z. Han and A. Fina. Thermal conductivity of carbon nanotubes and their polymer nanocomposites: A review. *Progress in Polymer Science*, 36:914–944, 2011. 14

B.S. Harrison and A. Atala. Carbon nanotube applications for tissue engineering. *Biomaterials*, 28:344–353, 2007. 15

D. Hecht, L. Hu, and G. Grünera. Conductivity scaling with bundle length and diameter in single walled carbon nanotube networks. *Applied Physics Letters*, 89:133112, 2006. 12

Y. Hirai, D. Takag, S. Anai, Y. Chihara, T. Tsuchiya, K. Fujimoto, Y. Hirao, and O. Tabata. ALA-induced fluorescence detection with photoresist-based microfluidic cell sorter for bladder cancer diagnosis. *Sensors and Actuators B: Chemical*, 213:547–557, 2015. 58, 79

L. Hu, D.S. Hecht, and G. Gruner. Carbon nanotube thin films: fabrication, properties, and applications. *Chem. Rev.*, 110:5790–5844, 2010. 79

S. Iijima. Helical microtubules of graphitic carbon. *Nature*, 354:56–58, 1991. 8

S. Iijima. Structural flexibility of carbon nanotubes. *Chemical Physics*, 104:2089, 1996. 23

M. Imaninezhad, J. Schober, D. Griggs, P. Ruminski, I. Kuljanishvili, and S.P. Zustiak. Cell attachment and spreading on carbon nanotubes is facilitated by integrin binding. *Front. Bioeng. Biotechnol.*, 6:129, 2018. 98

T. Izak, O. Szabo, L. Bacakova, and A. Kromka. Diamond functional layers for cell-based impedance spectroscopy. *Procedia Engineering*, 168:614–617, 2016. 46

R. Jackson, B. Domercq, R. Jain, B. Kippelen, and S. Graham. Stability of doped transparent carbon nanotube electrodes. *Adv. Funct. Mater.*, 18:2548–2554, 2008. 79

C.B. Jacobs, M.J. Peairs, and B.J. Venton. Review: Carbon nanotube based electrochemical sensors for biomolecules. *Analytica Chimica Acta*, 662:105–127, 2010. 15

J-Y. Ji-Yong Shin, T. Premkumar, and K.E. Geckeler. Dispersion of single-walled carbon nanotubes by using surfactants: are the type and concentration important? *Chem. Eur.*, 14:6044–6048, 2008. 25

M-X. Jing, C. Han, M. Li, and X-Q. Shen. High performance of carbon nanotubes/silver nanowires-PET hybrid flexible transparent conductive films via facile pressing-transfer technique. *Nanoscale Res. Lett.*, 9:588, 2014. 29

R. Joshi, W. Mankowski, M. Winter, and et al. Automated measurement of cobblestone morphology for characterizing stem cell derived retinal pigment epithelial cell cultures. *Ocular Pharmacology and Therapeutics*, 32:331–339, 2016. 34

M. Kaempgen, G.S. Duesberg, and S. Roth. Transparent carbon nanotube coatings. *Applied Surface Science*, 252:425–429, 2005. 15

E. Katz and I. Willner. Biomolecule-functionalized carbon nanotubes: applications in nanobioelectronics. *ChemPhysChem*, 5:1084–1104, 2004. 15

P. Kaur, M-S. Shin, A. Joshi, N. Kaur, N. Sharma, J-S. Park, and S.S. Sekhon. Interactions between multiwall carbon nanotubes and poly(diallyl dimethylammonium) chloride: effect of the presence of a surfactant. *J. Phys. Chem. B*, 117:3161–3166, 2013. 25

C.R. Keese and I. Giaever. A biosensor that monitors cell morphology with

electrical fields. *IEEE Engineering in Medicine and Biology Society*, 13:402–408, 1994. 39, 43, 44, 45

C.R. Keese, J. Wegener, S.R. Walker, and I. Giaever. Electrical wound-healing assay for cells in vitro. *PNAS*, 101:1554–1559, 2004. 1, 47, 102

A.A. Khalili and M.R. Ahmad. A review of cell adhesion studies for biomedical and biological applications. *International Journal of Molecular Sciences*, 16: 18149–18184, 2015. 109

K.K. Kim, S.M. Kim, and Y.H. Lee. Chemically conjugated carbon nanotubes and graphene for carrier modulation. *Acc. Chem. Res.*, 49:390–399, 2016. 28

S. Kim, Y. Yonghyuk, X. Wang, D.D.C. Bradley, S. Lee, and J.C. deMello. Spin- and spray-deposited single-walled carbon-nanotube electrodes for organic solar cells. *Adv. Funct. Mater.*, 20:2310–2316, 2010. 20, 22

S.H. Kim, W. Song, M.W. Jung, M-A. Kang, K. Kim, S-J. Chang, S.S. Lee, J. Lim, J. Hwang, S. Myung, and K-S. An. Carbon nanotube and graphene hybrid thin film for transparent electrodes and field effect transistors. *Adv. Mater.*, 26:4247–4252, 2014. 30

T.K. Kim. T test as a parametric statistic. *Korean J Anesthesiol*, 68:540–546, 2015. 61

L. Kong, J.K. Beattie, and R.J. Hunter. Effects of nonionic surfactant and sodium dodecyl sulfate layers on electroacoustics of hexadecane/water emulsions. *Colloid and Polymer Science*, 279:678–687, 2001. 90

S. Kumar, R. Rani, N. Dilbaghi, K. Tankeshwarab, and K-H. Kim. Carbon

nanotubes: a novel material for multifaceted applications in human healthcare. *Chem. Soc. Rev.*, 46:158–196, 2017. 15, 19

O.M. Kutova, L.M. Sencha, A.D. Pospelov, O.E. Dobrynina, A.A. Brilkina, E.I. Cherkasova, and I. V. Balalaeva. Comparative analysis of cell–cell contact abundance in ovarian carcinoma cells cultured in two- and three-dimensional in vitro models. *Biology*, 9:446, 2020. 36

S-H. Lee, C-C. Teng, C-C.M. Ma, and I. Wang. Highly transparent and conductive thin films fabricated with nano-silver/double-walled carbon nanotube composites. *Colloid and Interface Science*, 364:1–9, 2011. 29

J. Li, Y. Lu, Q. Ye, M. Cinke, J. Han, and M. Meyyappan. Carbon nanotube sensors for gas and organic vapor detection. *Nano Lett.*, 3:929–933, 2003. 10

L. Li, H. Li, Y. Guo, L. Yang, and Y. Fang. Direct synthesis of graphene/carbon nanotube hybrid films from multiwalled carbon nanotubes on copper. *Carbon*, 118:675–679, 2017. 30

X. Liang. *Nanotube superfiber materials*. William Andrew Publishing, 2014. 9

M.S. Liberio, M.C. Sadowski, C. Soekmadji, R.A. Davis, and Nelson C.C. Differential effects of tissue culture coating substrates on prostate cancer cell adherence, morphology and behavior. *PLOS One*, 9:e112122, 2014. 75

License. Creative Commons Attribution 4.0 International (CC BY 4.0), 2017. 10, 27, 36

T. Lin, V. Bajpai, T. Ji, and L. Dai. Chemistry of carbon nanotubes. *Aust. J. Chem.*, 56:635–651, 2003. 24

Y. Liu, F. Zhu, W. Dan, Y. Fu, and S. Liu. Construction of carbon nanotube based nanoarchitectures for selective impedimetric detection of cancer cells in whole blood. *Analyst*, 139:5086, 2014. 16

Y. Liu, J. Zhang, Y. Cheng, and S.P. Jiang. Effect of carbon nanotubes on direct electron transfer and electrocatalytic activity of immobilized glucose oxidase. *ACS Omega*, 3:667–676, 2018. 13

C.M. Lo, C.R. Keese, and I. Giaever. Impedance analysis of mdck cells measured by electric cell-substrate impedance sensing. *Biophysical Journal*, 69:2800–2807, 1995. 43

F. Loghin, S. Colasanti, A. Weise, A. Falco, A. Abdelhalim, P. Lugli, and A. Abdellah. Scalable spray deposition process for highly uniform and reproducible CNT-TFTs. *Flexible and Printed Electronics*, 1:045002, 2016. 12, 15, 22, 54, 79, 87, 88

F. Loghin, A. Rivadeneyra, M. Becherer, P. Lugli, and M. Bobinger. A facile and efficient protocol for preparing residual-free single-walled carbon nanotube films for stable sensing applications. *Nanomaterials (Basel)*, 9:471, 2019. 14

C.G. Lopez, S.E. Rogers, R.H. Colby, P. Graham, and J.T. Cabral. Structure of sodium carboxymethyl cellulose aqueous solutions: a SANS and rheology study. *Polymer Science B: Polymer Physics*, 53:492–501, 2015. 27

S. Lu and B. Panchapakesan. Nanotube micro-optomechanical actuators. *Applied Physics Letters*, 88:253107, 2006. 19

P. Mallinjoud, J.P. Villemin, H. Mortada, M. Polay Espinoza, F.O. Desmet, S. Samaan, E. Chautard, L.C. Tranchevent, and D. Auboeuf. Endothelial,

epithelial, and fibroblast cells exhibit specific splicing programs independently of their tissue of origin. *Genome Res.*, 24:511–521, 2014. 34

B. Mandal, D. Das, S. Rameshbabu, A.P. Dhara, and S. Pal. A biodegradable, biocompatible transdermal device derived from carboxymethyl cellulose and multi-walled carbon nanotubes for sustained release of diclofenac sodium. *RSC Adv.*, 6:19605, 2016. 27

N. Minami, Y. Kim, K. Miyashita, S. Kazaoui, and B. Nalini. Cellulose derivatives as excellent dispersants for single-wall carbon nanotubes as demonstrated by absorption and photoluminescence spectroscopy. *Applied Physics Letters*, 88: 093123, 2006. 26

F. Mirri, A.W.K. Ma, T.T. Hsu, N. Behabtu, S.L. Eichmann, and et al. High-performance carbon nanotube transparent conductive films by scalable dip coating. *ACS Nano*, 6:9737–9744, 2012. 19

A. Moisala, Q. Li, I.A. Kinloch, and A.H. Windle. Thermal and electrical conductivity of single- and multi-walled carbon nanotube-epoxy composites. *Composites Science and Technology*, 66:1285–1288, 2006. 8, 110

S.M. Mousavi-Khoshdel, P. Jahanbakhsh-bonab, and E. Targholi. Structural, electronic properties, and quantum capacitance of B, N and P-doped armchair carbon nanotubes. *Physics Letters A*, 380:3378–3383, 2016. 28

S. Namgung, T. Kim, K.Y. Baik, M. Lee, J.M. Nam, and S. Hong. Fibronectin-carbon-nanotube hybrid nanostructures for controlled cell growth. *Small*, 7: 56–61, 2011. 112

NanoCap. `https://nanocap.sourceforge.net`, 2019. [Online; accessed 17-September-2019]. 9

M.P. Neupane, I.S. Park, T.S. Bae, H.K. Yi, F. Watari, and M.H. Lee. Biocompatibility of $TiO_2$ nanotubes fabricated on Ti using different surfactant additives in electrolyte. *Materials Chemistry and Physics*, 134:536–541, 2012. 25

A. Nicolas, A. Besser, and S.A. Safran. Dynamics of cellular focal adhesions on deformable substrates: consequences for cell force microscopy. *Biophys. J.*, 95: 527–539, 2008. 37

Ninithi. `https://ninithi.software.informer.com/1.0/`, 2019. [Online; accessed 17-September-2019]. 9

S.H. Oh and J.H. Lee. Hydrophilization of synthetic biodegradable polymer scaffolds for improved cell/tissue compatibility. *Biomedical Materials*, 8:014101, 2013. 75

A.J. Page, F. Ding, S. Irle, and K. Morokuma. Insights into carbon nanotube and graphene formation mechanisms from molecular simulations: a review. *Rep. Prog. Phys.*, 78:036501, 2015. 8

J. Pai, Y. Wang, G.T. Salazar, C.E. Sims, M. Bachman, G.P. Li, and N.L. Allbritton. A photoresist with low fluorescence for bioanalytical applications. *Anal. Chem.*, 79:8774–8780, 2007. 72, 109

H. Park, J-S. Kim, B.G. Choi, S.M. Jo, D.Y. Kim, W.H. Hong, and S-Y. Jang. Sonochemical hybridization of carbon nanotubes with gold nanoparticles for

the production of flexible transparent conducing films. *Carbon*, 48:1325–1330, 2010. 18, 29

S. Pei, J. Du, Y. Zeng, C. Liu, and H.M. Cheng. The fabrication of a carbon nanotube transparent conductive film by electrophoretic deposition and hot-pressing transfer. *Nanotechnology*, 20:235707, 2009. 18

O.M. Perepelytsina, A.P. Ugnivenko, A.V. Dobrydnev, O.N. Bakalinska, A.I. Marynin, and M.V. Sydorenko. Influence of carbon nanotubes and its derivatives on tumor cells in vitro and biochemical parameters, cellular blood composition in vivo. *Nanoscale Res. Lett.*, 13:286, 2018. 113

R.J. Petrie and K.M. Yamada. Fibroblasts lead the way: a unified view of three-dimensional cell motility. *Trends in Cell Biology*, 25:666–674, 2015. 34

S.H. Piao, M.H. Kim, H.J. Choi, H. Lee, and J. Park. Dispersion state and rheological characteristics of carbon nanotube suspensions. *Industrial and Engineering Chemistry*, 52:369–375, 2017. 20

G.E. Pike and C.H. Seager. Percolation and conductivity: A computer study. I. *Phys. ReV. B*, 10:1421, 1974. 11

C. Preston, Y. Xu, X. Han, J.N. Munday, and L. Hu. Optical haze of transparent and conductive silver nanowire films. *Nano Research*, 6:461–468, 2013. 30

R.L. Price, K. Ellison, K.M. Haberstroh, and T.J. Webster. Nanometer surface roughness increases select osteoblast adhesion on carbon nanofiber compacts. *J. Biomed. Mater. Res. A*, 70:129–138, 2004. 113

A.R.A. Rahman, C.M. Lo, and S. Bhansali. A detailed model for high-frequency impedance characterization of ovarian cancer epithelial cell layer using ecis

electrodes. *IEEE Transactions on Biomedical Engineering*, 56:485–492, 2009. 43

R. Reeves, A. Ribeiro, L. Lombardo, R. Boyer, and J.B. Leach. Synthesis and characterization of carboxymethylcellulose-methacrylate hydrogel cell scaffolds. *Polymers (Basel)*, 2:252–264, 2010. 27

X. Ren, K. Pei, B. Peng, Z. Zhang, Z. Wang, X. Wang, and P.K.L. Chan. A low-operating-power and flexible active-matrix organic-transistor temperature-sensor array. *Adv. Mater.*, 28:4832–4838, 2016. 14

J-M. Retrouvey, S. Schwartz, and J.K. Hartsfield. Chapter 33 - oral-facial aspects of osteogenesis imperfecta. In Jay R. Shapiro, Peter H. Byers, Francis H. Glorieux, and Paul D. Sponseller, editors, *Osteogenesis Imperfecta*, pages 313–327. Academic Press, 2014. 34

L.D. Robilliard, D.T. Kho, R.H. Johnson, A. Anchan, S.J. O'Carroll, and E.S. Graham. The importance of multifrequency impedance sensing of endothelial barrier formation using ECIS technology for the generation of a strong and durable paracellular barrier. *Biosensors (Basel)*. 43

A. Roch, T. Roch, E.R. Talens, B. Kaiser, A. Lasagni, E. Beyer, and et al. Selective laser treatment and laser patterning of metallic and semiconducting nanotubes in single walled carbon nanotube films. *Diamond and Related Materials*, 45:70–75, 2014. 18

R.S. Ruoff, D. Qian, and W.K. Liu. Mechanical properties of carbon nanotubes: theoretical predictions and experimental measurements. *C. R. Physique*, 4: 993–1008, 2003. 14

S. Sakhawat Shah and A. Muhahammad Khan. Determination of critical micelle concentration (cmc) of sodium dodecyl sulfate (SDS) and the effect of low concentration of pyrene on its cmc using ORIGIN software. *Chem. Soc. Pak.*, 30:186–191, 2008. 91

N. Saran, K. Parikh, D-S. Suh, E. Munoz, H. Kolla, and S.K. Manohar. Fabrication and characterization of thin films of single-walled carbon nanotube bundles on flexible plastic substrates. *J. Am. Chem. Soc.*, 126:4462–4463, 2004. 19

C.A. Schneider, W.S. Rasband, and K.W. Eliceiri. NIH Image to ImageJ: 25 years of image analysis. *Nature Methods*, 9:671–675, 2012. 56

S. Shama Parveen, S. Rana, R. Fangueiro, and M.C. Paiva. Characterizing dispersion and long term stability of concentrated carbon nanotube aqueous suspensions for fabricating ductile cementitious composites. *Powder Technology*, 307:1–9, 2017. 25

Y. Shi, L. Ren, D. Li, H. Gao, and B. Yang. Optimization conditions for single-walled carbon nanotubes dispersion. *Surface Engineered Materials and Advanced Technology*, 3:6–12, 2013. 90, 91

Y-D. Shi, J. Li, Y-J. Tan, Chen; Y-F., and M. Wang. Percolation behavior of electromagnetic interference shielding in polymer/multi-walled carbon nanotube nanocomposites. *Composites Science and Technology*, 170:70–76, 2019. 11

D.H. Shin, H.C. Shim, J. Song, S. Kim, and C. Han. Conductivity of films made from single-walled carbon nanotubes in terms of bundle diameter. *Scr. Mater.*, 60:607–610, 2009. 12

R. Shvartzman-Cohen, Y. Levi-Kalisman, E. Nativ-Roth, and R. Yerushalmi-Rozen. Generic approach for dispersing single-walled carbon nanotubes: the strength of a weak interaction. *Langmuir*, 20:6085–6088, 2004. 27

Sigma-Aldrich. Carbon nanotubes. `https://www.sigmaaldrich.com/materials-science/material-science-products.html?TablePage=16376687`, 2019a. [Online; accessed 05-October-2019]. 8

Sigma-Aldrich. Components of RPMI 1640 cell culture medium. `https://www.sigmaaldrich.com/content/dam/sigma-aldrich/docs/Sigma/Formulation/r8758for.pdf`, 2019b. [Online; accessed 26-September-2019]. 65

D. Simien, J.A. Fagan, W. Luo, J.F. Douglas, K. Migler, and J. Obrzut. Influence of nanotube length on the optical and conductivity properties of thin single-wall carbon nanotube networks. *ACS Nano*, 2:1879–1884, 2008. 11, 12

S. Son, J. Yun, Y. Noh, S. Lee, H. Jo, S. Na, and H. Joh. Highly flexible and bendable carbon nanosheets as transparent conducting electrodes for organic solar cells. *Carbon*, 81:546–551, 2015. 18

J.A. Stolwijk, K. Matrougui, C.W. Renken, and M. Trebak. Impedance analysis of GPCR-mediated changes in endothelial barrier function: overview, and fundamental considerations for stable and reproducible measurements. *Pflugers Arch*, 467:2193–2218, 2015. 101

M.S. Strano, V.C. Moore, M.K. Miller, M.J. Allen, E.H. Haroz, C. Kittrell, R.H. Hauge, and R.E. Smalley. The role of surfactant adsorption during ultrasonica-

tion in the dispersion of single-walled carbon nanotubes. *Nanosci. Nanotech.*, 3:81–86, 2003. 28

R. Szulcek, H.J. Bogaard, and G.P. van Nieuw Amerongen. Electric cell-substrate impedance sensing for the quantification of endothelial proliferation, barrier function, and motility. *Visualized Experiments*, 85:51300, 2014. 46, 48

T. Takahashi, K. Tsunoda, H. Yajima, and T. Ishii. Dispersion and purification of single-wall carbon nanotubes using carboxymethylcellulose. *Japanese Journal of Applied Physics*, 43:3636–3639, 2004. 87

T. Takahashi, K. Takei, A.G. Gillies, R.S. Fearing, and A. Javey. Carbon nanotube active-matrix backplanes for conformal electronics and sensors. *Nano Lett.*, 11:5408–5413, 2011. 87

H. Tamai, K. Maruo, H. Ueno, K. Terao, H. Kotera, and T. Suzuki. Development of low-fluorescence thick photoresist for high-aspect-ratio microstructure in bio-application. *Biomicrofluidics*, 9:022405, 2015. 58, 110

R.C. Tenent, T.M. Barnes, J.D. Bergeson, A.J. Ferguson, B. To, L.M. Gedvilas, M.J. Heben, and J.L. Blackburn. Ultrasmooth, large-area, high-uniformity, conductive transparent single-walled-carbon-nanotube films for photovoltaics produced by ultrasonic spraying. *Adv. Mater.*, 21:3210–3216, 2009. 27, 79, 86, 87, 91, 92

S. Teymouri, F. Loghin, M. Bobinger, Z. Guttenberg, and P. Lugli. Transparent carbon nanotube electrodes for electric cell–substrate impedance sensing. *MRS Communications*, 9:1292–1299, 2019. 53, 69, 70, 76, 80, 81, 86, 87, 88, 93, 95, 97, 99, 101, 103, 107

ThermoFisher. Cell morphology. https://www.thermofisher.com/de/de/home/references/gibco-cell-culture-basics/cell-morphology.html, 2019. [Online; accessed 30-August-2019]. 34

A. Thess, R. Lee, P. Nikolaev, H. Dai, P. Petit, J. Robert, C. Xu, and et al. Crystalline ropes of metallic carbon nanotubes. *Science*, 273:483–487, 1996. 23

M. Tinkham. Energy gap interpretation of experiments on infrared transmission through superconducting films. *Phys. Rev.*, 104:845, 1956. 79

M.A. Topinka, M.W. Rowell, D. Goldhaber-Gordon, M.D. McGehee, D.S. Hecht, and G. Gruner. Charge transport in interpenetrating networks of semiconducting and metallic carbon nanotubes. *Nano Lett.*, 9:1866—1871, 2009. 13

M. Vafaiee, R. Mohammadpour, M. Vossoughi, E. Asadian, M. Janahmadi, and P. Sasanpour. Carbon nanotube modified microelectrode array for neural interface. *Frontiers in Bioengineering and Biotechnology*, 8, 2021. 17

L. Vaisman, H.D. Wagner, and G. Marom. The role of surfactants in dispersion of carbon nanotubes. *Advances in Colloid and Interface Science*, 128:37–46, 2006. 8, 10, 23, 24, 25, 28, 90, 110

M.V. Vellayappan, S.K. Jaganathan, and I.I. Muhamad. Unravelling the potential of nitric acid as a surface modifier for improving the hemocompatibility of metallocene polyethylene for blood contacting devices. *PeerJ*, 4:e1388, 2016. 28

M.D. Vo and D.V. Papavassiliou. Effect of sodium dodecyl sulfate adsorption on the behavior of water inside single walled carbon nanotubes with dissipative particle dynamics simulation. *Molecules*, 21:500, 2016. 25

M.D. Vo, B. Shiau, J.H. Harwell, and D.V. Papavassiliou. Adsorption of anionic and non-ionic surfactants on carbon nanotubes in water with dissipative particle dynamics simulation. *Chemical Physics*, 144:204701, 2016. 25, 90, 91

M.O. Wang, J.M. Etheridge, J.A. Thompson, C.E. Vorwald, D. Dean, and J.P. Fisher. Evaluation of the in vitro cytotoxicity of cross-linked biomaterials. *American Chemical Society*, 14:1321–1329, 2013a. 74

X. Wang, Q. Jiang, W. Xu, W. Cai, Y. Inoue, and Y. Zhu. Effect of carbon nanotube length on thermal, electrical and mechanical properties of CNT/bismaleimide composites. *Carbon*, 53:145–152, 2013b. 8

Y. Wang and G.J. Weng. *Micromechanics and Nanomechanics of Composite Solids*. Springer International Publishing AG, 2018. 14

J. Wegener, C.R. Keese, and I. Giaever. Electric cell–substrate impedance sensing (ECIS) as a noninvasive means to monitor the kinetics of cell spreading to artificial surfaces. *Experimental Cell Research*, 259:158–166, 2000. 46, 101

G. Wypych. *Handbook of fillers (Fourth Edition)*. ChemTec Publishing, 2016. 11

G. Xiao, Y. Tao, J. Lu, and Z. Zhang. Highly conductive and transparent carbon nanotube composite thin films deposited on polyethylene terephthalate solution dipping. *Thin Solid Films*, 518:2822–2824, 2010. 11

P. Xue, J. Bao, Y.J. Chuah, N.V. Menon, Y. Zhang, and Kang Y. Protein covalently conjugated SU-8 surface for the enhancement of mesenchymal stem cell adhesion and proliferation. *Langmuir*, 30:3110–3117, 2014. 76

T. Yamada, Y. Hayamizu, Y. Yamamoto, Y. Yomogida, A. Izadi-Najafabadi,

D.N. Futaba, and K. Hata. A stretchable carbon nanotube strain sensor for human-motion detection. *Nat. Nanotechnol.*, 6:296, 2011. 14

K. Yanagi, H. Udoguchi, S. Sagitani, Y. Oshima, T. Takenobu, H. Kataura, T. Ishida, K. Matsuda, and Y. Maniwa. Transport mechanisms in metallic and semiconducting single-wall carbon nanotube networks. *ACS Nano*, 4:4027–4032, 2010. 13

F. Yang, X. Wang, D.Q. Zhang, J. Yang, D. Luo, Z.W. Xu, and et al. Chirality-specific growth of single-walled carbon nanotubes on solid alloy catalysts. *Nature*, 510:522–524, 2014. 13

L. Yu, C. Shearer, and J. Shapter. Recent development of carbon nanotube transparent conductive films. *Chem. Rev.*, 116:13413–13453, 2016. 9, 12, 13, 15, 18, 19, 20, 21, 22, 24, 78

K. Yurekli, C.A. Mitchell, and R. Krishnamoorti. Small-angle neutron scattering from surfactant-assisted aqueous dispersions of carbon nanotubes. *American Chemical Society*, 126:9902–9903, 2004. 26

S. Zanganeh, F. Khodadadei, S.R. Tafti, and M. Abdolahad. Folic acid functionalized vertically aligned carbon nanotube (FA-VACNT) electrodes for cancer sensing applications. *Journal of Materials Science and Technology*, 32:617–625, 2016. 15

S. Zhang, T. Shado, S.S. Bekaroglu, and T. Karanfil. The impacts of aggregation and surface chemistry of carbon nanotubes on the adsorption of synthetic organic compounds. *Environ. Sci. Technol.*, 43:5719–5725, 2009. 23, 90

X. Zhang, T.V. Sreekumar, T. Liu, and S. Kumar. Properties and structure of nitric acid oxidized single wall carbon nanotube films. *Phys. Chem. B*, 108: 16435–16440, 2004. 24

Y. Zhang, L. Wang, J. Zhu, Y. Hu, W. Xing, and J. Cheng. Real-time monitoring of extracellular matrix-mediated PC12 cell attachment and proliferation using an electronic biosensing device. *Biotechnol. Lett.*, 34:397–404, 2012. 45

N. Zhao and J. Kang. *Carbon Nanotubes - synthesis, characterization, applications*. InTech, 2011. 19

Y. Zhou and R. Azumi. Carbon nanotube based transparent conductive films: progress, challenges, and perspectives. *Science and Technology of Advanced Materials*, 17:493–516, 2016. 23, 27, 28, 79, 90

# List of Figures

# Nomenclature

**2D** 2-dimensional

**AC** Alternating current

**Ag** Silver

**AgNPs** Silver nanoparticles

**AgNWs** Silver nanowires

**APTES** (3-aminopropyl)triethoxysilan

**Au** Gold

**BSA** Bovine serum albumin

**c.m.c** Critical micelle concentration

**CMC** Carboxymethyl cellulose

**CNTs** Carbon nanotubes

**CTAB** Cetyltrimethylammonium bromide

**Cu** Copper

**CVD** Chemical vapor deposition

**DI** Deionized

**DWCNTs** Double-walled CNTs

**ECIS** Electric cell-substrate impedance sensing

**FDA** Fluorescein diacetate

**GPa** Giga pascal

**h** Hour

**IPA** Isopropyl alcohol

**MWCNTs** Multi-walled CNTs

**OLED** Organic light-emitting diodes

**P/S** Penicillin-streptomycin

**Pd** Palladium

**PI** Propidiumiodid

**Ra** Surface roughness

**Rs** Sheet resistance

**RT** Room temperature

**SDS** Sodium dodecyl sulfate

**SEM** Scanning electron microscope

**SMU** Source measuring unit

**SPES** Sulfonated poly(ether sulfone)

**SWCNTs** Single-walled CNTs

**TCFs** Transparent conducting films

**TFT** Thin film transistors

**TPa** Tera pascal

$treated - COP$ atmospheric-pressure plasma-treated cyclic olefin polymer

# Publications

Shokoufeh Teymouri, Florin Loghin, Marco Bobinger, Zeno Guttenberg, Paolo Lugli. Transparent carbon nanotube electrodes for electric cell–substrate impedance sensing. MRS Communications, 9:1292–1299, 2019.

Vijay Deep Bhatt, Shokoufeh Teymouri, Katharina Melzer, Alaa Abdellah, Zeno Guttenberg, Paolo Lugli. Biocompatibility tests on spray coated carbon nanotube and PEDOT:PSS thin films. IEEE Transactions on Nanotechnology, 15:373–379, 2017.

# Acknowledgement

I would like to acknowledge my supervisor Prof. Paolo Lugli for giving me the great opportunity to do a PhD in his research group and I appreciate his support and guidance during my PhD. I would like to thank my mentor at ibidi Dr. Zeno Guttenberg for the time and effort he put into my thesis. Great thanks goes to Dr. Roman Zantl for giving me such a great opportunity to join ibidi. I've learned many things from him, not only scientifically but also from his positive character.

I would like to thank Prof. George Malliaras, and all the partners who have organized excellent training schools and meetings in the OrgBio project. Many thanks to Prof. Diamond, Dr. Larisa Florea and Dr. Alexandru Tudor at Dublin City University for giving me this opportunity to join their Lab for my secondment, which was a great academic experience. Special thanks to Dr. Róisín Owens for a well-organized and a great informative secondment at the Microelectronics Center of Provence in France.

I would like to thank PD. Markus Becherer at the Institute of Nanoelectronic for his significant support at the university. I wish to show my gratitude to Mrs. Antonia Raschke in graduate center of Electrical and Computer Engineering Department for being always supportive and helpful. Special thanks to Florin Loghin for introducing the spray-coating technique and his guidance during my

PhD project. I would also like to thank Dr. Marco Bobinger for always being helpful in the lab and introducing the scanning electron microscopy. It was a great pleasure working with this team in a productive atmosphere.

I highly appreciate my colleagues at ibidi in all departments for their support and time, and of course the pleasant atmosphere. Many thanks to Iris, Simon and Valentin for their support in administration process and my accommodation in Germany. Thanks to Jan for his understanding and giving me time to finish this work. Special thanks to Peter, Christopher, Lea and Ulf for their comments during the writing process of my paper. Thanks to Helga, Elias, and Peggy for the informative workshops that I had at ibidi. Thanks to Christian Ammer for providing the required ibidi products for my experiments. Many thanks to Wolfgang for providing the required array holder. Thanks to Johanness for his support in IT.

I would also like to thank my parents for their encouragement, positive energy and support. I owe my success to them for their patience and dedication. Many thanks to little baby in my tummy for participating in finalization of thesis and helping mom to finish the work. Special thanks to Amir for all his support, patience, encouragement, and love. Words and sentences cannot express my gratitude to him.